ABSTRACT

VO, LONG HOANG. Determination of P-y Curves for Sand by Laboratory Experiments and Three-dimensional Numerical Analyses of Laterally Loaded Piles. (Under the direction of Dr. Mohammed Gabr and Dr. Mervyn Kowalsky)

P-y curves for sandy soil are determined in this study based on laboratory tests and regression analysis of laterally loaded pile tests by 3D numerical simulation. Soil parameters resulted from sixteen triaxial tests is used to generate API p-y curves, and a procedure of converting stress-strain curves into API-similar p-y curves is suggested.

Numerical analysis of large-scale pile experiments indicates insignificant effects of cyclic loading on p-y curves at low numbers of cycles; however, boundary condition and surcharge are very influential to soil-pile behavior and properties of p-y curves. Numerical simulation is extended to free-field condition and parametric study on effect of soil relative density is performed. Correlation between calibrated model parameters and those from triaxial tests is also developed as recommendation for future 3D finite element models.

P-y relationships resulted from numerical analysis suggests overestimation of modulus of subgrade reaction and underestimation of soil ultimate resistance in API recommendations. Supplementary vertical stress caused by pile displacement is believed to change soil failure surface and improve soil ultimate resistance.

Determination of P-y Curves for Sand by Laboratory Experiments and Three-dimensional Numerical Analyses of Laterally Loaded Piles

by
Long Hoang Vo

A thesis submitted to the Graduate Faculty of
North Carolina State University
in partial fulfillment of the
requirements for the Degree of
Master of Science

Civil Engineering

Raleigh, North Carolina
2016

APPROVED BY:

Dr. Roy Borden

Dr. Mohammed Gabr
Committee Co-Chair

Dr. Mervyn Kowalsky
Committee Co-Chair

DEDICATION

I dedicate this achievement to my dearest maternal grandparents and paternal grandmother, who brought me up and taught me to become a decent man with a kind heart, optimism and determination to pursue dreams. I would like to thank my loving family for encouragement and support in whole the journey. Thank you to my wife, Trinh Phan, whose sacrifices, hard-work, love and encouragement over the years made this achievement possible. Lastly, this is for my son, Khoi Vo, my true believer, who is the reason and driving force for this journey.

ACKNOWLEDGMENTS

The research work presented in this thesis has been performed under supervision of Professor Mohammed Gabr, who has been providing extensive knowledge, and helpful support and guidance throughout the research and preparation of this thesis. I would like express my gratitude to him for his mentorship, support and direction. I also would like to extend my appreciation to Professor Mervyn Kowalsky for the opportunity to work in this wonderful project so I can accomplish the research interest that I have been really into since undergraduate study, and for the courses that become a significant input for my knowledge and this research.

I would like to show my deep gratefulness to Professor Roy Borden, who has been my academic advisor whole Masters' program, for being a member of my committee and for precious advices and assistances in last two years.

A huge thank is to Diego Aguirre, Chien-Ting Tang and Jinung Do for their help on experimental works, especially Diego's generosity in sharing processed pile experimental data. Many thanks go to other Professors and friends in Geotechnical group for their helps at times and friendship over this remarkable stage of life.

My special thank goes out to Vietnam Education Foundation for financial and other supports that turn my studying dream to reality.

Finally, and most importantly, my deepest appreciation goes to my beloved wife and son for boundless support and patience in this journey with me.

BIOGRAPHY

Long Vo was born and raised in Vinh City, Vietnam, and moved to Hanoi and Ho Chi Minh City for undergraduate study and developing career, respectively. He completed Bachelor degree in Civil Engineering in 2002 at National University of Civil Engineering in Vietnam, and had been working as both structural engineer and teaching assistant in geotechnical engineering ever since. He continued his study into graduate school at North Carolina State University on a fellowship awarded by Vietnam Education Foundation to pursue Master of Science degree in Civil Engineering with an emphasis in Geotechnical Engineering. He plans to advance to PhD program soon.

TABLE OF CONTENTS

LIST OF TABLES

LIST OF FIGURES

1. INTRODUCTION

1.1 Background

Analysis of laterally loaded pile has been a prominent case of the emerging field of soil-pile/structure-interaction. This is a typical problem that needs to be dealt with in design of offshore platforms, bridges and earth retaining structures. Different from axially loaded single pile, which can be treated as axisymmetric problem, or long wall subjected to earth lateral pressure, which is categorized as plain strain, horizontally loaded pile problem, single or in group of limited number, is a real three-dimensional problem due to direction of loading and complexity of stress and strain states in surrounding soil. In addition, with this problem, one has to deal with soil properties in horizontal direction, which is affected by soil anisotropy. However, despite of high level of complexity of the problem, the solutions or the approaches towards the solutions could and should be practical.

P-y curves approach has been developed for sand and clay and layered ground since 1950's in semi-empirical way. P-y curve describes relationship between soil reaction to pile lateral deflection at given depth. The soil reaction is in form of load per unit length could be understood as equivalent resultant of pressure by surrounding soil on pile. It captures soil nonlinear response and influence of nature of loading. The theoretical solution was developed analytically and subsequently calibrated and refined by small to large scale experiments on instrumented piles. P-y curve are developed in relation with pile configurations and soil properties obtained from laboratory experiments or in-situ investigation. Improved solutions have been developed and validated for cyclic and dynamic loading through the years (El Naggar and Novak, 1995, Boulanger, *et al.*, 1999, Pranjoto and Pender, 2003, Gerolymos and Gazetas, 2005, Allotey and El Naggar, 2008). Pile analysis using p-y model could be performed analytically and numerically. In numerical analysis, p-y relationships are characterized in discrete springs in conjunction with other elements namely frame for pile, gap member describing soil-pile attachment, detachment and re-attachment in cyclic and dynamic loading, and dashpot describing soil damping in dynamic case. Beam on nonlinear Winkler foundation (BNWF) approach using p-y relationship has been considered as the standard-of-practice for the analysis and design of laterally loaded piles.

With the development of finite element method and numerical analyzing packages, 2D and 3D simulation, in which soil is described by constitutive models offers another way to investigate soil-pile interaction and verify p-y curves. Since it is a more advanced approach, the input parameters for analysis are required better in quantity and quality to yield reliable outcomes. Soil reaction is not given directly from analyzed outcomes but is obtained from processing results on stresses at points in soil clusters adjacent to pile surface.

As a soil-structure interaction problem, to derive correct solution the analyzing procedure needs to implement appropriate responses of pile and surrounding soil to acting load. Pile flexural behavior is the main concerns from the structural part. The pile can be rigid, elastic or nonlinear, and choosing appropriate sectional flexural rigidity to range of loading is important for the investigation. Reinforced-concrete-filled-steel-pipe pile (RCFSPP) is a subject of this study. Working as a composite section, steel jacket and concrete core interaction is mutually beneficial, thus its axial, flexural and shear capacity is enhanced. Circumferential steel tube provides larger flexural rigidity and is able to resist larger tensile and compressive stress. Steel pipe also increases inner concrete compressive strength through passive confinement caused by concrete dilation, which in turn hinders pipe inward buckling (Furlong, 1967, Lu and Kennedy, 1994, Priestley, *et al.*, 1994, Elremaily and Azizinamini, 2002).

RCFSPPs are suitable for regions at high risk of earthquake. Since ductility capacity of the section is significantly improved in comparison to conventional concrete one, the system has ability to sustain large lateral displacement when the structure enters inelastic region (Priestley and Park, 1969, Chail, *et al.*, 1991, Priestley, *et al.*, 1994). For bridges, they normally perform as column-pile system with a column-cap. Column part is above and pile part is below ground level. Under action of seismic load there are typically two plastic hinges, each forms in one part of the system. The first one likely develops at column top, at the column-cap intersection, where the maximum moment occurs as the system works with restrained-head condition (Song, *et al.*, 2005, Song and Chai, 2008). Once column hinges, moment diagram varies and majority of additional moment caused by larger load is distributed to locations in elastic regions, which could lead to formation of second hinge. Is it reported that underground hinge plays a minor role in design of restrained-head pile-column system since it likely remains elastic while top hinges reaches damage control limit state (Montejo, *et al.*, 2012). However, for free-head condition, in ground hinge would govern pile-column performance and thus its formation should be well investigated.

A large-scale testing program on RCFSPPs is performed in the soil pit at the Constructed Lab Facilities of North Carolina State University. The objective of the work is to investigate the development of underground plastic hinge as the soil stiffness is varied and the corresponding performance of pile in framework of performance-based design. The plastic hinge formation is influenced by presence of surrounding soil, boundary condition and surcharge. Reaction from subsurface layers alters moment diagram along pile and therefore influences location of hinge and corresponding value of yielding lateral force at column top. Soil characterization thus is required as the input for analysis of pile testing data and for generating p-y curves for 2D analysis using Beam on nonlinear Winkler foundation approach or constitutive model in 3D finite element study. Although soil tests can only be conducted in limited conditions that do not fully reflects real behavior of soil elements under the impact of pile, soil properties are important for future analysis as correlation between them with calibrated model parameters, which are back analyzed from observed data, could be derived. A set of soil properties that one associates to another also helps the verification process.

This study aims to develop p-y curves for laterally loaded piles from soil laboratory triaxial testing data, from three-dimensional numerical analysis of large-scale pile testing in bounded condition and from three-dimensional numerical analysis of the same pile in unbounded condition of reality.

1.2 Scope of work

This study started with literature review of triaxial testing, factors that should be considered during testing, post-testing corrections of data, and how to use test results to generate p-y curves and build a set of model parameters for numerical analysis. Another portion of literature review was on numerical analysis of laterally loaded pile.

Sixteen triaxial tests in axial compression stress path were performed along with other soil classification tests. Reconstituted specimens for the tests were prepared in four different void ratios and were tested at four confining pressure. Test results were employed to construct p-y curves following American Petroleum Institute (API) recommendations (API, 2000). A procedure to convert axial compression stress-strain responses to API-similar p-y relationship is proposed.

Based on two pile experimental results, three-dimensional numerical analyses by Plaxis 3D Finite Element (Brinkgreve and Broere, 2006) program were performed to calibrate model parameters. P-y curves are derived from the finite element analyses under three condition: (1) p-y curves for cyclic loading in bounded conditions, which is pile testing conditions, (2) p-y curves for static loading in bounded conditions, and (3) p-y curves for static loading in free-field conditions.

1.3 Layout

This research is organized in form of two papers. Paper I is focused on laboratory testing on sand and p-y curves generated from results of soil experiments. Review of testing procedure, corrections, hyperbolic model and p-y curves is presented in Sections from 2.2 to 2.4. Soil classification and triaxial testing results are shown in Sections 2.6 and 2.7, respectively. Section 2.8 illustrates derived p-y curves. Conclusions and recommendations for this part will be place in Section 2.9

The second paper starts with background on numerical analysis of laterally loaded pile (Section 3.2). Pile testing program and results are described in Section 3.3. Sections 3.4 and 3.5 present 3D simulation and derived p-y curves from model calibration of testing results. Comparison of calibrated soil properties and triaxial test results is in Section 3.6, followed by parametric study on effects of boundary conditions and soil density are shown in Section 3.7. Conclusions and recommendations are expressed in Section 3.8.

Section 4 consists of summary of conclusions of Paper I and Paper II and recommendations for future researches.

2. PAPER I: EXPERIMENTAL SOIL PARAMETERS FOR DEVELOPING P-Y CURVES

2.1 Introduction

P-y curve model has been a practical and effective method in investigating performance of laterally loaded pile. P-y relationship recommended by American Petroleum Institute has been used widely in analytical and numerical analyses. Two characteristic parameters of p-y relationship are modulus of subgrade reaction, which is selected based on shear strength parameters, and ultimate resistance, which can be computed from soil friction angle or undrained shear strength, pile diameter and loading properties (API, 2000). Therefore, soil laboratory experiments or/and in-situ investigation data are necessary for generating p-y curves. Three-dimension numerical simulation is a powerful tool to analyze complicated soil-structure interaction problems. With a proper soil constitutive model and model parameters, the simulation can perform deformation analysis at high level of accuracy. Constitutive model and model parameters are most important input for the analysis. Model and its set of parameters are normally calibrated by regression analyzing data of completed experiments on structural systems. Comparison and/or correlation between those calibrated parameters and properties determined from lab tests or in-situ ground investigation is very valuable for future analysis on comparable problems. P-y curves also can be determined from 3D finite element analysis of laterally loaded pile.

As a part of an investigation on performance of laterally loaded pile in sand, this study is focused on laboratory characterizing soil properties to construct API-based p-y curves for tested soil. This set of properties also a basis for selecting model parameters for 3D numerical analysis in a separate paper to determine another set of p-y curves. Axial compression (AC) stress path is selected to deliver soil strength parameters and stress-strain responses as input for above tasks. The main reasons are that triaxial test is an advanced method in characterizing soil shear strength and stress-strain response, and it has been studied for long time in relation to soil constitutive behavior of soil. Its popularity and practicality also are factors for the selection. Triaxial tests are performed with wide range of soil density to develop relation between relative density and soil engineering parameters (unit weight, modulus and friction angle).

In order to obtain reliable data from triaxial tests, testing procedure and factors affecting experimental results are carefully reviewed. Post-testing corrections for membrane effects and change in cross-sectional are assessed and applied to develop stress-strain response. Obtained soil properties will be checked with previous studies. Bases on obtained soil properties, p-y curves are generated following American Petroleum Institute (API) recommendations (API, 2000). A preliminary procedure of converting axial compression stress-strain response to API-similar p-y curve is also recommended.

2.2 Background on triaxial testing

2.2.1 Triaxial test

Triaxial test with conventional apparatus is widely used to measure shear strength parameters and stress-strain response of soils. It has many advantages: drainage control, less stress concentration, failure plane is not pre-defined, and various stress paths could be performed. Triaxial test comprises two main stages: (1) consolidation to replicate in-situ stress state or loading history of soil element and (2) shear to simulated how the soil element to be loaded due to structure. By controlling drainage conditions, radial (σ_h) and axial (σ_v) stresses during consolidation and shear, as presented in Table 2.1, several stress types and shearing modes could be performed. Laboratory testing stress path on soil should be compatible with field stability and deformation situation. Among stress paths, AC is the least complicated one to perform with presently available equipment and is the most likely to appear in geotechnical investigation report for shear strength of sandy soils along with other in-situ methods. Current standards cover this testing method are ASTM D7181− 11 and D4767− 11 for CD and CU conditions, respectively.

True triaxial testing apparatus have been introduced (Ko and Scott, 1967, Airey and Wood, 1988, Ibsen and Praastrup, 2002, Ismail, *et al.*, 2005, Changho Choi, *et al.*, 2008) that allows testing soils at any stress state and more complex stress paths considering effects of intermediate principal stress and anisotropy.

Table 2.1. Triaxial test conditions

Drainage control	Consolidation	Shearing modes
Unconsolidated - Undrained (UU), Consolidated - Undrained (CU), Consolidated - Drained (CD),	Isotropic consolidation: $\sigma_h = \sigma_v$, K_o-consolidation: $\sigma_h = K_o\sigma_v$,	Axial Compression (AC): $\Delta\sigma_h = 0$, $\Delta\sigma_v > 0$, Axial Extension (AE): $\Delta\sigma_h = 0$, $\Delta\sigma_v < 0$, Lateral Compression (LC): $\Delta\sigma_h > 0$, $\Delta\sigma_v = 0$, Lateral Extension (LE): $\Delta\sigma_h < 0$, $\Delta\sigma_v = 0$,

2.2.2 Specimen preparation method

Cohesionless soils are normally tested in reconstituted specimens. Wood, *et al.* (2008) summarized depositional methods for sample preparation:

- Dry funnel deposition is a commonly used method. Soil is filled in from bottom of mold with low falling head (about 6mm). Sample density could be increased raising funnel up quickly or tapping symmetrically on mold side,

- Water sedimentation aims to provide sample with loosest possible density and higher saturation. The procedure is suggested by Chaney and Mulilis (1978) to produce soil structure that is resulted from natural sedimentation. Since the soil is boiled before being filled into the mold, the sample has higher degree of saturation. Thomson and Wong (2008) found out that uniformity of specimen by this method is not as good as assumed.

- Slurry and mixed dry deposition are methods to make homogenous sample by mixing soil in de-aired water and in dry state, respectively. These two methods are used for silty sand specimens to avoid grain segregation,

- Air pluviation is to rain sand through dispersing screen into the mold. Falling height and raining rate are two main factors effecting on soil density. Higher drop height induces higher soil density and, in contrary, faster raining rate produces lower density. Constant height and rate would yield samples with uniform density,

- Dry and moist tamping methods produce specimen by tamping soil into mold in layers. It minimizes soil segregation and prepare samples with wide range of relative density (Ladd, 1978). Moist tamping might yield very loose sample; however, it was concluded that sampling by this method is less homogeneous than by air pluviation (Jang and Frost, 1998). Frost and Park (2003) confirmed the finding based on X-ray images that displayed sudden change in density at layer boundaries. Thomson and Wong (2008) reported the same pattern and significant difference in void ratio within each layers based on X-ray computed tomography (CT) scanning images.

2.2.3 Effects of specimen aspect ratio and end restraint

ASTM-D7181 recommends using cylindrical specimen with diameter of 33 mm or higher and aspect ratio from 2 to 2.5. The diameter also should be at least six times as large as largest grain size. Figure 2.1 describes Bishop and Green (1965) study on influence of end restraint in triaxial test on sandy soil strength. Material was fine to medium ham River sand and specimens had aspect ratios of 0.5, 1 and 2 with regular and lubricated ends. For the samples with height-to-diameter ratio of 2 to 1, end restraint had no effect on soil shear strength but the impact was increasingly significant for lower ratios. Authors also reported 2 to 1 samples had bulging shape during shear with little enlargement of diameter at the ends. On the other hand, very efficient platens lubrication could reduce aspect ratio to 1 to 1 having same friction angle as of 2 to 1 sample. 1 to 1 sample had large expansion at sample ends and maintained cylindrical shape up to peak strain.

Duncan and Dunlop (1968) realized effective friction of lubricated ends were reversely proportional to sample diameter. Therefore, lubricated caps and bases could be either effective or ineffective in different cases. For drained tests, they suggested stress difference at given axial strain in normal ends sample to be higher than that in sample with lubricated ends. However, samples with low end restraint would dilate more at given stress level and have more uniform radial dilation over sample height, making it more possible to further the test to large strain with more reliable stress-strain response,

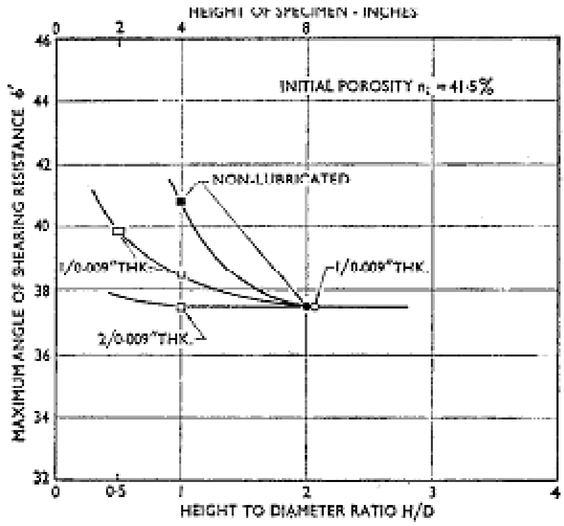

Figure 2.1. Influence of specimen aspect ratio on soil friction angle at various degree of end restraint (Bishop and Green, 1965)

2.2.4 Saturation and back pressure

In triaxial testing procedure, using Skempton's B parameter to determine specimen level of saturation was suggested by Chaney, *et al.* (1979). It is evident that sample degree of saturation has significant effect on soil shear strength. Mulilis, *et al.* (1978) performed triaxial tests on Monterey No. 0 sand at B-values of 0.91, 0.92, 0.93 and 0.97 or higher, which are all corresponding to degree of saturation of almost 100% (Black and Lee, 1973, Mulilis, *et al.*, 1978), and found out that samples at lower B-values had shear strength higher by some 10% than those at 0.97 or higher. ASTM-D7181 (2011) recommends B- value of specimen to be equal to or greater than 0.95.

To assure sample saturation requirement, following steps are typically conducted in sample preparation and saturation:

- Saturates porous stones by boiling in de-aired water for about 15 minutes and keep them always submerged in de-aired water before placing into apparatus,
- Flushes out any air bubbles trapped in pumps, sensors and pipes,
- Circulation of carbon dioxide (CO_2) through samples to replace the air in the sample since CO_2 has higher water solubility than air. This practice aims to reduce time and pressure value for back pressure process. However, it was suggested that side reaction between soil components and CO_3H could take place as a limitation (Rad and Clough, 1984)
- Back pressure the specimen to dissolve air bubbles into water. During this stage, both cell and pore pressure are incrementally applied to maintain constant effective pressure on sample and, therefore, avoid volume change. ASTM-D7181 recommendes efective stress during back pressure should not excess 35 kPa.

Without supplemental use of CO_2, back pressure requires high pressure and/or considerable time. Initial degree of saturation plays a decisive role in these two aspects (Lowe and Johnson, 1960, Black and Lee, 1973). Under same applied back pressure, wet samples need longer time to be saturated; however, required back pressure for wet sample a much lower than for fairly dry sample. Lowering back pressure facilitates triaxial test as it helps overcome issues of leakage and chamber wall limit pressure. Since the sample is flushed with water during the seating stage of triaxial test, it would be beneficial to increase initial level of saturation. Rad and Clough (1984) proposed using vacuum for this stage, which allows water percolation under controlled pressure in a very short period of time, normally 5 minutes, to decrease final required back pressure values for saturating sample. Although this method is quite complicated to perform it proves that water circulation can significantly improve saturation process.

Black and Lee (1973) also suggested that soil stiffness strongly influences pore water pressure response. Medium to soft soil might have B-value of from 0.93 to 0.99 at degree of saturation of 99% while stiff and very stiff soil has B < 0.5 at the same level of saturation. At required B=0.95, degree of saturation of soft soil is about 96%, and for stiff soil is 99.9%. This indicates that saturation of stiff sample is more difficult and soft samples should be saturated to B value higher than 0.95 required by current testing standard.

2.2.5 Strain rate during shear

Since shearing stage is strain-controlled, chosen rate of strain should guarantee full water pore pressure dissipation during drained shearing. ASTM-D7181 provides a guideline on this as follows:

$$\varepsilon = 4\% / (10t_{90}) \qquad (2.1)$$

where t_{90} is amount of time to reach degree of consolidation of 90% in confined compression test.

Yamamuro and Lade (1993) conducted study on uniform Cambria sand found out rate of strain has very insignificant effect on results of drained test. Triaxial tests were performed at strain rates of 0.0517%, 0.245% and 0.740% per minute and yielded relatively insignificant difference in deviatoric stress-strain curves although higher rate tended to give higher stress difference. Therefore, it can be concluded that in that range soil shear strength parameter, modulus and strain at peak are independent of strain rate. In a newer study Yamamuro, *et al.* (2011) performed very wide range to extremely high rate of strain tests on crushed loose and medium coral sand. For CD tests, tests at rates of from 0.0022% up to 0.0282% per second showed little variation.

2.3 Data corrections

2.3.1 Correction for volume change in saturation

During seating and saturation by back pressure stages, effective stress is maintained on sample, resulting in a volume change; however, due to unsaturation of sample, the real change is not equal to the variation in pore volume recorded. ASTM-D7181 suggests calculating change in volume of specimen during saturation as follows:

$$\Delta V_{sat} = 3V_o(\Delta H_s / H_o) \qquad (2.2)$$

where:

- V_o and H_o are initial volume and height of specimen, respectively,
- ΔH_s is specimen recorded change in height,

Garga and Zhang (1997) equipped both external linear varying displacement transducer (LVDT) and Hall effect radial displacement transducer (HRDT) in triaxial tests on Uminin sand to measure specimen volume change. Specimen initial relative density varies from 1.9% to 54.7%. Authors found that during saturation process, total decrease in void ratio due to seating pressure of 25kPa, water flushing and back pressure saturation ranges from 0.026 to 0.008; the lower relative density, the higher change in void ratio. Among them, the one at D_R=17% has void ratio change of 0.016, and the ones at D_R=28.1% and higher have similar figures of 0.008 and 0.009.

2.3.2 Correction for cross-sectional area

Specimen cross section changes its size during isotropic consolidation and shear. In latter stage, axial stress is determined by dividing recorded axial force by cross-sectional area. Due to significant deformation, which indicates in axial strain and volume change, sample might bulge significantly or exhibits a failure plane, resulting in considerable change in cross-sectional area. This will contribute to errors in computing deviatoric stress and should be corrected to obtain reliable stress-strain response, friction of angle and modulus.

The methods of computing effective cross-sectional area of specimen are based on the shape of sample during shear and whether it has failure plane or not (see Figure 2.2)

- Cylinder model (Germaine and Ladd, 1988):

This model assumes sample deforms as a right cylinder during shear. This method is more suitable for tests with ideally frictionless ends or lubricated platens that minimize end restraint. This model is adopted in ASTM-D7181 for CD test. Corrected cross-sectional area is given by:

$$A_\varepsilon = A_c[(1-\varepsilon_v)/(1-\varepsilon_a)] \tag{2.3}$$

where A_c is area after consolidation, and ε_v and ε_a are volumetric and axial strain, respectively, corresponding to A_ε

- Parabolic model (Germaine and Ladd, 1988):

This model assumes sample deforms as a barrel and the area is calculated at the largest mid-height section. Germaine and Ladd (1988) claimed that this model is developed particularly for undrained test. Corrected cross-sectional area is given by:

$$A_\varepsilon = A_c\left[-\frac{1}{4}+\frac{\sqrt{25-20\varepsilon_a-5\varepsilon_a^2}}{4(1-\varepsilon_a)}\right] \tag{2.4}$$

- Bulging model (Germaine and Ladd, 1988):

This model assumes the strains to be mostly contributed by central zone of the sample. Corrected cross-sectional area is given by:

$$A_\varepsilon = A_c[(1-\varepsilon_v)/(1-\alpha\varepsilon_a)] \tag{2.5}$$

Where: $\alpha = 1$ to 2 is an empirical constant could be computed as ratio of sample length to length of bulging zone. When $\alpha = 1$, equations 2.3 and 2.4 are identical, and equations 2.4 and 2.5 provide same result with $\alpha = 4/3$.

- Shear plane model (La Rochelle, *et al.*, 1988):

This model is more appropriate for stiff clay or dense sand samples. When shear plane is initiated, cross-sectional area decreases as two parts of specimen start sliding along the plane if no bulging occurs. However, for soil, since bulging always takes place around the edge of shear plane, the area increase, in general. This corrected cross-sectional area is applied for post-peak stress calculation and given by:

$$A_\varepsilon = A_f + (A_e - A_f)[(\varepsilon_a-\varepsilon_f)/(\varepsilon_e-\varepsilon_f)] \tag{2.6}$$

where:

- A_f: cross-sectional area at peak,

- A_e: cross-sectional area at the end of test,
- ε_f: axial strain at peak stress,
- ε_e: axial strain at the end of stress,

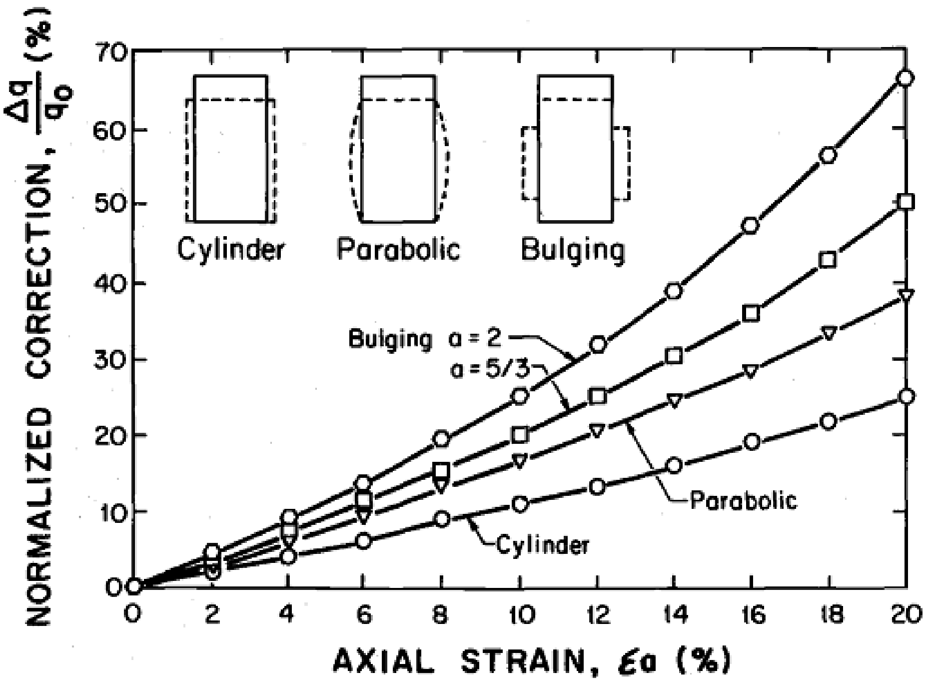

Figure 2.2. Correction for area of sample without failure plane and effect of models to magnitude of correction (Germaine and Ladd, 1988)

To select a proper model, change in shape of specimen should be closely monitored during and after testing (Zhu and Anderson, 1998). If bulging occurs during shear, parabolic and bulging models should be used in combined with α =4/3 for the latter. If there is shear plane after peak, equation 2.5 should be implemented to correct area prior to peak and 2.6 for remaining segment of stress-strain curve. Germaine and Ladd (1988) argued that calculation with cylindrical model would significantly overpredict strength of samples having actually parabolic deforming shape and substantially for ones with localized bulging. In other study, La Rochelle, *et al.* (1988)

categorized failure modes into bulging failure, which is cover both parabolic and bulging models mentioned above, and shear plane failure only. They considered equation 2.3 as satisfactory for samples that exhibits bulging deformation only.

It is noteworthy that positive value of ε_v or ε_a means corresponding component is in compression or decreasing.

2.3.3 Correction for membrane effects

Flexible membrane enclosing specimen has significant influence on soil behavior and derived shear strength parameters. Henkel and Gilbert (1952) reported that membrane effect contribute to apparent increase in undrained shear strength. Therefore, it is should be examined and must be addressed properly in order to obtain true response and strength of soil.

There have been two types of membrane effect correction: (i) corrections of principal stresses due to membrane resistance, and (ii) correction for membrane penetration. The latter describing penetration of latex membrane into void or gap between particles on specimen side surface during consolidation and then affect effective cross-sectional area and volumetric train in drained shear or evolution of pore pressure undrained shear stage.

It is noteworthy that correction for membrane resistance is associated to correction to cross-sectional area since it depends on assumption on deformation of specimen,

2.3.3.1 Correction for membrane resistance

During testing, especially in shearing phase, soil specimen and membrane experience strains in many directions at various level. Figure 2.3 illustrates stress and strain states in cylindrical membrane (Lade, 2016). Relationships between stress and strain for general and plane stress (σ_{rm}=0) conditions in realm of elasticity are presented in Table 2.2. General solutions for axial and circumferential stresses in membrane determined by elasticity theory with Poisson's ratio of 0.5 for membrane are presented in Table 2.3

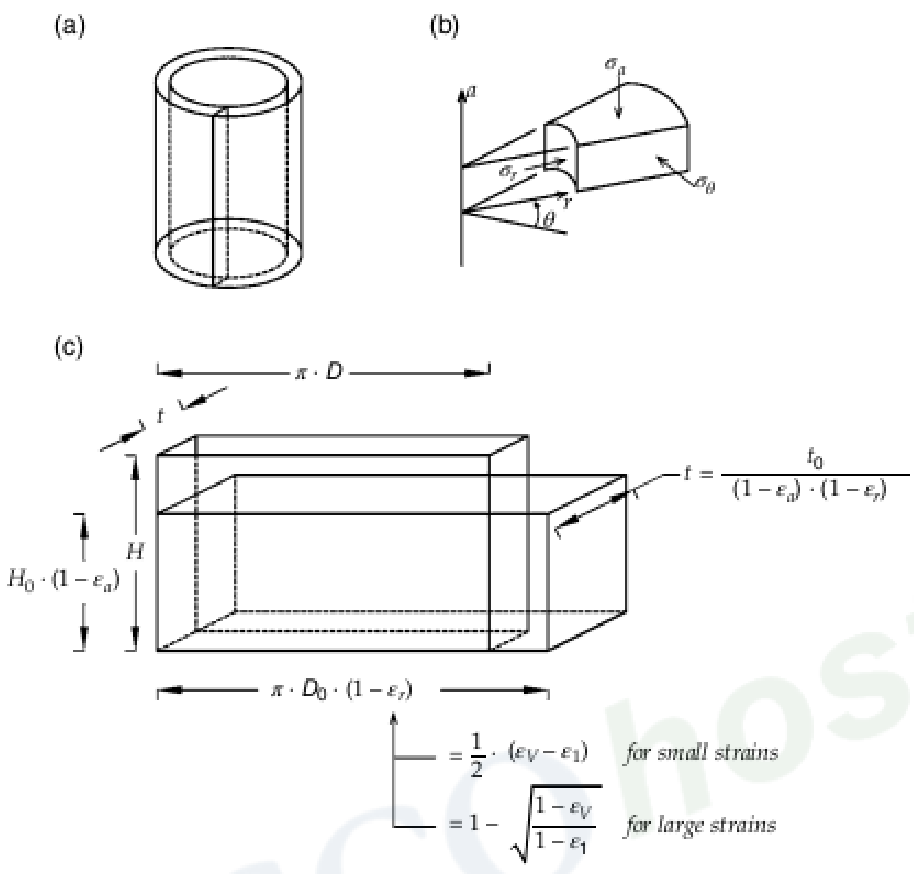

Figure 2.3. Stresses and strains in membrane: (a) cylindrical membrane, (b) stress in element, and (c) deformation of membrane (Lade, 2016)

Table 2.2. Relationship between membrane stresses and strains (Lade, 2016)

General condition		Plane stress condition	
$\varepsilon_{am} = \dfrac{1}{E_m}(\sigma_{am} - \nu\sigma_{\theta m} - \nu\sigma_{rm})$	(2.7)	$\varepsilon_{am} = \dfrac{1}{E_m}(\sigma_{am} - \nu\sigma_{\theta m})$	(2.10)
$\varepsilon_{\theta m} = \dfrac{1}{E_m}(-\nu\sigma_{am} + \sigma_{\theta m} - \nu\sigma_{rm})$	(2.8)	$\varepsilon_{\theta m} = \dfrac{1}{E_m}(-\nu\sigma_{am} + \sigma_{\theta m})$	(2.11)
$\varepsilon_{rm} = \dfrac{1}{E_m}(-\nu\sigma_{am} - \nu\sigma_{\theta m} - \sigma_{rm})$	(2.9)	$\varepsilon_{rm} = \dfrac{1}{E_m}(-\nu\sigma_{am} - \nu\sigma_{\theta m})$	(2.12)

Table 2.3. Stresses in membrane (Lade, 2016)

General condition		Plane stress condition	
$\sigma_{am} = \dfrac{2}{3}E_m(2\varepsilon_{am} + \varepsilon_{\theta m}) + \sigma_{rm}$	(2.13)	$\sigma_{am} = \dfrac{2}{3}E_m(2\varepsilon_{am} + \varepsilon_{\theta m})$	(2.15)
$\sigma_{\theta m} = \dfrac{2}{3}E_m(\varepsilon_{am} + 2\varepsilon_{\theta m}) + \sigma_{rm}$	(2.14)	$\sigma_{\theta m} = \dfrac{2}{3}E_m(\varepsilon_{am} + 2\varepsilon_{\theta m})$	(2.16)

Equations from 2.13 to 2.16 indicate that if ε_{am} and $\varepsilon_{\theta m}$ can be determined from specimen axial, radial and volumetric strains, which are ε_a, ε_r and ε_v, respectively, membrane resistance could be computed. In compression test, membrane and specimen are assumed to deform together (Lade, 2016), resulting in:

$$\varepsilon_{am} = \varepsilon_a \tag{2.17}$$

$$\varepsilon_{\theta m} = \varepsilon_r \tag{2.18}$$

- Axial stress correction (Lade, 2016):

$$\Delta\sigma_{1m} = \frac{P_{amembrane}}{A_{specimen}} = \frac{\sigma_{am} A_{m\varepsilon}}{A_{\varepsilon}} \tag{2.19}$$

in which:

- $A_{m\varepsilon} = A_{om} / (1-\varepsilon_a)$: membrane cross-sectional area,
- $A_{\varepsilon} = A_c[(1-\varepsilon_v) / (1-\varepsilon_a)]$: specimen cross-sectional area,
- A_{om}: cross-sectional area of membrane before shearing
- A_c: cross-sectional area of specimen before shearing

Equation 2.19 becomes:

$$\Delta\sigma_{1m} = \frac{A_{om}}{A_c(1-\varepsilon_v)}\sigma_{am} = \frac{4t_m}{D_c(1-\varepsilon_v)}\sigma_{am} \tag{2.20}$$

Substitution of 2.17, 2.18 and 2.13 into 2.20 produces:

$$\Delta\sigma_{1m} = \left[\frac{2}{3}E_m(2\varepsilon_a + \varepsilon_r) + \sigma_{rm}\right]\frac{4t_{om}}{D_c(1-\varepsilon_v)} \tag{2.21}$$

where:

- D_c: diameter of sample after consolidation,
- E_m: Young's modulus of membrane,
- t_{om}: initial membrane thickness,
- $\varepsilon_a, \varepsilon_r$: specimen axial and radial strain, respectively
- σ_{rm} : radial stress in membrane,

- Confining stress correction (Lade, 2016):

$$\Delta\sigma_{3m} = \frac{P_{\theta membrane}}{HD_{\varepsilon}} = \frac{2\sigma_{\theta m}Ht_m}{HD_{\varepsilon}} = \frac{2t_{m\varepsilon}}{D_{\varepsilon}}\sigma_{\theta m} \tag{2.22}$$

in which:

- $t_{m\varepsilon} = t_{om} / [(1-\varepsilon_a)(1-\varepsilon_r)]$: membrane thickness when it is strained,
- $D_\varepsilon = D_c(1-\varepsilon_r)$: specimen diameter when membrane is strained,

Then equation 2.22 becomes:

$$\Delta\sigma_{3m} = \frac{2t_{om}}{D_c(1-\varepsilon_a)(1-\varepsilon_r)^2}\sigma_{\theta m} = \frac{2t_{om}}{D_c(1-\varepsilon_v)}\sigma_{\theta m} \quad (2.23)$$

Substitution of 2.17, 2.18 and 2.14 into 2.23, produces:

$$\Delta\sigma_{3m} = \left[\frac{2}{3}E_m(\varepsilon_a + 2\varepsilon_r) + \sigma_{rm}\right]\frac{2t_{om}}{D_c(1-\varepsilon_v)} \quad (2.24)$$

Equations 2.21 and 2.24 are general solutions for stress corrections. Many researchers have implemented thus approach to derive corrections for principal stresses on specimen with following expressions for specimen radial strain at small and large strain (Lade, 2016):

- For small strain: $\varepsilon_r = 0.5(\varepsilon_v - \varepsilon_a)$ (2.25)
- For large strain: $\varepsilon_r = 1 - \sqrt{(1-\varepsilon_v)/(1-\varepsilon_a)}$ (2.26)

Henkel and Gilbert (1952) performed CU and unconfined compression tests on London clay and suggested strength contributed by flexible membrane is proportional to membrane stiffness and independent of specimen strength and confining pressure. Authors proposed two theories named compression shell theory and hoop tension theory to estimate magnitude axial and radial stress corrections, respectively. They claimed that corrections from above theories roughly met testing data on membrane only. La Rochelle, *et al.* (1988) confirmed the equations underestimated required magnitude of correction.

Duncan and Seed (1967) improved shell theory equation with consideration of both axial and volumetric strains of cylindrical deformation. They implemented plane stress condition, membrane Poission's ratio is 0.5, and use large strain formula for specimen radial strain (equation 2.26) to yield following expressions for stress corrections:

$$\Delta\sigma_{1m} = \frac{2E_m}{3}\left[1 + 2\varepsilon_{at} - \sqrt{\frac{1-\varepsilon_v}{1-\varepsilon_{at}}}\right]\frac{4t_{om}}{D_{os}(1-\varepsilon_v)} \quad (2.27)$$

$$\Delta\sigma_{3m} = \frac{2E_m}{3}\left[2 + \varepsilon_{at} - 2\sqrt{\frac{1-\varepsilon_v}{1-\varepsilon_{at}}}\right]\frac{2t_{om}}{D_{os}(1-\varepsilon_v)} \quad (2.28)$$

where:

- t_{om}: initial membrane thickness,
- D_{os}: initial diameter of specimen,
- ε_v: volumetric strain during shear,
- ε_{at}: total axial strain during consolidation and/or shear, percentage of specimen length prior to consolidation, as authors included effect of consolidation,

Some researchers (Molenkamp and Luger, 1981, Berre, 1982) have developed stress corrections for small strain conditions by adopting equation 2.25 for specimen radian strain. In addition, they assumed plane stress condition for membrane. Subsequently, the expressions for correction were derived as follows:

$$\Delta\sigma_{1m} = E_m\left[\varepsilon_a + \frac{1}{3}\varepsilon_v\right]\frac{4t_{om}}{D_c(1-\varepsilon_v)} \quad (2.29)$$

$$\Delta\sigma_{3m} = E_m\left[\frac{1}{3}\varepsilon_v\right]\frac{4t_{om}}{D_c(1-\varepsilon_v)} \tag{2.30}$$

For testing at low volumetric strain, equations 2.29 and 2.30 become:

$$\Delta\sigma_{1m} = E_m\left[\varepsilon_a + \frac{1}{3}\varepsilon_v\right]\frac{4t_{om}}{D_c} \tag{2.31}$$

$$\Delta\sigma_{3m} = \frac{4}{3}E_m\varepsilon_v\frac{t_{om}}{D_c} \tag{2.32}$$

Fukushima and Tatsuoka (1984) assumed that membrane axial deformation is independent of radial and circumferential deformations and suggested simplified equations on stress correction:

$$\Delta\sigma_{1m} = \frac{4E_m t_m \varepsilon_a}{D_c} \tag{2.33}$$

$$\Delta\sigma_{3m} = \frac{2E_m t_m \varepsilon_r}{D_c} \tag{2.34}$$

ASTM-D7181 and ASTM-D4767 adopted equation 2.33 for membrane correction. However, Lade (2016) commented 2.33 and 2.34 being unrealistic in view of elasticity theory as derived without Poission’s ratio,

La Rochelle, *et al.* (1988) investigated effect of initial confinement by membrane due to difference between nominated diameter of membrane and specimen diameter. Initial confining pressure induced by membrane stretching was given by:

$$\sigma_{om} = 2E_m t_{om}\frac{D_c - D_{om}}{D_c D_{om}} \tag{2.35}$$

where:

- D_c: diameter of sample after consolidation,
- D_{om}: initial diameter of membrane,
- E_m and t_{om}: Young's modulus and thickness of membrane, respectively

Germaine and Ladd (1988) combined solutions of Berre (1982) and La Rochelle, *et al.* (1988). In which axial correction was presented in term of force aiming to combine with area corrections in different deforming shapes,

$$\Delta F_{1m} = \pi E_m D_{om} t_{om} \left[\varepsilon_a + \frac{2}{3} \varepsilon_v \right] \tag{2.36}$$

$$\Delta \sigma_{3m} = 2 E_m t_{om} \left[\frac{2}{3} \frac{\varepsilon_v}{D_c} - \frac{D_c - D_{om}}{D_c D_{om}} \right] \tag{2.37}$$

where: E_m is Young's modulus of membrane ($\approx$ 1400 kPa)

The authors acknowledged that assumption of cylindrical deformation shape was implemented to derive corrections. However, they suggested that bulging likely would cause more significant error in radial than axial stress correction.

Axial and radial stress in AC test are corrected as follows (Lade, 2016):

$$\sigma_{1,corr} = \sigma_1 - \sigma_{1m} \tag{2.38}$$

$$\sigma_{3,corr} = \sigma_3 - \sigma_{3m} \tag{2.39}$$

Please be very mindful that positive value of ε_v, ε_a or ε_r means corresponding component is in compression or decreasing. Positive stress denotes compression.

2.3.3.2 Correction for membrane penetration and compliance

Membrane penetration and membrane compliance are terms used to describe membrane intrusion into peripheral voids between particles of specimen during consolidation and shear (see Figure 2.4). Evans and Seed (1987) used separately the former for consolidation and the latter indicate change in degree of penetration in shearing stage although others might have referred either of them in both phases.

Membrane penetration was first recognized and addressed by Newland and Allely (1957, 1959) when they performed drained and undrained tests on dilatant sand. Volume change and/or induced pore water pressure in triaxial tests are affected by this phenomenon, resulting in erroneous stress-strain response and soil shear strength. Evans and Seed (1987) suggested that membrane compliance leads to unconservative valuation on strength of contractive samples and overconservative valuation on dilative ones.

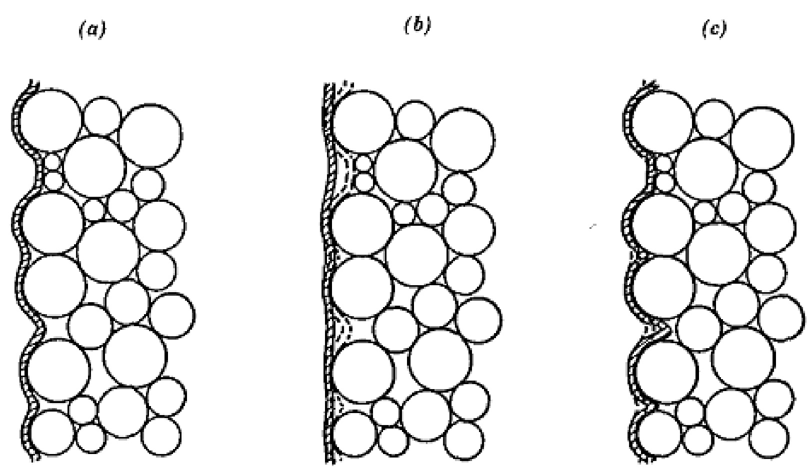

Figure 2.4. Deformation of membrane: (a) After consolidation; (b) during undrained shear with increasing pore water pressure; (c) during drained shear with increasing cell pressure (Kramer, *et al.*, 1990)

During consolidation, membrane penetrates into perimeter voids as water is being squeezed out. Therefore, specimen volume change is less than recorded change in volume. Bohac and Feda (1992) found that membrane penetration contributed about 50% of total volume change during K_0-consolidation.

In undrained shear, due to change in pore water pressure, specimen volume change might occur as further membrane penetration and rebound probably compensate soil skeleton dilation (Newland and Allely, 1959) and contraction, respectively. Since actual constant volume condition is not ensured, pore water development is compromised. Kiekbusch and Schuppener (1977) reported a 50 kPa difference in induced pore water pressure from undrained tests on medium sand samples with normal and liquid-rubber treated membranes. Meanwhile, in drained shear, the common sense is that effective confining pressure is constant, thus penetration compliance does not happen. However, since sample dilates (Newland and Allely, 1957) or its diameter increases during shear, hoops stress caused by membrane grows and increase effective confinement. Therefore, membrane enter further to the voids, resulting in incorrect volume strain derived from recorded volume change.

Membrane penetration is corrected by computing sample volumetric change by penetration effect. It has been done experimentally (Newland and Allely, 1957, 1959, Roscoe, *et al.*, 1964, Frydman, *et al.*, 1973, Kiekbusch and Schuppener, 1977, Martin, *et al.*, 1978, Ramana and Raju, 1982, Evans and Seed, 1987, Nicholson, *et al.*, 1993) and analytically (Molenkamp and Luger, 1981, Baldi and Nova, 1984, Kramer, *et al.*, 1990), and the former is likely preferable (Bohac and Feda, 1992). Nicholson, *et al.* (1993) cited numbers of earlier experimental studies, whose results were different from the analytical solutions, and suggested that further improvement of analytical models should be done to give better predictions. All above investigators agreed that dominant factors influencing membrane penetration are (i) soil grain size and gradation, and (ii) effective confining stress. Minor factors are: (i) particle angularity, (ii) soil fabric or sample preparation methods, (iii) soil density, (iii) membrane thickness and stiffness.

Once there is a change in effective confining pressure, the measured volume change can be described as totality of components induced by membrane penetration and true soil deformation as follows:

$\Delta V = \Delta V_s + \Delta V_m$, or:

$$\frac{\Delta V}{V_o} = \frac{\Delta V_s}{V_o} + \frac{\Delta V_m}{V_o} = \varepsilon_v + \Delta v_m \frac{A_m}{V_o} \qquad (2.40)$$

where:

- V_o: initial specimen volume,
- ΔV: total or recorded volume change,
- ΔV_m: volume change due to membrane penetration,
- ΔV_s: true volume change of specimen,
- ε_v: true volumetric strain,
- Δv_m: membrane penetration per unit area or unit membrane penetration,
- A_m: contact area between specimen and membrane,

Newland and Allely (1957) assumed that specimen deformation is isotropic, which leads to $\varepsilon_v = 3\varepsilon_a$, and described equation 2.40 in form of:

$\varepsilon_{vr} = \varepsilon_v + \varepsilon_m = 3\varepsilon_a + \varepsilon_m$, then:

$$\varepsilon_m = \varepsilon_{vr} - 3\varepsilon_a \qquad (2.41)$$

where: ε_m is the volumetric strain caused by membrane penetration,

Vaid and Negussey (1984) commented that equation 2.41 overestimates membrane penetration effect since sand exhibits anisotropic behavior that axial strain is lower than radian strain in experiments,

Frydman, *et al.* (1973) performed tests on mono-sized glass at three different diameters of 0.18mm, 0.3 mm and 1.85 mm. The confining latex membrane was 0.03mm. They varied confining pressure and specimen volume, but kept sample diameter and height) at the same time, by using solid and hollow specimen. As a result, they could plot values of $\Delta V/V_o$ as a function of the ratio of A_m/V_o, as defined in equation 2.40.

Subsequently, Δv_m and ε_v were determined as slope and intercept of the lines, respectively, corresponding to various values of confining pressure. Δv_m then was plotted in relations with confining pressure and mean grain size. Curve fitting of $\Delta v_m - \log\sigma_3$' response gave a nearly linear relationship. Its slope, S, which is later called normalized unit penetration/compliance, is membrane penetration induced volume change per unit area of membrane per log-cycle change in effective confining pressure). Influence of mean grain size d_{50} on S was found by plotting them together, with the former on log scale, and the obtained relation given by:

$$S = 0.014 \log d_{50} - 0.001 \qquad (2.42)$$

Kiekbusch and Schuppener (1977) tested on a wider range of soil types, from medium sand (d_{50}=0.4mm) to silty clay (d_{50}=0.002mm). Although they did not arrive at a formula, a nonlinear curve expressing correlation between D_{50}, which is even in log scale, and S (see Figure 2.5)

Ramana and Raju (1982) processed the data from earlier studies differently by displaying them on log-log scale, and S versus d_{50} curves appeared approximately as two linear segments (see Figure 2.6) described as follows:

$$\log S = 0.21 \log d_{50} - 2.77 \text{ for } 0.001\text{mm} \leq d_{50} \leq 0.08\text{mm} \tag{2.43}$$

$$\log S = \log d_{50} - 1.9 \text{ for } 0.08\text{mm} \leq d_{50} \leq 2\text{mm} \tag{2.44}$$

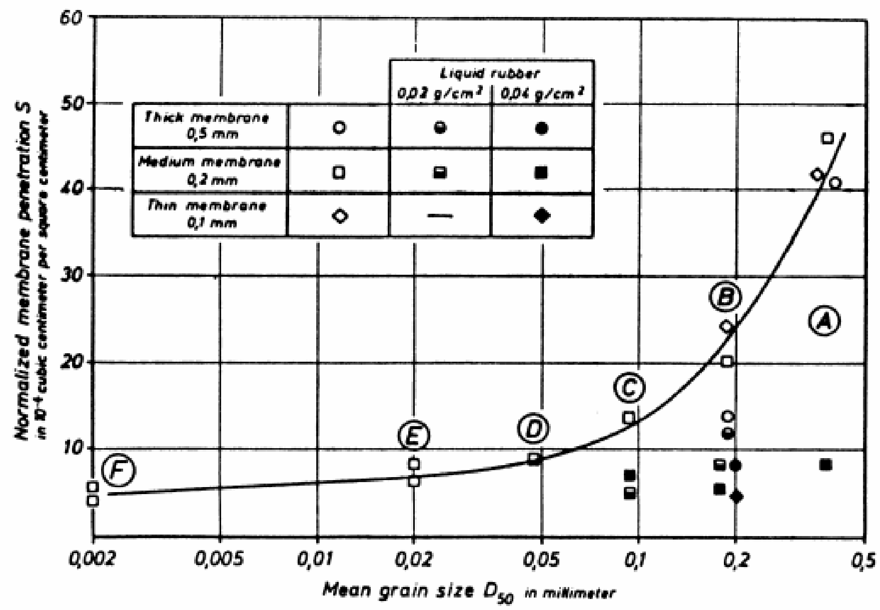

Figure 2.5. Relationship between S and d_{50} (Kiekbusch and Schuppener, 1977)

Nicholson, *et al.* (1993) re-assessed relation between normalized unit penetration and representative particle size. They performed tested on many types of sands and gravels, which had d_{50} covering a wide range from 0.82mm to 56 mm, to determine S. The authors also included results from several previous researches. Values of S then were plotted versus d_{10}, d_{15}, d_{20}, d_{25} and d_{50} of materials separately to compare and find least scattered relationship. d_{20} was concluded to provided strongest correlation with S in form of a polynomial equation as follows:

$$S = 0.0019 + 0.0095 d_{20} - 0.0000157 d_{20}^2 \tag{2.45}$$

where:

- S: normalized unit penetration [mL/cm^2 per log cycle of σ'_3 in kPa]
- d_{20}: particle-size index, [mm]

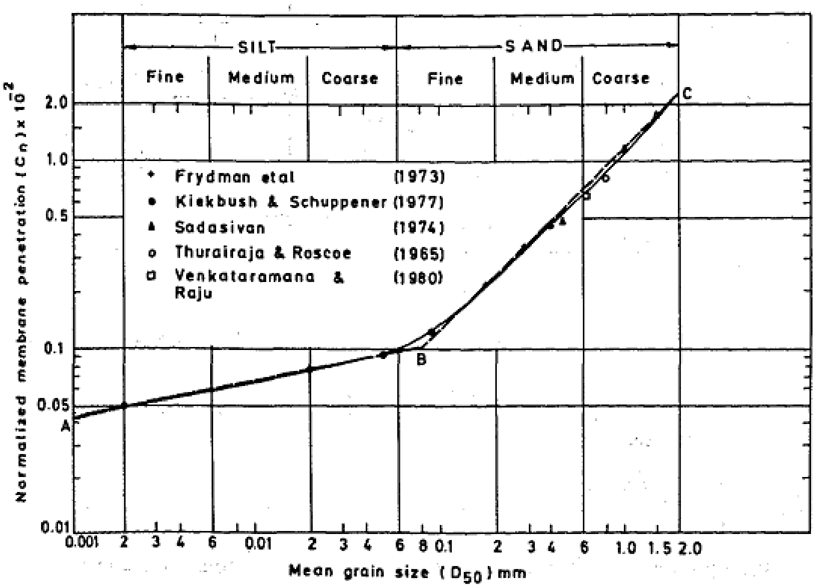

Figure 2.6. Membrane penetration in relation with mean grain size (Ramana and Raju, 1982)

Unit membrane penetration could be determined by:

$$\Delta v_m = S \log(\sigma'_3 / \sigma'_{3i}) \tag{2.46}$$

Then volume change due to membrane penetration is given by

$$\Delta V_m = \Delta v_m A_m = \frac{4V_o}{D_o} S \log(\sigma'_3 / \sigma'_{3i}) \tag{2.47}$$

where:

- σ'_{3i} : initial effective stress on specimen, either at the end of saturation or consolidation
- $\sigma'_3 = \sigma'_{3i} + \Delta\sigma'_3$: final effective stress on specimen, either at the end of consolidation or shearing
- D_i and H_i: initial diameter and height of specimen,

2.4 Hyperbolic stress-strain curve

Hyperbolic stress-strain relationship or incremental linear elastic model was developed by Duncan and Chang (1970) and Duncan, *et al.* (1980) to capture soil non-linearity and stress-dependent nature. In many finite element analyzing packages, hyperbolic model is considered as improvement of Mohr-Coulomb model. The stress-strain response is built based on tangent modulus at different stress condition as follows:

$$E_t = \left[1 - \frac{R_f(1-\sin\phi)(\sigma'_1 - \sigma'_3)}{2c\cos\phi + 3\sigma'_3\sin\phi}\right]E_i \qquad (2.48)$$

Where:

- $E_i = KP_a\left(\dfrac{\sigma'_3}{P_a}\right)^n$ is initial tangent modulus (2.49)
- $\phi = \phi_1 - \Delta\phi\log\left(\dfrac{\sigma'_3}{P_a}\right)$ is friction angle (2.50)
- P_a=100 kPa is atmospheric pressure
- R_f is value ratio, and is always less than 1

- K is modulus number,
- n is modulus exponent
- c is soil cohesion, for sandy soil c=0

E_i and R_f could be determined by transforming stress-strain curve in to hyperbolic form (see Figure 2.7). R_f is defined as ratio of stress difference at failure to asymptotic value. Duncan and Chang (1970) suggested R_f in between 0.75 and 1 based on various testing results of soils. Later, Duncan, *et al.* (1980) and Byrne, *et al.* (1987) found out R_f could be as low as 0.51.

K, n, ϕ_1 and $\Delta\phi$ are defined by performing triaxial tests at different confining pressures on samples at the same relative density. For sand, n = 0.5 has been used in numbers of studies (Seed and Idriss, 1970, Seed, *et al.*, 1986, Byrne, *et al.*, 1987) and n can be accepted as constant for a type of soil although it can vary with relative density (Duncan and Chang, 1970, Duncan, *et al.*, 1980). Byrne, *et al.* (1987) summarized testing data from the investigation by Duncan, *et al.* (1980) and found out that R_f was dependent on soil relative density and confining pressure. Therefore, they suggested computing R_f as a function of friction angle as follows:

$$R_f = 0.9\frac{\phi_{cv}}{\phi} \tag{2.51}$$

Where: $\phi_{cv} = \phi_p - \phi_{dil}$

- ϕ_{cv}: friction angle when sample reach steady state,
- ϕ_{cv}: peak friction angle
- ϕ_{dil}: dilatancy angle

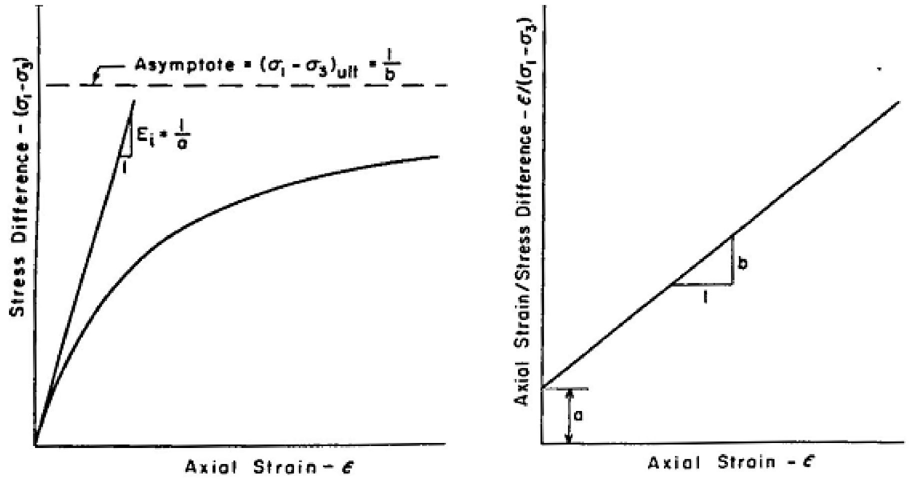

Figure 2.7. Determination of E_i and $(\sigma_1\text{-}\sigma_3)_{ult}$ (Duncan and Chang, 1970)

2.5 P-y curve

Beam on nonlinear Winkler foundation (BNWF) approach using p-y relationship has been the main method in analyzing laterally loaded pile. The analysis can be performed analytically or numerically with discretized nonlinear springs representing soil behavior. P-y curve describes nonlinear relationship between soil reaction to pile lateral deflection at given depth. Soil reaction is in form of load per unit length and could be understood as equivalent resultant of pressure by surrounding soil on pile.

P-y curves are determined by regression analysis of pile load test (Matlock, 1970, Reese, *et al.*, 1974, Georgiadis, 1983, O'Neill and Murchison, 1983). Reese, *et al.* (1974) performed tests on piles embedded in sand and back analyzed p-y curves for short-term static and cyclic loading and related them to pile diameter (D), and soil effective unit weight (γ'), friction angle (ϕ) and modulus of subgrade reaction (k_h). O'Neill and Murchison (1983) developed further the study and the results were adopted in American Petroleum Institute (API) recommendations. API p-y relationships also were implemented later in developing p-y curves for cyclic and dynamic loadings (Naggar and Bentley, 2000, Pranjoto and Pender, 2003, Allotey and El Naggar, 2008).

Other authors improved API curves by data of in-situ testing methods. Robertson (1989) used soil properties obtained from flat dilatometer testing (DMT) to generate p-y curves. Gabr and Borden (1988) and Gabr, *et al.* (1994) determined modulus of subgrade reaction from DMT reading. Marchetti*, et al.* (1991) developed a straightforward procedure to construct API p-y curves for clay from DMT reading and index. Another method is converting pressure expansion curve of pressuremeter tests to p-y curves (Briaud*, et al.*, 1984, Robertson*, et al.*, 1985, Bouafia, 2007).

API recommended p-y relation (API, 2000) is expressed as :

$$p = Ap_u \tanh\left(\frac{k_h z}{Ap_u} y\right) \qquad (2.52)$$

where:

- z: depth of interest,
- $\begin{cases} A = 0.9 \quad \text{for cyclic loading} \\ A = \max\{0.9; 3 - 0.8z/D\} \text{ for static loading} \end{cases} \qquad (2.53)$
- D: pile diameter,
- k_h: modulus of subgrade reaction (see Figure 2.8)
- $p_u = \min\{(C_1 z + C_2 D)\gamma' z; C_3 D\gamma' z\}$: ultimate soil resistance per unit length,
- $C_1 = \frac{K_0 \tan\phi \sin\beta}{\tan(\beta-\phi)\cos\alpha} + \frac{\tan^2\beta \tan\alpha}{\tan(\beta-\phi)} + K_o \tan\beta(\tan\phi \sin\beta - \tan\alpha) \qquad (2.54)$

- $C_2 = \frac{\tan\beta}{\tan(\beta-\phi)} - K_a$ (2.55)

- $C_3 = k_0 \tan\phi \tan^4\beta + k_a(\tan^8\beta - 1)$ (2.56)

- $\alpha = \phi/2, \beta = 45 + \phi/2, K_0 = 0.4, \text{ and } K_a = \tan^2(45 - \phi/2)$

It is noteworthy that p-y curves by API recommendation for cyclic and static load are identical except for depths satisfying $3 - 0.8z/D > 0.9$, which yields z < 2.625D. This zone is relatively small in comparison with typical pile length, except some special cases like caissons.

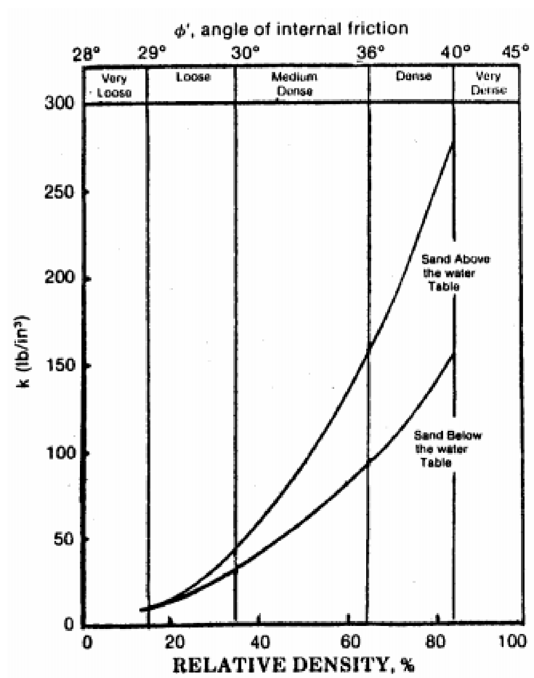

Figure 2.8. Modulus of subgrade reaction (API, 2000)

Although k_h is commonly selected based on friction angle, Figure 2.8 suggests that it is can be chosen from relative density, which likely results in a different k_h from value given by ϕ. Initial slope of API p-y curves is linearly proportional to depth. Previous studies concluded that API k_h overestimated stiffness of soil at depth greater than few times pile diameter (Yan and Byrne, 1992, Boulanger, *et al.*, 2003). Authors did not clarify whether it was selected by friction angle or relative density. Boulanger*, et al.* (2003) suggested to apply a correction for effect of overburden stress on k_h as follows:

$$k_h^* = c_\sigma k_h = \sqrt{\frac{\sigma'_{ref}}{\sigma'_{vo}}} k_h \tag{2.57}$$

where:

- k_h^* : overburden stress corrected of subgrade reaction
- σ'_{ref} : reference stress at which k is calibrated, taken as 50 kPa
- σ'_{vo} : effective overburden stress at point of interest,

Based on Mobilized Strength Design concept (Osman and Bolton, 2005) Bouzid, *et al.* (2013) proposed a new approach to develop p-y curve from stress-strain response resulted from undrained triaxial test on clay by using two converting coefficients N_c and M_c (Figure 2.9). N_c is actually modified bearing capacity factor for cohesion. The authors suggested different values of coefficients in three segments of stress-strain curve to circumvent abrupt incline in p-y curve as follows:

$$p = \Delta\sigma_1 N_c D \tag{2.58}$$

$$y = \varepsilon_a D / M_c \tag{2.59}$$

where:

- M_c=2.6 in all segments

- From origin to half maximum stress difference: N_c= 11.23 (smooth interface) and N_c= 17.86 (rough interface). From half to maximum stress difference: N_c gradually decreases to 9. After peak: N_c=9,

No procedure on converting stress-strain relationship to p-y curve for sand has been reported. This study will suggest new formulas using the form of equations 2.58 and 2.59; however, N_c will be replaced by another bearing capacity factor, which is N_q

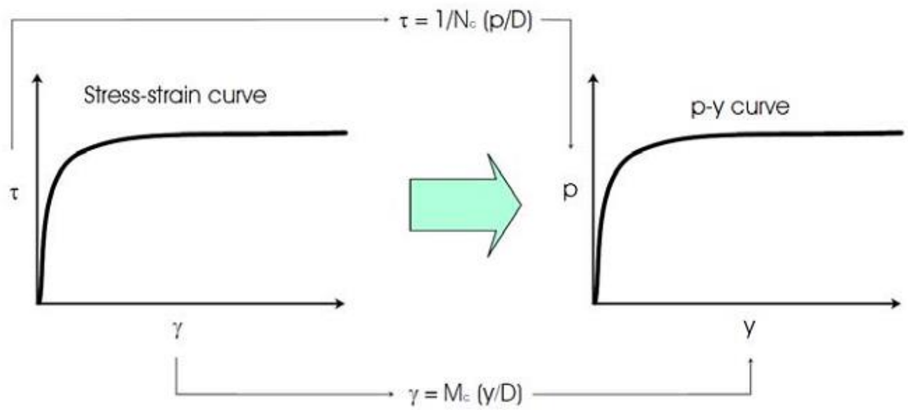

Figure 2.9. Converting stress-strain curve to p-y curves by scaling factors N_c and M_c (Bouzid, *et al.*, 2013)

2.6 Soil testing program

2.6.1 Classification tests

2.6.1.1 Particle-size distribution

Particle-size analysis was performed following ASTM D422-63 (Reapproved 2007). Four samples were taken from sand dump, and in the pit before pile tests 1 and 2 as in Table 2.4. Outcomes are presented in Figure 2.10 and Table 2.5

The results show that soil is clean sand, of which less than 4% of soil mass is fine (d<0.075mm), about 62% is fine sand (0.075mm ≤ d<0.42mm) and 34% of medium sand

(0.42mm ≤ d<2mm). Soil is classified as poorly graded sand (SP) according to Unified Soil Classification System (USCS) and as A-3 in AASHTO classification system. Since fine content was less than 4%, Atterberg limits tests for fines were not conducted.

Table 2.4. Samples for particle-size analysis

Pile test	Sample	Location	Depth (m)
N/A	#0.1	Sand dump	N/A
1	#1.1	Soil pit	0.15
1	#1.2	Soil pit	0.50
2	#2.1	Soil pit	0.15

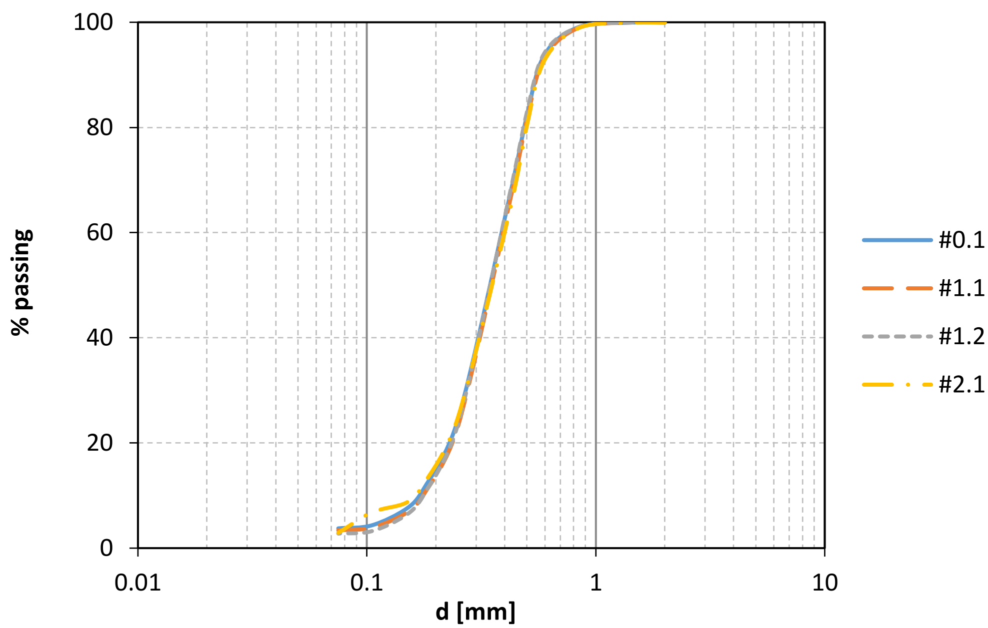

Figure 2.10. Particle-size distribution

Table 2.5. Particle-size distribution parameters

d_{10} (mm)	d_{20} (mm)	d_{30} (mm)	d_{50} (mm)	d_{60} (mm)	C_u	C_g
0.17	0.21	0.26	0.33	0.4	2.4	1.0

2.6.1.2 Specific gravity test

Specific gravity was determined following ASTM D854-14. Three dry and one wet (with known moisture content) samples were tested in four different water pycnometers. Outcomes are presented in Table 2.6. Average value is 2.66

Table 2.6. Specific gravity tests

Test	Initial condition	Gs
1	Dry	2.67
2	Dry	2.65
3	Dry	2.67
4	Wet	2.67

2.6.1.3 Minimum and maximum index void ratio (e_{min} and e_{max})

Degree of packing of sand particles is described as relative density given by:

$$D_R = \frac{e_{max} - e}{e_{max} - e_{min}} \tag{2.60}$$

where:

- e is in-situ void ratio
- e_{max} and e_{min} are void ratios of loosest and densest samples obtained in lab testing

Since it is very difficult to have undisturbed samples for determining e in practice, D_R is normally determined by empirical correlations with in-situ test data, such as SPT, CPT and DMT. However, as they were not available in this projects, index void ratios e_{max} and e_{min} are the essential for determining soil relative density.

ASTM D4253-14 and D4254-14 provide guidance on determination of e_{min} and e_{max}, respectively. Several attempts were performed for each case and average values of five attempts with consistence within 2% were recorded as index void ratios (Table 2.7) Maximum and minimum dry density were calculated as $16.2\,\mathrm{kN/m^3}$ and $13.7\,\mathrm{kN/m^3}$, respectively. Ratio of $\frac{\gamma_{d,min}}{\gamma_{d,max}} = 0.84$ is within the statistical data reported by Mayne, *et al.* (2001)

Table 2.7. e_{max} and e_{min}

Attempt	e_{max}	e_{min}
1	0.9109	0.6166
2	0.9082	0.61085
3	0.9059	0.6076
4	0.9048	0.6134
5	0.8987	0.6162
Average	0.91	0.61

2.6.2 Axial compression triaxial tests

2.6.2.1 Testing procedure

Sixteen axial compression triaxial tests were performed to determine soil shear strength parameters and stress-strain relationship. All tests were consolidated-drained (CD) following procedure recommended by ASTM D7181-11. Samples were prepared at void ratios of 0.85, 0.79, 0.75 and 0.7 corresponding to initial relative density of 20%, 40%, 53% and 70%, respectively. Specimens at certain density were tested at four confining pressures of 25 kPa, 50 kPa, 100 kPa, 200 kPa. Dry unit weight of samples is presented in Table 2.8.

Samples aspect ratio fell between 1.93 and 2.07. Latex membranes had nominal diameter of 7.1cm and thickness of 0.3mm. Dry soil was deposited inside stretched membrane by dry funnel method with low drop height. To ensure sample consistency, funnels were capable to provide enough soil for sample in one attempt. Specimen void ratio was controlled by funnel spout opening. Loose samples were prepared with large opening while dense sample with smaller one or stopper and additional tapping on the mold sides.

Both ends of a specimen were restrained, filter papers and porous stones were placed at both ends to ensure water drainage and filtration. Specimens was held by suction of 5kPa while apparatus wall and top were being assembled. The cell then was filled with de-aired water and placed in testing device. A seating pressure of from 10 to 30 kPa was set on samples,

Specimens were saturated in two steps. First was water circulation under water head caused by de-aired water tank and vacuum pressure of about 2 kPa. Water flowed through sample from bottom to top to avoid densification. The circulation volume was greater than three times specimen volume. This method was very effective as sample after circulation has initial B-values between 0.83 and 0.91 and thus helped reducing back pressure value and time. Second stage was back pressure. In this stage, effective stress was set equal to seating stress and range of back pressure was from 100 to 175 kPa. All specimen had B-values of 0.95 or higher after saturation to enter isotropic or K_0 consolidation and shear stages.

During testing, axial load, axial deformation, cell pressure, back pressure, pore water pressure, and volumetric changes were automatically measured by electrical transducers and saved in computers. The shearing stage was strain-controlled with the rate of 1.75%/hour and maximum strain of 20%.

Table 2.8. Dry unit weight various relative density

D_R (%)	**20**	**40**	**53**	**70**
γ_d (kN/m^3)	14.1	14.6	14.9	15.3

2.6.2.2 Sample post-testing shape

All samples had bulging shape to some degree after testing, in which the ones at relative density of 53% and higher exhibited failure plane (see Figure 2.11). Therefore, area correction by cylindrical model will underestimate sample average area. This issue will be addressed later in this study,

(a) (b) (c)

Figure 2.11. Deformation of samples: (a) D_R=20%, (b) D_R=40% and (c) D_R=53%

2.6.2.3 Assessment of membrane penetration effect

Correction for volume change during saturation by ASTM-D7181 was made for samples before other factors are assessed.

Volume change of sample during consolidation is calculated by Nicholson, *et al.* (1993) equations 2.45, 2.46 and 2.47. Selected results are described in Table 2.9. Normalized unit penetration is given by:

$$S = 0.0019 + 0.0095d_{20} - 0.0000157d_{20}^{2} = 0.0039$$

Outcomes show that volume change by membrane intrusion could be 41% of total volume change for low pressure and around 10% to 15% for high pressure. However, due to volumetric train in consolidation is not significant, only as high as 1% for sample e085P20, effect of this phenomenon to specimen volume is marginal. Membrane compliance is also insignificant and could be neglected during shear, as discussed in following section on effect of membrane resistance,

Table 2.9. Effect of membrane penetration during consolidation

Sample	e_o	σ'_{sat} (kPa)	σ'_3 (kPa)	ΔV_c (cm^3)	ΔV_m (cm^3)	$\frac{\Delta V_m}{\Delta V_c}$
e085P25	0.85	15	25	0.41	0.14	0.35
e085P200	0.85	20	200	6.74	0.65	0.10
e079P25	0.79	15	25	0.39	0.14	0.35
e079P200	0.79	30	200	4.56	0.53	0.12
e075P25	0.75	10	25	0.78	0.26	0.33
e075P200	0.75	30	200	4.12	0.52	0.13
e070P25	0.70	10	25	0.66	0.27	0.41
e070P200	0.70	20	200	4.15	0.64	0.15

2.6.2.4 Assessment of membrane resistance

Corrections for membrane resistance are calculated for 4 samples: e085P200, e0.79P25, e0.75P100 and e0.70P50 by expressions of ASTM-D7181, Duncan and Seed

(1967) and Germaine and Ladd (1988). Cylindrical model for sample deformation is implemented. Membrane initial confinement (La Rochelle, *et al.*, 1988) is neglected since samples and membranes had almost the same diameter. Volume change of these sample during shear are illustrated in Figure 2.12,

- On radial stress correction:

It is obvious in Figure 2.13 that radial stress correction by Germain and Ladd's expression has identical shape as of volumetric strain. That means a contractive specimen (e085P200 for example) has membrane in compression circumferentially, which is not reasonable as sample diameter likely tends to increase from a certain strain in AC tests. In that sense, it can be concluded that Duncan and Seed's equation provides better estimation for contractant. Both equations predict better in sample with dilative behavior. Data suggests that these equations likely work well with axial extension (AE) which typically has decreasing specimen diameter during shear.

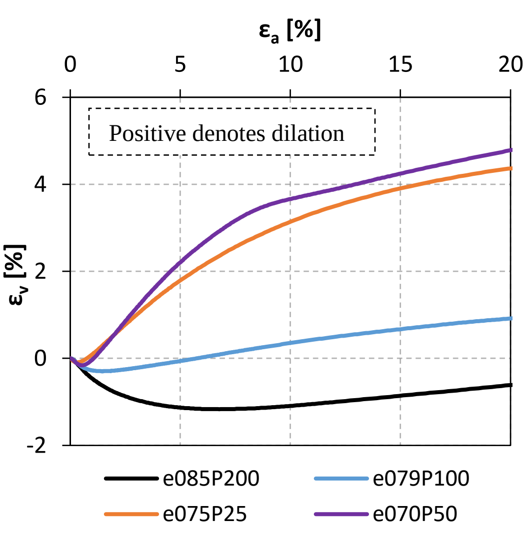

Figure 2.12. Volumetric strain of selected samples

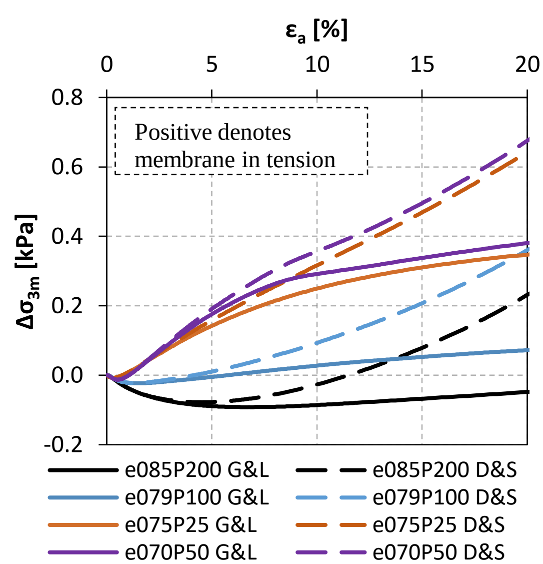

Figure 2.13. Radial stress correction by Duncan and Seed (D&S), and Germaine and Ladd (G&L) equations

Second point is that magnitude of radial membrane resistance is relatively low in comparison with confining pressure. It is only about 2% in sample with confinement of 25kPa and down to 0.1% in sample at 200 kPa. Therefore, radial stress correction is negligible in drained AC test and importantly, membrane compliance during shear is insignificant as well.

- On axial stress correction:

Figure 2.14 compares axial stress corrections by ASTM-D7181, Duncan and Seed (1967) and Germaine and Ladd (1988) recommendations. All methods show same trend. ASTM gives largest magnitude of correction in almost range of strain, except at axial strain lower than 10% in e0.85P200. Maximum corrections from above methods, and uncorrected stress differences at peak and at strain of 20% are presented in Table 2.10 and Table 2.11. Results of e085P25 are also added in the tables as the most-affected specimen. It can be seen that the corrections have slight impact on maximum stress difference. However, the constant volume strength could be moderately affected if membrane resistance is not corrected.

Table 2.10. Membrane axial stress correction at peak

Sample	e085P25	e085P200	e079P100	e075P25	e070P50
ε_a (%)	9.20	14.72	7.8	3.7	2.87
$\Delta\sigma_1$ (kPa)	76.9	509.9	275.7	92.5	198.5
$\Delta\sigma_{1m}$ (kPa)	-2.17	-3.48	-1.84	-0.88	-0.687

Table 2.11. Membrane axial stress correction at ε_a=20%

Sample	e085P25	e085P200	e079P100	e075P25	e070P50
$\Delta\sigma_1$ (kPa)	72.2	499.4	262.2	73.4	154.5
$\Delta\sigma_{1m}$ (kPa)	-4.7	-4.7	-4.7	-4.8	-4.8

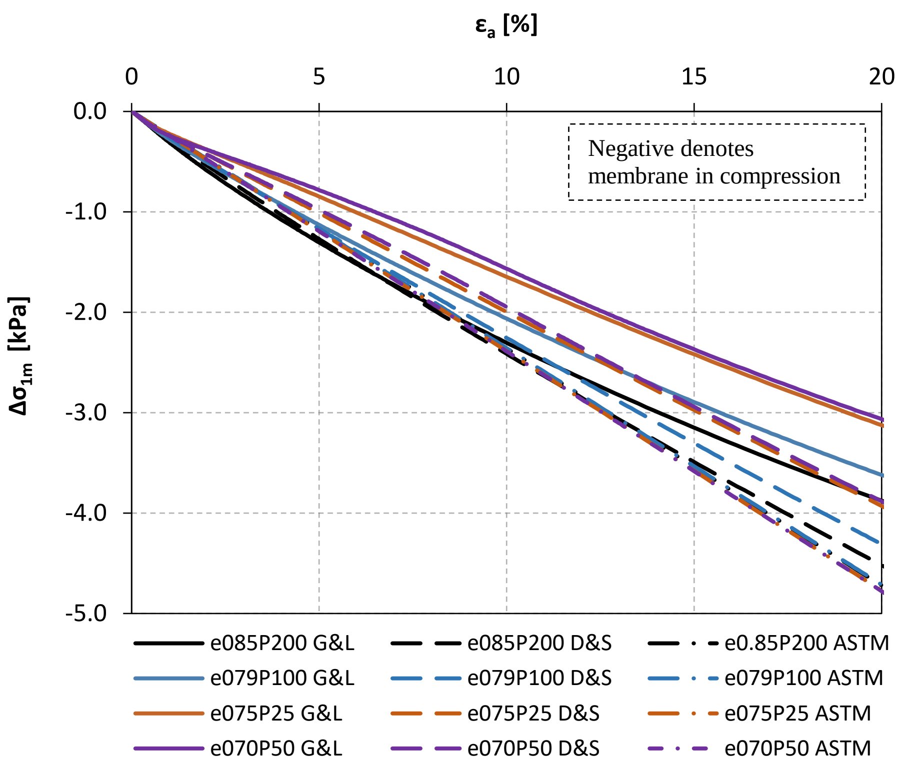

Figure 2.14. Axial stress corrections by equations of ASTM ASTM-D7181, Duncan and Seed (1967) and Germaine and Ladd (1988)

2.6.2.5 Assessment of cross-sectional area correction

Cross-sectional area correction is analyzed by using following general equation by Germaine and Ladd (1988) for bulging deformation:

$A_{\varepsilon} = A_{c}[(1-\varepsilon_{v})/(1-\alpha\varepsilon_{a})]$, with:

- ○ $\alpha = 1$ for cylindrical deformation,
- ○ $\alpha = 4/3$ for parabolic deformation,

This area correction also applied in axial membrane resistance correction by Germaine and Ladd (1988). Deviatoric stress-strain responses for the samples in two cases are illustrated in Figure 2.15 and some of their features are described in Table 2.12

and Table 2.13. It appears that using α=4/3 gives lower deviator stress and peak friction angle. Degree of reduction is proportional to sample void ratio, and the gap increases with increasing strain. Interestingly, strain at peak also decreases in samples at void ratio of 0.85 and 0.79, and difference in friction angle at strain of 20% at almost the same among samples.

Stress-strain curves with corrections recommended by ASTM also is plotted in Figure 2.15 and unsurprisingly they are almost identical to those obtained with α =1. This fact and others discussed previously lead to the conclusion that cross-sectional area correction is the most significant factors and should be considered in drained AC tests, followed by axial membrane resistance correction. Remaining factors as radial membrane resistance and membrane penetration are negligible.

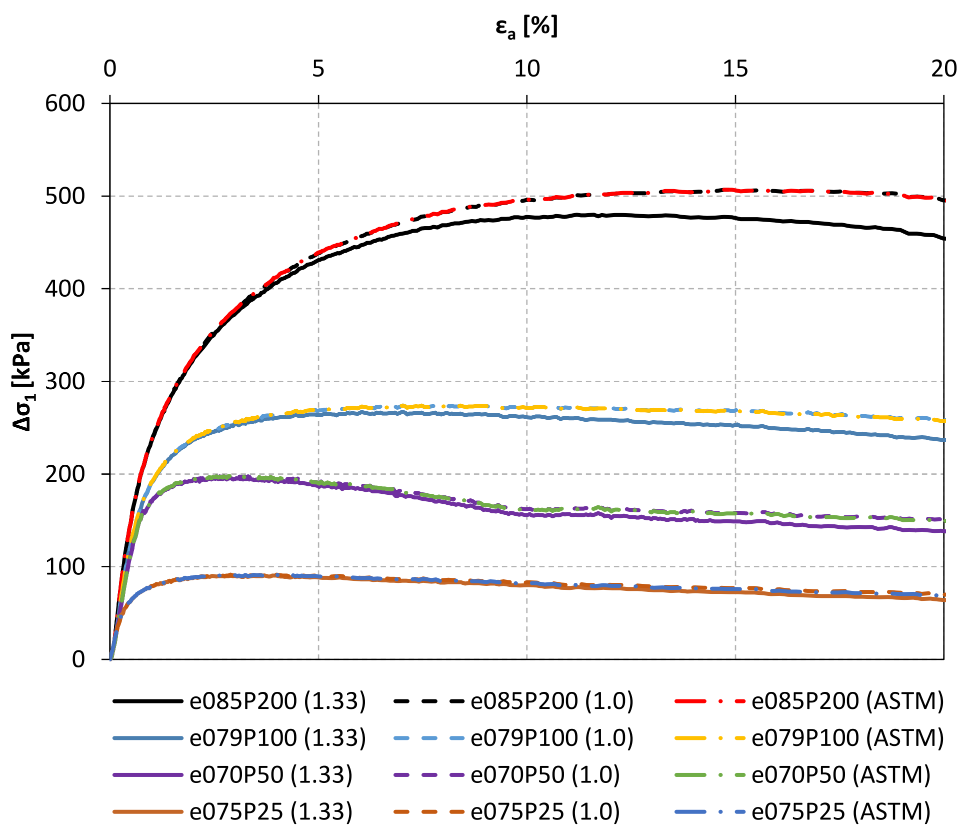

Figure 2.15. Effect of cross-sectional area on sample stress-strain curves

Table 2.12. Effect of cross-sectional area correction to deviatoric stress at peak

Sample	e085P200		e079P100		e075P25		e070P50	
	α=1	α=1.33	α=1	α=1.33	α=1	α=1.33	α=1	α=1.33
ε_a (%)	14.72	11.2	7.8	6.04	3.7	3.7	2.87	2.87
$\Delta\sigma_1$ (kPa)	506.8	497.9	274.1	267.1	91.9	90.7	198	196
ϕ_p (deg)	34.0	33.1	35.3	34.8	40.5	40.2	41.5	41.3

Table 2.13. Effect of cross-sectional area correction to deviatoric stress at ε_a=20%

Sample	e085P200		e079P100		e075P25		e070P50	
	α=1	α=1.33	α=1	α=1.33	α=1	α=1.33	α=1	α=1.33
ε_a (%)	20	20	20	20	20	20	20	20
$\Delta\sigma_1$ (kPa)	495.6	454.3	258.3	236.9	70.3	64.2	151.5	138.9

2.7 Testing Results

2.7.1 Stress difference-strain response and initial modulus

Stress-strain responses for samples are built including all above corrections (Figure 2.16 to Figure 2.19). Corrections for membrane resistance and cross-sectional area are computed by Germaine and Ladd (1988) equations. Bases on deformation shape of specimen coefficient α=4/3 is applied for area correction.

Initial tangent modulus for each sample is determined by transforming stress-strain curve into hyperbolic form (Duncan and Chang, 1970). Results are presented in Table 2.14. Ratio of E_i/P_a is plotted versus σ_3' / P_a to perform curve fitting for K and n. It can be seen that n=0.52 and values of K are described in Table 2.15 and Figure 2.20**.** A relation between K and D_R is determined by curve fitting and it appear to be linear. This result is in good agreement with the average line of tests by (Duncan*, et al.*, 1980) (see Figure 2.21 and Figure 2.22). The relation is given by:

$$K = 10.36D_R + 90 \tag{2.61}$$

where: D_R is soil relative density in percent

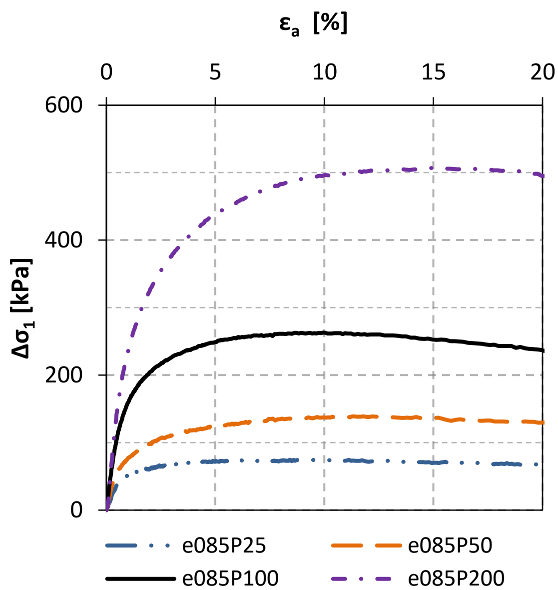

Figure 2.16. Stress-strain responses for samples at e=0.85

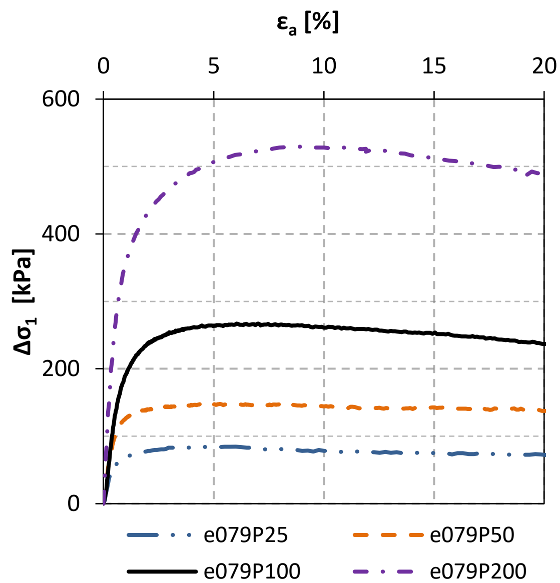

Figure 2.17. Stress-strain responses for samples e=0.79

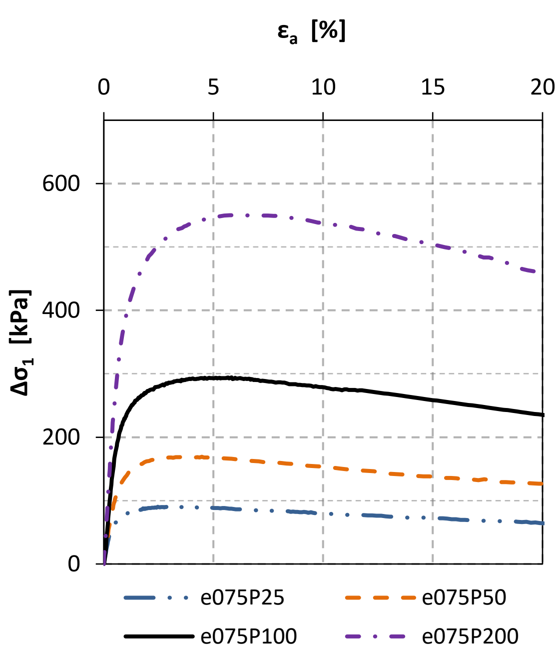

Figure 2.18. Stress-strain responses for samples at e=0.75

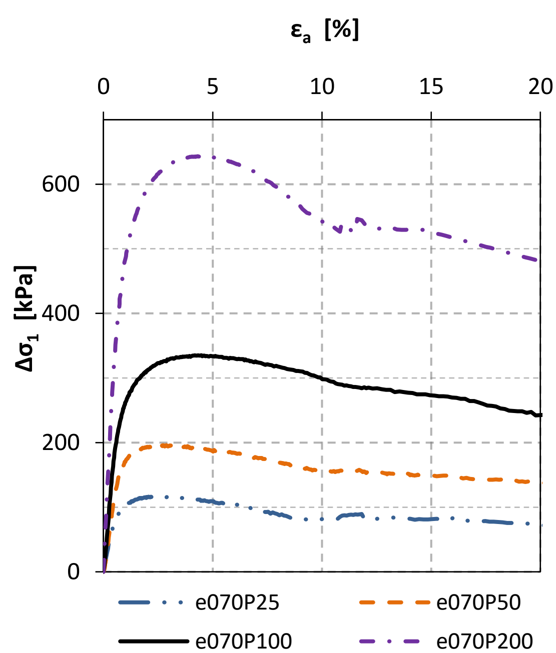

Figure 2.19. Stress-strain responses for samples at e=0.70

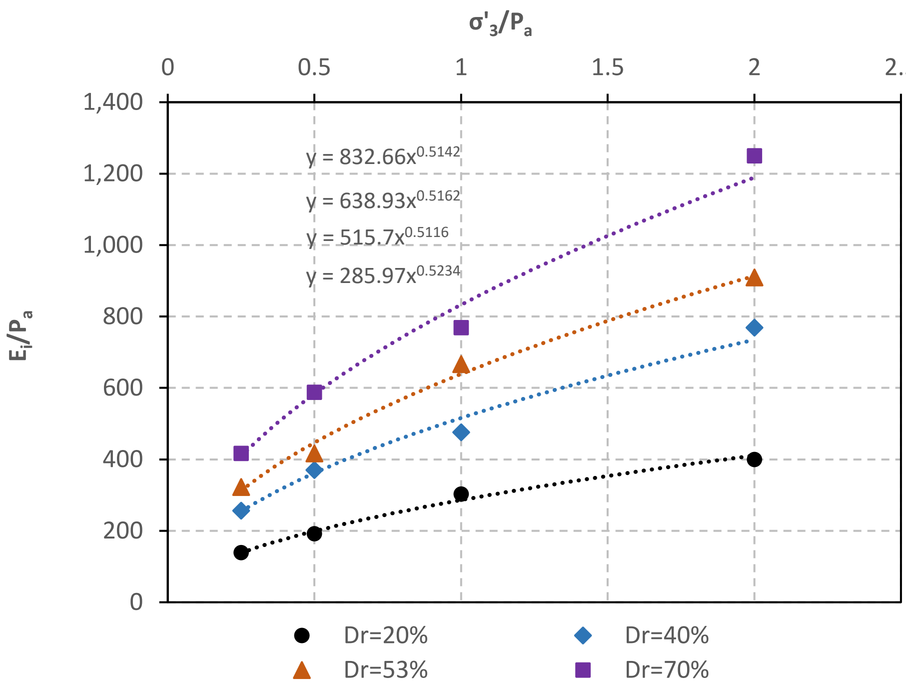

Figure 2.20. E_i / P_a - σ'_3/P_a relation at different relative densities

Table 2.14. Initial modulus [kN/m^2] at various relative density and confinement

D_R (%)	σ'_3 / P_a			
	0.25	**0.5**	**1.0**	**2.0**
20	13,890	19,230	30,300	40,000
40	25,650	37,040	52,630	76,920
53	32,260	41,670	66,670	90,910
70	41,670	58,820	76,923	125,000

Table 2.15. Modulus number K at various relative density

D_R (%)	20	40	53	70
K	286	516	638	832
n	0.52	0.51	0.52	0.51

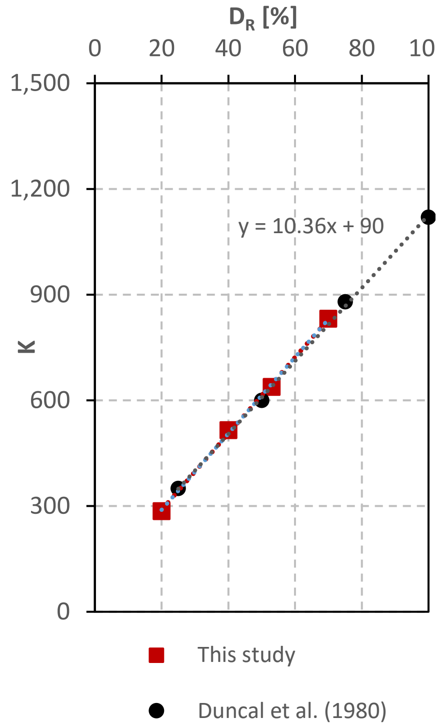

Figure 2.21. K – DR relation

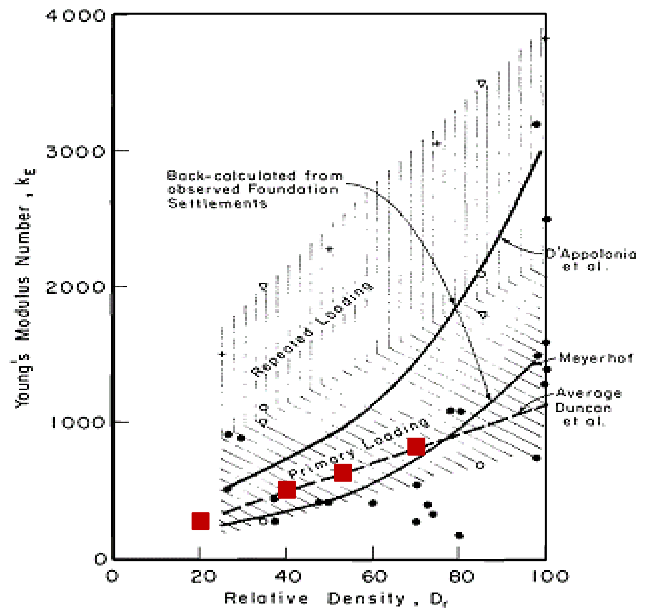

FIG. 14. Comparison of back-calculated and measured k_E values. ● Duncan *et al.* (1980), primary loading; + Seed and Idriss (1970), repeated loading; ○ Lambe and Whitman (1968), primary loading; ▽ Lambe and Whitman (1968), repeated loading.

Figure 2.22. Comparison of obtained result with earlier studies (Byrne, *et al.*, 1987)

2.7.2 Shear strength parameters

2.7.2.1 Friction angle

Friction angle is computed at peak and the results are presented in Table 2.16 and Figure 2.23. Curve-fitting of peak friction angle values gives figure at confinement of atmospheric pressure ϕ_1 and its change per log-cycle of pressure $\Delta\phi$ (Table 2.17)

Table 2.16. Peak friction angle [deg] at various relative density and confinement

D_R (%)	σ'_3 / P_a			
	0.25	**0.5**	**1.0**	**2.0**
20	36.3	34.9	34.7	33.1
40	39.1	36.7	34.8	34.2
53	40.2	39.1	36.4	34.6
70	44.2	41.3	38.8	37.2

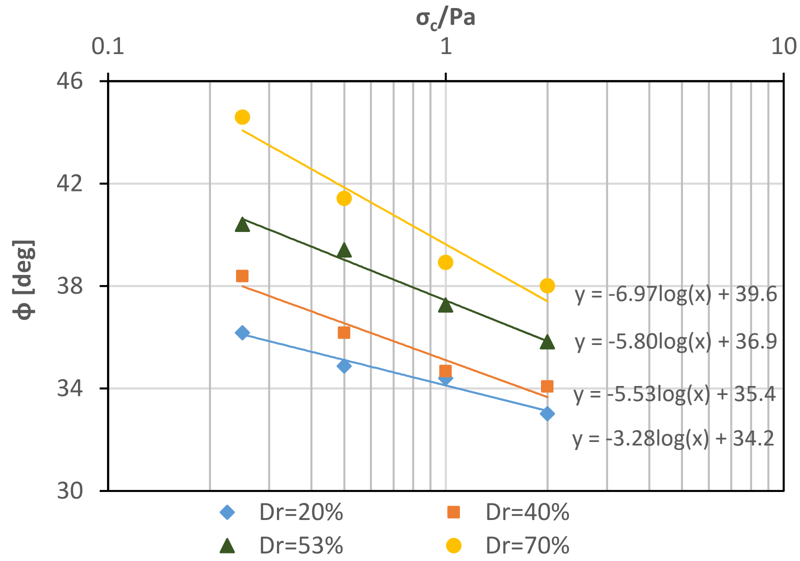

Figure 2.23. Stress-dependent peak friction angle

Table 2.17. Friction angle parameters at various relative density

D_R (%)	20	40	53	70
ϕ_1 (deg)	34.2	35.4	36.9	39.6
$\Delta\phi$	3.28	5.53	5.80	6.97

2.7.2.2 Dilatancy angle and failure ratio

Stress-dependent friction angle model, which is described by equation 2.50 ((Duncan, *et al.*, 1980), and a later study by Byrne and Eldridge (1982) indicated that when confining pressure is sufficiently large, peak friction angle is equal to constant volume friction angle and soil dilation is completely suppressed. For a given soil, at a given confining pressure, peak friction angle varies with relative density; however, constant volume friction angles of samples at density state are identical (Figure 2.24). Since samples were tested at confining pressure of up to 200 kPa, constant volume friction angle is determined by finding intersection of extended trendlines of peak friction angle (Figure 2.25). The obtained constant volume friction angle is 32 (deg). Dilatancy angle is determined from peak and constant volume friction angles and its values are illustrated in Table 2.18. Table 2.19 shows failure ratios at different relative densities, which are computed by equation 2.51. A summary on soil classification and triaxial testing results is presented in Table 2.20 as a reference set of soil properties for numerical analysis using hyperbolic model or similar.

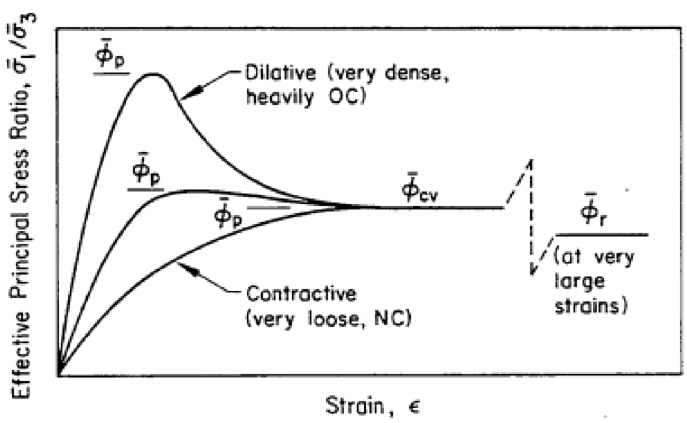

Figure 2.24. Constant volume friction angle of dilative and contractive specimens (Kulhawy and Mayne, 1990)

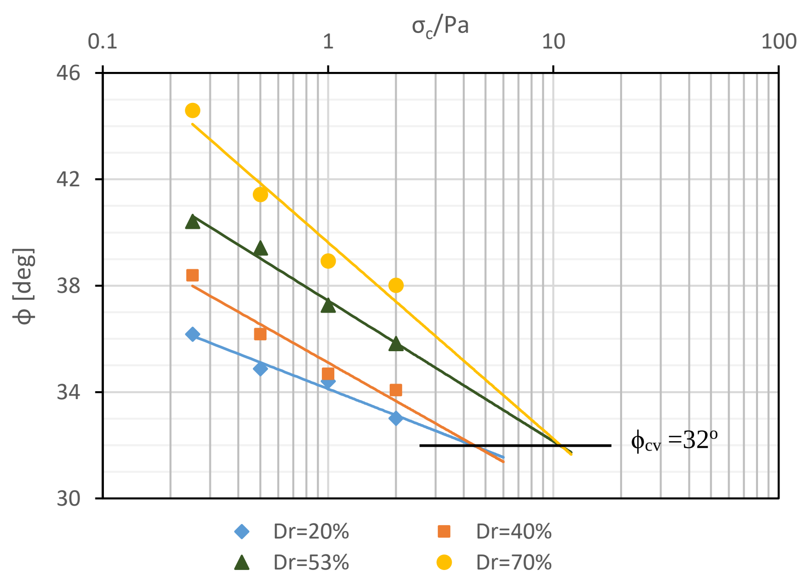

Figure 2.25. Determining constant volume friction angle

Table 2.18. Dilatancy angle [deg] at various relative density and confinement

D_R (%)	σ'_3 / P_a			
	0.25	**0.5**	**1.0**	**2.0**
20	4.3	2.9	2.7	1.1
40	7.1	4.6	2.8	2.5
53	8.3	7.1	4.4	3.4
70	12.2	9.3	6.8	6.1

Table 2.19. Failure ratio at various relative density

D_R (%)	20	40	53	70
R_f	0.86	0.83	0.79	0.74

Table 2.20. Summary of soil parameters in relation with relative density

D_R (%)	γ_d (kN/m3)	K	n	ϕ_1 (deg)	$\Delta\phi$	R_f
20	14.1	286	0.52	34.2	3.28	0.86
40	14.6	516	0.52	35.4	5.33	0.83
53	14.9	638	0.52	36.9	5.80	0.79
70	15.3	832	0.52	39.6	6.97	0.74

2.8 P-y curves for soil

2.8.1 P-y curve by API recommendations

P- curves are computed at depths that give vertical overburden pressure of 25 kPa, 50 kPa and 75 kPa. Input for p-y curve generating is described in Table 2.21 and the outcomes are shown in Figure 2.26 to Figure 2.29. Modulus of subgrade reaction (k_h) is chosen based on ϕ_1 (Figure 2.8). Ultimate reactions of curves are presented in Table 2.22, in which A is coefficient for ultimate resistance computed by equation 2.53. The generated p-y curves are for both cyclic and static loading since for D=0.32m, the zone that has those types of curve different one from other is 0.84m. Data points of p-y curves are tabulated in Appendix A

Table 2.21. Input for API p-y curves

D_R (%)	γ_d (kN/m^3)	z_1 (m)	z_2 (m)	z_3 (m)	ϕ_1 (deg)	k_h (kN/m^3)
20	14.1	1.77	3.55	5.32	34.2	31,200
40	14.6	1.71	3.42	5.14	35.4	39,400
53	14.9	1.68	3.36	5.03	36.2	48,900
70	15.3	1.63	3.28	4.90	39.6	71,900

Table 2.22. Ultimate soil reaction, Ap_u, of API p-y curves

D_R (%)	γz_1 =25 kN/m	γz_2 =50 kN/m	γz_3 =75 kN/m
20	134.1	489.2	1049
40	143.6	232.8	1142.2
53	159.6	584.4	1274.2
70	194.9	669.1	1569.1

2.8.2 Proposed procedure to convert triaxial stress-strain curve to p-y curve

Static API-similar p-y curve converted from sandy soil triaxial stress-strain curve has two components computed by equations in the form proposed by (Bouzid, *et al.*, 2013):

$$p = \Delta\sigma_1 N_s D \tag{2.62}$$

$$y = \varepsilon_a D / M_s \tag{2.63}$$

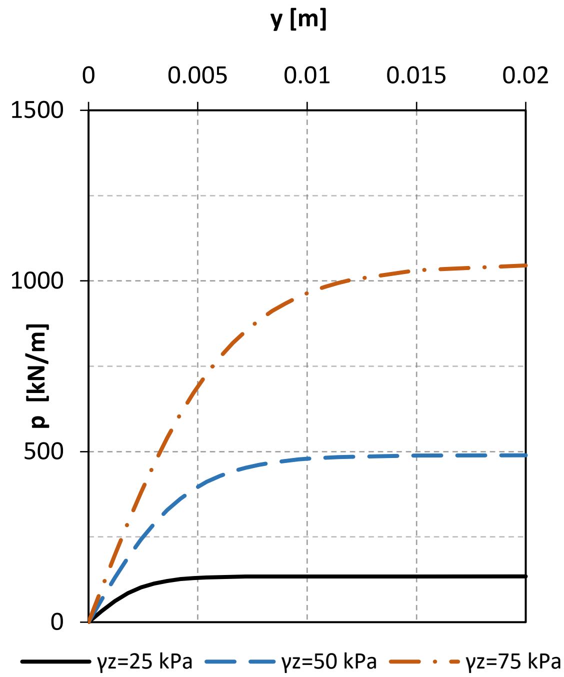

Figure 2.26. p-y curves at depths for soil with D_R=20%

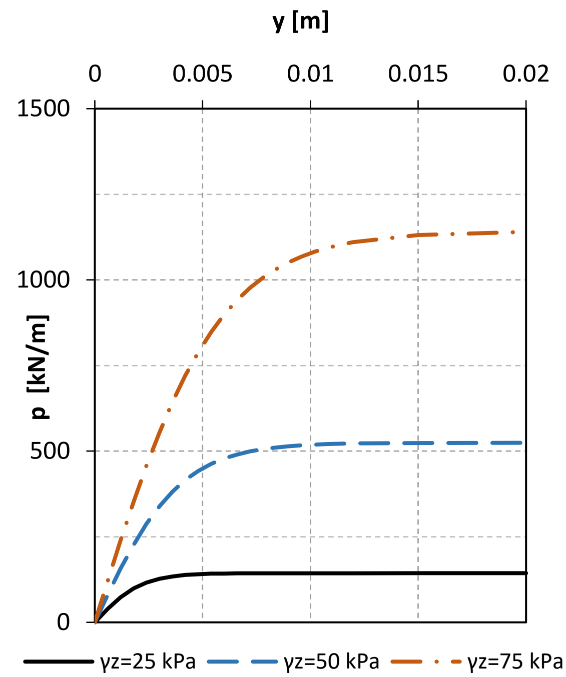

Figure 2.27. p-y curves at depths for soil with D_R=40%

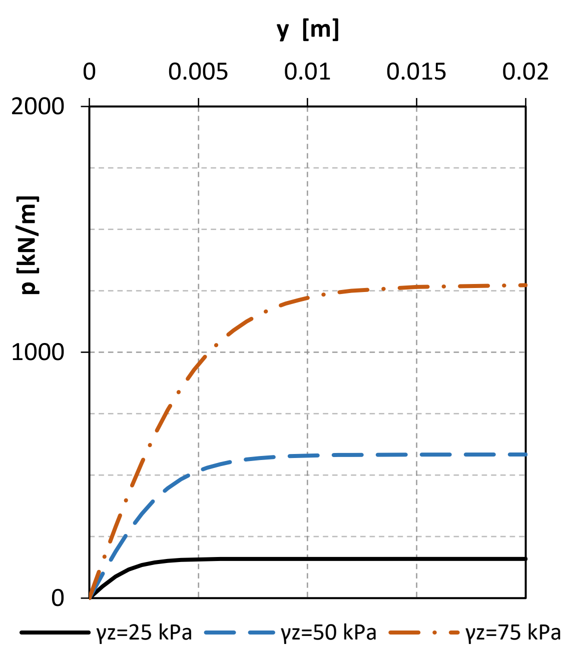

Figure 2.28. p-y curves at depths for soil with D_R=53%

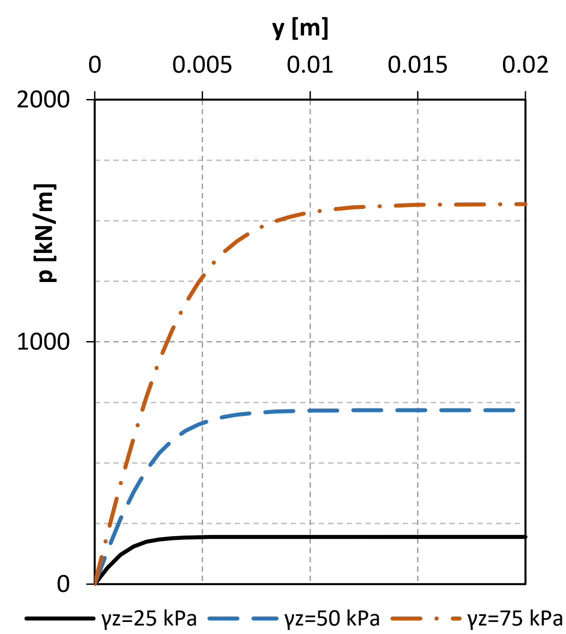

Figure 2.29. p-y curves at depths for soil with D_R=70%

The p-y curve will have following properties:

- Only the up-to-peak segment of stress-strain curve, $\varepsilon_a \le \varepsilon_p$, in used
- The converted p-y curve will have ultimate soil reaction similar to that of API one
- The converted p-y curve will have displacement at Ap_u similar to that of API one

Reese, *et al.* (1974) suggested typical pile deflection that mobilize ultimate soil reaction is 3D/80 (Figure 2.30). Therefore, coefficient M_s can be determined by:

$$\frac{3D}{80} = \varepsilon_{ap} D M_s \qquad (2.64)$$

$$M_s = \frac{80\varepsilon_{ap}}{3} = 26.7\varepsilon_{ap} \qquad (2.65)$$

$$y = \frac{3D}{80}\frac{\varepsilon_a}{\varepsilon_{ap}} \qquad (2.66)$$

where: ε_{ap} is axial strain at peak of stress-strain curve

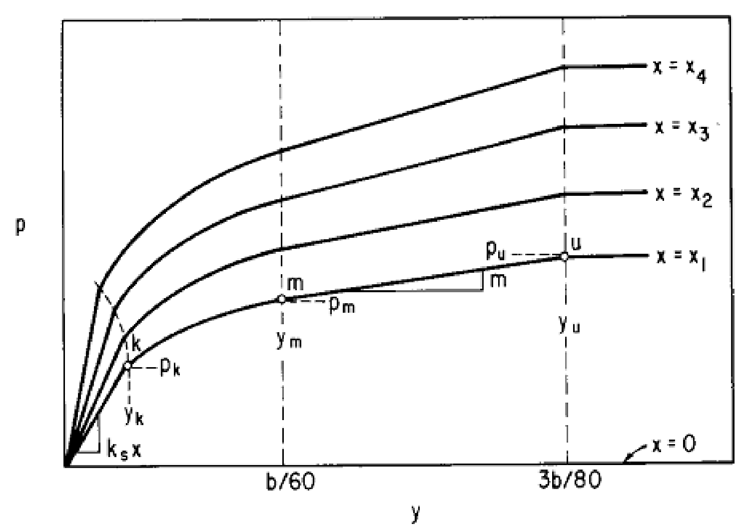

Figure 2.30. Characteristic shape of p-y curve for sand (Reese, *et al.*, 1974)

N_s is determined based on a finding of that all API p-y curves for depths bearing overburden pressures of 25 kPa, 50 kPa and 75kPa appear to have $p_u = (C_1 z + C_2 d)\gamma' z$ (C_1 and C_2 as in equations 2.54 and 2.55, respectively), which means they have shallow failure wedge. Therefore, p_u can be related to bearing capacity factors N_γ or/and N_q of shallow foundation. For simplicity, $N_q = tg^2\left(\frac{\pi}{4}+\frac{\phi'}{2}\right)e^{\pi tg\phi'}$ by Vesic is selected to participate in scaling coefficient N_s. It is assumed N_s=mN_q and m is determined by balancing two sides of following equation:

$$Ap_u = \Delta\sigma_{1max} D(mN_q) \qquad (2.67)$$

Then: $$p = \Delta\sigma_1 (mN_q) D \qquad (2.68)$$

where:

- $\Delta\sigma_{1max}$ peak deviatoric stress of stress-strain curve
- m is a modifier to N_q,

A new set of p-y curves developed from stress-strain responses at confining pressure of 25, 50 and 75 kPa, which correspond to certain numbers of depth depending on soil unit weight. Since soil tests only can be conducted in limited number, generalized parameters should be determined, for example the set of modulus number K, modulus exponent n, ϕ_1, $\Delta\phi$, R_f obtained for hyperbolic model, to construct stress-strain curve at other confining pressure and thus p-y curves at other depths.

The stress-strain curves at aforementioned confinement is reconstructed by hyperbolic model parameters shown in Table 2.20 and testing peak strain (Table 2.23). ϕ_1 is used for all soil at same density as previously employed for generating API p-y curves.

Coefficient M_s is illustrated in Table 2.24. The converted p-y curves are plotted along with API ones in Figure 2.31 to Figure 2.34. It is noteworthy that the increasing depths in curves correspond to $\gamma'z$ =25 kPa, 50 kPa and 75 kPa, respectively. Value of modifier, m, is also indicated for each curve.

It can be seen that two sets of p-y curves have good agreement at small depth ($\gamma'z$ =25 kPa). However, gap between the two rises with increasing depths, especially at small displacement. Further study needs to be done to determine scaling factor for this segment of the p-y curves.

Modifier m is calculated for each curve and its values it presented in Table 2.25 and Figure 2.35. It is shown that m is inversely proportional with D_R and likely linearly proportional with depth. Effects of D_R is considered by multiplying m by $\tan^2\phi_1$, where ϕ_1 is friction angle at confinement of 100 kPa, and values of $m(\tan^2\phi_1)$ at certain depth is much more convergent (Figure 2.36). An average line for $m(\tan^2\phi_1)$ is plotted and bases on that, m to depth relation can be written as:

$$m(\tan^2\phi_1) = 0.042z + 0.02 \quad (2.69)$$

Then: $$N_s = \frac{0.042z + 0.02}{\tan^2\phi_1} N_q \quad (2.70)$$

Table 2.23. Peak strain [%] of tested samples resulted from Hyperbolic model

D_R (%)	σ'_3 / P_a		
	0.25	**0.5**	**0.75**
20	4.5	5.4	6.6
40	2.8	3.4	3.8
53	2.8	3.00	3.4
70	2.5	2.6	2.7

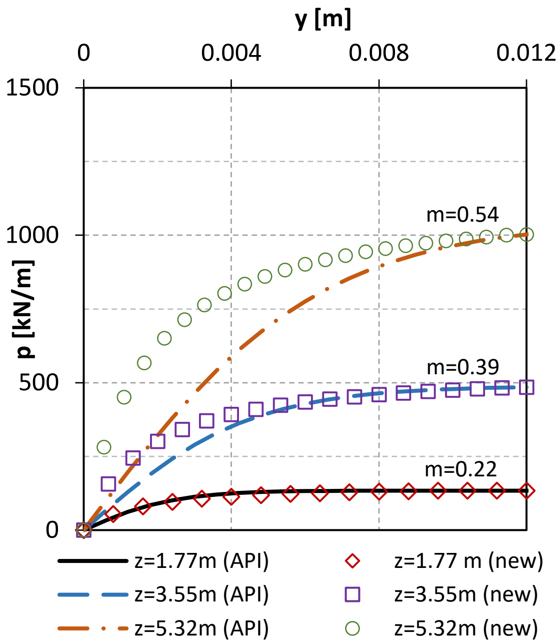

Figure 2.31. Proposed p-y curves converted from stress-strain response for D_R=20%

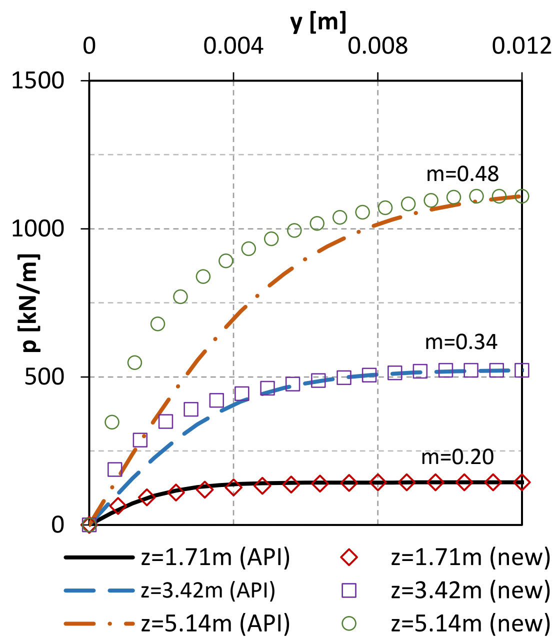

Figure 2.32. Proposed p-y curves converted from stress-strain response for D_R=40%

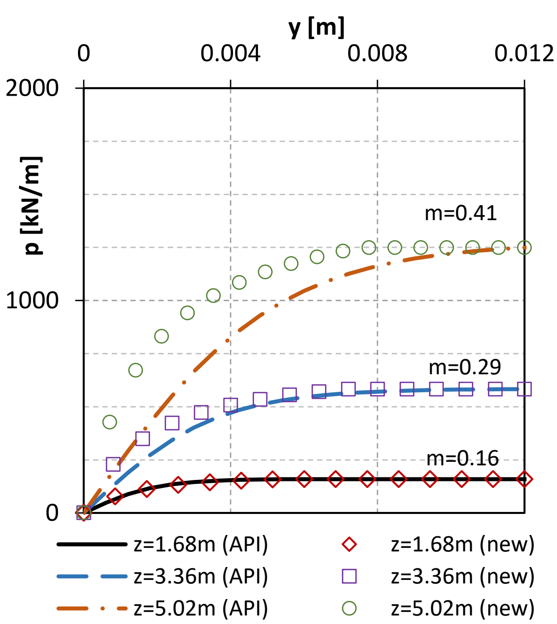

Figure 2.33. Proposed p-y curves converted from stress-strain response for D_R=53%

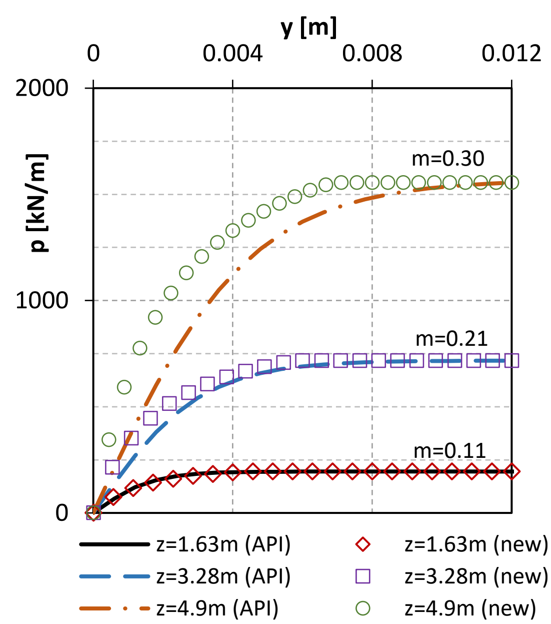

Figure 2.34. Proposed p-y curves converted from stress-strain response for D_R=70%

Table 2.24. Coefficient M_s

D_R (%)	σ'_3 / P_a		
	0.25	**0.5**	**0.75**
20	0.012	0.014	0.018
40	0.007	0.009	0.010
53	0.007	0.008	0.009
70	0.007	0.007	0.007

Table 2.25. Modifier m for N_q

D_R (%)	$\gamma' z$ (kPa)		
	25	**50**	**75**
20	0.22	0.39	0.54
40	0.20	0.34	0.48
53	0.16	0.19	0.41
70	0.11	0.21	0.30

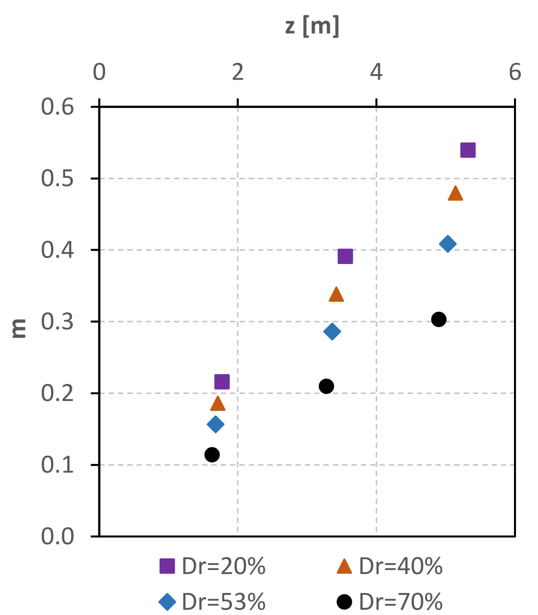

Figure 2.35. Modifier m in relation with depth and relative density

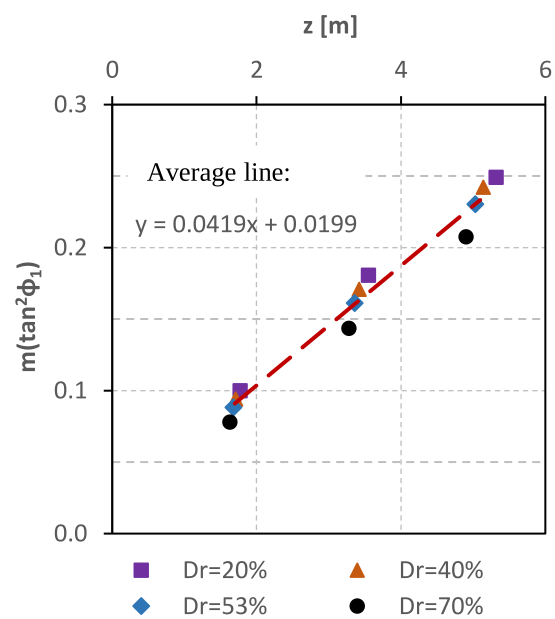

Figure 2.36. m($\tan^2\phi_1$) in relation with depth and relative density

2.9 Conclusions and recommendations

Soil classification and sixteen drained axial compression triaxial tests were performed to determined soil properties for laterally loaded pile analyses. The focus was on valuation of soil shear strength and modulus parameters across relative density between 20% and 70%. Several factors affecting triaxial testing results were assessed and corrections for them were applied in final outcomes. The conclusions on findings are:

- Cross-sectional area correction caused obvious change in stress-strain response and is the most important correction among all. Coefficient α=1.33 was chosen for tested samples based on observation on post-experimental failed samples. This correction is highly recommended to be considered in processing testing date. For better selection of α, sample radial deformation should be monitored closely during shear.

- Latex membrane with nominal diameter of 7.1cm and thickness of 0.03cm had generally little effects, including membrane resistance and membrane compliance, on stress-strain response. Membrane axial resistance had insignificant contribution peak stress difference (up to 3%) but it increased with increasing axial strain and could make up of 6.5% of stress difference at strain of 20%. Therefore, it should be considered with testing data at post-peak axial strain.

- Stress-strain responses for sixteen samples at relative densities of 20%, 40%, 53% and 70% were developed and a set of shear strength and modulus parameters was determined and could be implemented in numerical simulation. Relation between modulus number and relative density could be expressed as: $K = 10.36D_R + 90$

- P-y curves by API recommendations were generated for selected depths. They were employed to developed a new set of p-y curves from triaxial stress-strain curves. A procedure to convert stress-strain curves to p-y curves was presented, in which two converting coefficients was associated with stress-strain curve parameters and depth as follows:

$$M_s = \frac{80\varepsilon_p}{3}$$

$$N_s = \frac{0.042z + 0.02}{\tan^2 \phi_1} N_q$$

- The new API-similar p-y curves are appropriate for depths that has ultimate soil reaction computed by $p_u = (C_1 z + C_2 d)\gamma' z$, where C_1 and C_2 are defined by equations 2.54 and 2.55, respectively. They show good agreement with API ones at low depths (γz=25 kPa); however, for deeper ones, there are significant gap at low displacement. These are also more suitable for loose to medium sand as they are developed based on up-to-peak segment of stress strain curves. For dense sand, the post-peak response needs to be addressed and combined in p-y curves. Analytical development and calibration on this set of p-y curve is necessary, and further studies on its limitations are recommended.

3. PAPER II: P-Y CURVES FOR SAND OBTAINED FROM THREE-DIMENSIONAL NUMERICAL ANALYSIS OF LATERALLY LOADED PILE

3.1 Introduction

Performance of laterally loaded pile has been a prominent case of the field of soil-structure interaction. Lateral load transmitted to pile results from wind, sea wave, seismic activities, or lateral earth pressure of sloping ground or soil excavation. As the pile deflects, stress-strain behavior of soil elements adjacent to pile is very complicated and different from place to place. For simplicity, soil reaction is represented by an equivalent resultant of soil stresses on pile perimeter. The relation between soil reaction and pile deflection at given depth is called p-y curve. P-y curves has been mainly determined by semi-empirical method of back analysis of pile load test results, and many researches have offered the p-y relationship for analysis and design (Matlock, 1970, Reese, *et al.*, 1974, Georgiadis, 1983, Briaud, *et al.*, 1984, Yan and Byrne, 1992, Bouafia, 2007)

Beam on nonlinear Winkler foundation (BNWF) has been the main approach to develop and calibrate p-y curves. P-y relationships are used to characterize discrete springs in the numerical model. The model could be at high level of complexity with supplementary elements, for example gap member describing soil-pile attachment, detachment and re-attachment in cyclic and dynamic loading, or equivalent spring stiffness and dashpot describing soil damping in dynamic case (El Naggar and Novak, 1995, Boulanger, *et al.*, 1999, Budek, *et al.*, 2000, Allotey and El Naggar, 2008). These improved features help verifying p-y curves for cyclic and dynamic loading by examining cyclic and dynamic load tests on piles. Three-dimensional numerical analysis offers an alternative way to investigate laterally loaded pile and construct p-y curves (Brown and Shie, 1990, Yang and Jeremić, 2002, Fan and Long, 2005, Kim and Jeong, 2011, Zhang and Ahmari, 2013). Soil stress-strain behavior is described by constitutive model using its own properties, and soil reaction could be determined by finding resultant, in loading direction, of stresses at points in soil clusters adjacent to pile surface. Getting along with a movement toward performance-based design, deformation analysis by finite element method plays more significant role in geotechnical engineering.

A large-scale testing program on reinforced concrete filled steel pipe piles is performed in soil pit at the Constructed Lab Facilities of North Carolina State University to investigate formation of in ground plastic hinge and interaction between soil and pile in framework of performance-based design. Rigid boundary and surcharge definitely influences soil-pile system performance and p-y curves for soil, particularly on three aspects: (1) vertical stress in soil, (2) lateral modulus of subgrade reaction and (3) ultimate soil resistance. Therefore, implementation of API p-y curves for pile analysis with consideration of combining effect of all above factors is very challenging, particularly in selecting modulus of subgrade reaction and ultimate resistance. This study uses Plaxis 3D Foundation (Brinkgreve and Broere, 2006) to simulate two real pile tests in soil pit and validate model parameters by matching testing results. Soft Soil Hardening model, which bases on hyperbolic stress-strain relation and stress-dependent modulus by Duncan and Chang (1970), is employed in the analyses. The simulation is focused on range of loading magnitude in which pile still behaves elastically. P-y curves for testing conditions then are generated, and subsequently the model is extended to determine p-y relationships for free-field conditions. Effects of cyclic load, boundary conditions and soil relative density are examined. The relation between calibrated soil modulus and that resulted from triaxial tests is also an aim of the research as a recommendation for future 3D numerical analyses.

Derived p-y curves for testing conditions could be deployed as a portion of backbone loading p-y relation in Beam on nonlinear Winkler foundation model with advanced models for pile to investigate soil-pile interaction in both linear and nonlinear regions of pile behavior in experiments.

3.2 Background on numerical analysis of laterally loaded pile

3.2.1 Analyzing models

For analysis of pile subjected to lateral load by Beam on nonlinear Winkler foundation (BNWF) approach or 3D simulation, following models are used to describe pile and soil behaviors:

- Elastic pile – elastic soil
- Plastic pile – elastic soil
- Elastic pile – nonlinear soil
- Nonlinear pile – nonlinear soil

Last two models are currently dominant in current studies on laterally loaded pile. BNWF model now covers third and fourth models for cyclic and dynamic analysis with complexity in defining spring stiffness (El Naggar and Novak, 1995, Boulanger, *et al.*, 1999, Naggar and Bentley, 2000, Gerolymos and Gazetas, 2005, Taciroglu, *et al.*, 2006).

Pile flexural behavior might be considered with effect of confinement on concrete compressive strength (Budek, *et al.*, 2000, Kerop D. Janoyan, *et al.*, 2006, Rajaparthy, *et al.*, 2008), and even can be described in fiber model (Hutchinson, *et al.*, 2004, Taciroglu, *et al.*, 2006, Allotey and El Naggar, 2008, Limkatanyu, *et al.*, 2009).

The open-source platform OpenSees (http://opensees.berkeley.edu) offers a wide range of linear and nonlinear structural elements, including fiber, and soil models for 3D numerical analysis. OpenSeesPL (Lu, *et al.*, 2011) is a user interface for execution of push-over and seismic pile-ground simulation, in which available soil constitutive model for sand is Drucker-Prager model. Commercial 3D finite element packages, e.g. Plaxis (Brinkgreve and Broere, 2006), offers better soil models but at the same time likely don't include progressive models for pile. However, pile nonlinearity could be described by choosing appropriate section secant stiffness at the level of imposing load.

3.2.2 Constitutive model for soils

There are a number of existing soil constitutive models for finite element analysis of geotechnical engineering problems. It is important to understand their applicability and limitations of the models and selecting model parameters. Brinkgreve (2005) summarized existing models and following are some of them, which are appropriate and have been used for numerical investigation of soil-structure interaction.

- The Mohr-Coulomb model

This is a elasto-perfectly plastic model and is considered as first order model. It works well in strength analysis with hexagon failure contour that includes consideration of effect of intermediate stress. However, it has limited ability in accurately estimating deformation response prior to failure. Estimation of deformation for unloading cases, excavation for example, would be exaggerated as the model uses the same modulus value for loading and unloading. Another limitation is that it is not able to describe softening behavior of soil after reaching peak strength. Kim and Jeong (2011) and Kim, *et al.* (2014) employed Plaxis 3D Foundation simulation using Mohr-Coulomb model to analyze large diameter steel pipe piles and drilled shafts.

- The Drucker-Prager Model (Drucker and Prager, 1952)

Drucker-Prager model is a simplification of Mohr-Coulomb model with hexagon failure contour being replaced by a cone-shaped one. Therefore, failure analysis for problem in unconventional stress paths or in multiple stress paths, like in laterally loaded pile, might become erroneous. This model has been used in numbers of earlier studies on this area by Brown and Shie (1990), Yang and Jeremić (2002, 2005) , Karthigeyan, *et al.* (2007) and Lu, *et al.* (2010)

- Hyperbolic Model and Hardening Soil Model

Hyperbolic model (Duncan and Chang, 1970) is considered as improved first order model, while Soft Soil Hardening (Brinkgreve and Vermeer, 1997) is true second order for soils (Brinkgreve, 2005). They both have same failure criteria as Mohr-Coulomb and include improvements in describing soil stiffness. They both use a power rule for stress-dependent modulus and nonlinear stress-strain behavior of soil up to failure. Hardening Soil model overcomes Hyperbolic model limitation in modelling post-peak behavior by using dilatancy angle for soil. These model should be employed for better accuracy on displacement estimation for geotechnical engineering problems. Zhang and Ahmari (2013) implemented Hyperbolic model for examining laterally loaded pile on clay. This study will be using Hardening Soil Model in Plaxis 3D Foundation dealing with the problem.

3.2.3 Factors affecting p-y curves obtained from 3D analysis

Fan and Long (2005) performed 3D simulation of single pile test in sand at Mustang Island and verify parameters of Desai model (Desai, *et al.*, 1991) used in the analysis. It is noteworthy that this testing data was used for developing API family p-y curves by Reese, *et al.* (1974), and lateral load was applied at 0.3m above ground surface. P-y curves for soil then was generated from analysis result. Parametric study was conducted and following are summary on effects of studied factors:

- Pile section flexural rigidity (EI) and diameter (D):

Pile section EI was concluded to have insignificant effects on p-y curves when pile diameter remains unchanged. However, increase in D (while EI is constant) leads to increase in ultimate soil reaction, and thus larger soil reaction in p-y curves. A linear relationship between p_u and D was not confirmed.

- Horizontal earth pressure coefficient (K):

Soil reaction is reported to increase considerably in p-y curves with increasing K, which means soil stress history or overconsolidation ratio (OCR) and pile installation method would play an important role in soil-pile interaction.

- Angle of dilatancy:

The study concluded that dilatancy angle is proportional to ultimate soil reaction thus influences p-y relationship.

- Soil-pile interface properties:

Kim and Jeong (2011) performed 3D numerical analyses of large diameter steel pile (D=1.0m) and pile drilled shaft (D=2.4m) in Plaxis 3D Foundation using Mohr-Coulomb model for soil. The parametric study on interface properties, which is represented by interface strength reduction factor R_{inter}, showed no significant influence of this parameter on pile behavior.

- Cyclic loading:

There have been no previous 3D numerical analysis that reported impact of cyclic loading on obtained p-y curves. In general, p-y curve is influenced by number of loading cycles, level of load and soil types. Reese, *et al.* (1975) reported very significant reduction due to cyclic load in soil response in p-y curves obtained from testing results on pile in stiff clay. However, API equations for p-y relationship for sand indicate cyclic load has almost no effect along pile length, except within the depth of less than three times pile diameter from ground surface. The difference likely results from effects of soil gapping (for clay) and soil cave-in (for sand). Allotey and El Naggar (2008) suggested the latter could be beneficial and improve pile performance.

3.2.4 Stress state of surrounding soil due to lateral movement of pile

Fan and Long (2005) reported a complicated stress pattern in soil clusters adjacent to pile. Different stress paths were found in different zones (see Figure 3.1). Soil elements on pile section perimeter experience four different stress paths namely lateral compression (LC), axial compression (AC), direct simple shear (DSS) and axial extension (AE). Therefore, the soil modelling could be extremely complicated involving sizing the zones of dissimilar stress-strain behaviors, assigning appropriate model parameters to the zones and post-analyzing check for suitability of zoning. In addition, it needs to be performed separately for different depths. For practical purpose, one zone with equivalent soil parameters should be modelled, and shear strength and modulus parameters of the zone also should be associated with stress-strain curves by a conventional stress path as AC. This study applies second approach.

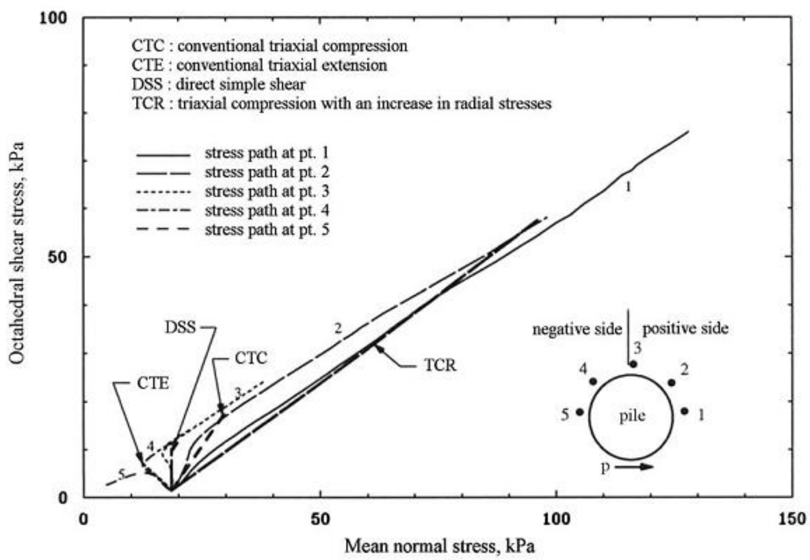

Figure 3.1. Stress paths at soil elements around pile section (Fan and Long, 2005)

3.2.5 Soil reaction for p-y curves from numerical analysis results

Fan and Long (2005) introduced a procedure to determine soil reaction from stresses at points closest to pile perimeter as follows:

- Determine closest Gauss points to pile perimeter and their coordinates to pile section center (x_g, z_g). They are on black dashed line in Figure 3.2
- Compute traction vector T_x representing x-component stress at every stress point:

$$T_x = \sigma'_{xx} n_x + \sigma'_{xy} n_y + \sigma'_{xz} n_z \quad (3.1)$$

where:

$$n_x = \cos\theta_x = \frac{x_g}{\sqrt{x_g^2 + z_g^2}} \quad (3.2)$$

$$n_z = \cos\theta_z = \frac{z_g}{\sqrt{x_g^2 + z_g^2}} \quad (3.3)$$

$$n_y = 0 \quad (3.4)$$

- Compute total soil reaction by stress points:

$$p_x = \int T_x dL \quad (3.5)$$

where L is the circumference of the closest Gauss points

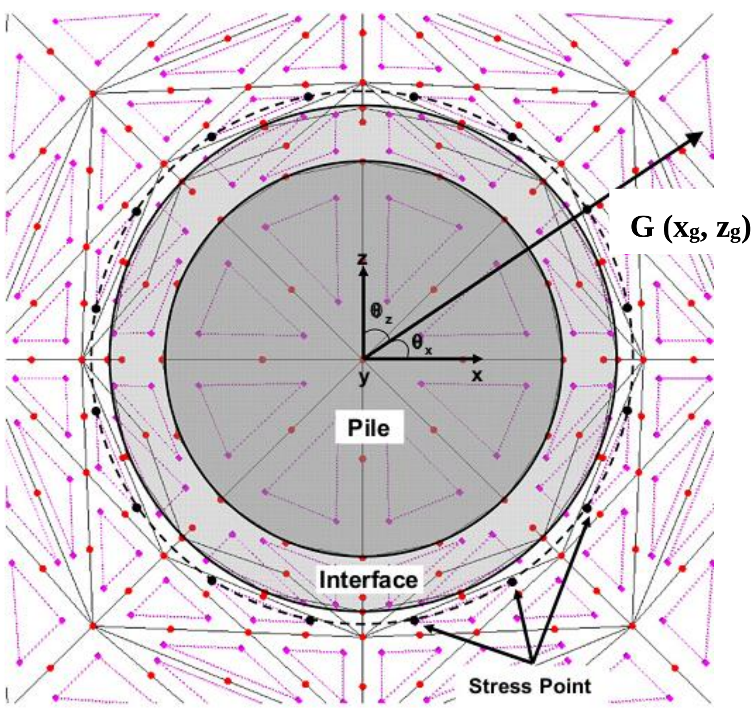

Figure 3.2. Location of stress points for computing soil reaction on pile (Kim and Jeong, 2011)

3.3 Pile testing program

3.3.1 Pile testing program

Eight reinforced-concrete-filled-steel-pipe piles (RCFSPP) were tested in soil pit, which is 3.05m in diameter and 6.10m in depth, at the Constructed Lab Facilities of North Carolina State University. Pit was filled with gravel at bottom and about 4.5m of sand above. Before being installed each pile was instrumented with strain gages at spacing of 0.6m in projected underground portion. Strain gages were mounted on front and back sides of pile, in direction of loading. Inclinometers were setup at pile center at spacing of 0.6m throughout from top to bottom of pile.

Subsequently, pile was installed into soil pit after the soil was liquefied by upward water flow. Pile was hang on crane for few days as water was draining out and soil was settling. Two semi-circular concrete plates were placed on sides of pile leaving a lane in the middle of the pit for pile to be displaced. These plates and another one at the bottom of the pit created a sandwich-like soil-plates system. Top and bottom plates were connected by six post-tension bars, which allows applying surcharge on soil by hydraulic jacks. Another set of LED markers are mounted on pile portion above ground surface and their locations will be tracked to independently observe pile deflection. Some pressure cells were mounted on pit wall in order to investigate boundary effect. All testing data was recorded digitally and very frequently during testing.

Piles were tested in free-head condition. Lateral force was applied on top of pile by a hydraulic actuator that has capacity of 445 kN and stroke of 1.8 m (see Figure 3.3). All tested were displacement-controlled and load history was designed in two phases. Phase I was to evaluate elastic performance of piles, so loading pattern is single cycle with increasing of displacement magnitude until first yield occurred. Phase II was to investigate nonlinear response so piles were tested with standard three-cycle set at each level of ductility until pile fracture. Target displacements were initially determined by a 2D finite element software using p-y curves in OpenSees platform.

Figure 3.3. Pile test S6 setup (courtesy of Diego Aguirre)

Piles were casted pair with same configuration, one was tested with presence of top plates and the other one had additional surcharge of 46 kPa. Surcharge was kept constant during testing by adjusting total pressure of hydraulic jacks. Different pairs of piles had different pile diameter-to-pipe thickness, D/t, ratios. This study will analyze results of pile tests S5 and S6 in elastic range of pile behavior.

3.3.2 Pile configuration and section moment-curvature response

3.3.2.1 Pile description

Description of piles in pile tests S5 and S6 is summarized in Table 3.1, in which both piles shared cross section details (Figure 3.4) and materials properties (Table 3.2)

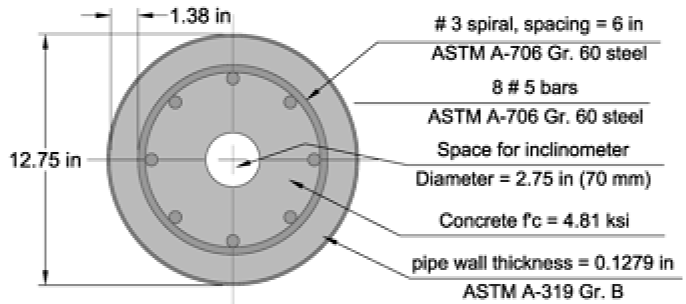

Figure 3.4. Pile cross section (courtesy of Diego Aguirre)

Table 3.1. Details on piles in pile tests S5 and S6 for analyses

Pile test	L (m)	D (m)	t (mm)	D/t	Surcharge	Cantilever length (m)
S5	5.82	0.324	3.3	95	Plates = 5kPa	1.73
S6	5.82	0.324	3.3	95	Plates + 45.8 kPa = 50.8 kPa	1.79

Table 3.2. Pile materials properties

Concrete	Steel pipe	Longitudinal steel	Transverse steel
f'_c = 33.2 MPa E_c=28,810 MPa	f_y = 374.9 MPa f_{ult}= 521.9 MPa	f_y = 488.0 MPa f_{ult}= 687.4 MPa	f_y = 445.70 MPa

3.3.2.2 Pile flexural rigidity

Bases on pile section configuration, section gross stiffness and moment-curvature response are computed. Moment-curvature relationship calculation implements Mander' model for confined concrete (Mander, *et al.*, 1988) and King's model for steel (King, *et al.*, 1986). Section limit states (Priestley, *et al.*, 2007) are used for determination of M-Φ relation parameters and nominal flexural strength. Moment-curvature response and its values at several limit states are presented in Figure 3.5and Table 3.3. It can be seen that up to first yield, moment-curvature relationship is almost linear. The cracked section flexural rigidity can be computed as $(EI)_{cr} = M_y^{'} / \Phi_y^{'}$. $(EI)_{cr}$ - to - $(EI)_{gr}$ ratio is 0.57 (Table 3.4); $(EI)_{cr}$ is used for pile in numerical model.

Table 3.3. Section limit states (Priestley, *et al.*, 2007)

Limit state	Criteria	Obtained values
First yield	$\varepsilon_s = \varepsilon_y$ or ε_c=0.002, whichever occurs first	$\Phi_y^{'} = 0.00963\ 1/m$ $M_y^{'} = 131.22\ kNm$
Service	ε_s= 0.015 or ε_c=0.004, whichever occurs first	$\Phi_s = 0.03776\ 1/m$ $M_{DC} = 218.55\ kNm$
Damage control	ε_s= 0.004 or ε_c=0.02, whichever occurs first	$\Phi_{DC} = 0.17269\ 1/m$ $M_{DC} = 269.59\ kNm$
Ultimate	ε_s= 0.009 or ε_c=0.025, whichever occurs first	$\Phi_u = 0.52293\ 1/m$ $M_u = 301.53\ kNm$

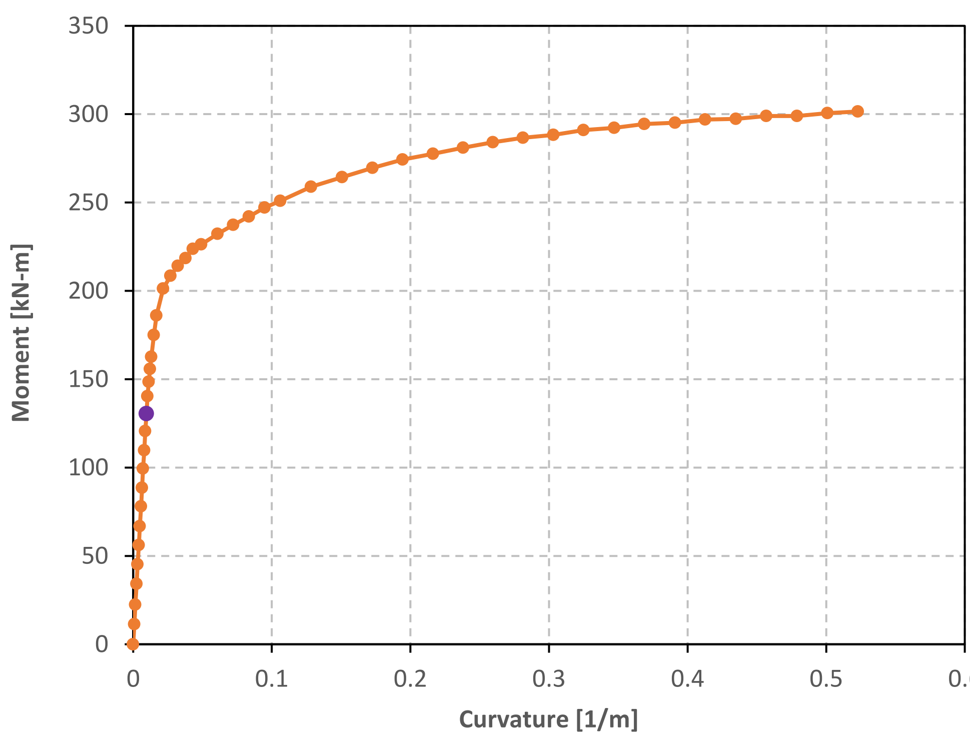

Figure 3.5. Section moment-curvature response (courtesy of Diego Aguirre)

Table 3.4. Gross and crack flexural rigidity of section

$(EI)_{gr}$ (kNm^2)	$(EI)_{cr}$ (kNm^2)	$(EI)_{cr}/(EI)_{gr}$
23,848	13,626	0.57

3.3.3 Soil properties

Soil classification tests were performed for sand layer to determined particles-size distribution, e_{max} and e_{min}, and specific gravity (Table 3.5). Sixteen triaxial tests with axial compression stress path in drained condition were conducted on reconstituted specimens at four relative densities of 20%, 40%, 53% and 70% and four confining pressures of 25 kPa, 50 kPa, 100 kPa and 200 kPa. Stress-strain curves then were transformed into hyperbolic form to determined modulus number K and modulus exponent n. Shear strength parameters of friction angle and failure ratio R_f were derived from testing results. A set of parameters for Hyperbolic model was established as a basis for selecting model parameters in numerical simulation (Table 3.6). Relation between modulus number and relative density is expressed as:

$$K = 10.36D_R + 90 \qquad (3.6)$$

Soil samples were taken from the pit prior every pile test to determine water content, unit weight and in-situ void ratio. To minimize sample disturbance, soil was collected carefully with Shelby tube. However, due to limitation in working space as pile was already installed, as well as safety concerns, samples only could be collected up to the depth of 0.6m. Moisture content testing procedure is covered by ASTM D2216-10. Results for pile tests S5 and S6 are presented in Table 3.7

Table 3.5. Soil type, specific gravity, and index void ratios

Soil type	e_{max}	e_{min}	G_s
SP	0.91	0.61	2.66

Table 3.6. Summary of strength and modulus parameters

D_R (%)	γ_d (kN/m3)	K	n	ϕ_1 (deg)	$\Delta\phi$	R_f
20	14.1	286	0.52	34.2	3.28	0.86
40	14.6	516	0.52	35.4	5.33	0.83
53	14.9	638	0.52	36.9	5.80	0.79
70	15.3	832	0.52	39.6	6.97	0.74

Table 3.7. Moisture content, unit weight and void ratio

Pile test	Sample	Depth (m)	w (%)	γ (kN/m^3)	e	D_R (%)
S5	#5.1	0.15	2.34	14.2	0.88	10
S6	#6.1	0.15	2.77	14.2	0.89	6.7

3.3.4 Testing results for pile test S5 and S6

Prescribed pile head displacement and load histories for pile tests S5 and S6 and pile displacement profiles up to pile yielding are shown in Appendix B

3.3.5 Gapping and soil cave-in

Once pile was displaced, a gap between pile back surface and soil occurred and increased with increasing load. Due to soil arching and, to some extent, soil unsaturation, soil did not cave in the void. However, as the void enlarged with increasing magnitude of cyclic load, mainly in direction of loading, soil started falling in from sides and then from back and front of pile (see Figure 3.6 and Figure 3.7). These phenomena are extremely hard to simulate in numerical analysis; therefore, their influence on pile-soil system performance was categorized as one of effects of cyclic loading. This impact was assessed by the change in model parameters of analyses for first value of pseudo-static load and higher ones at subsequent cycles.

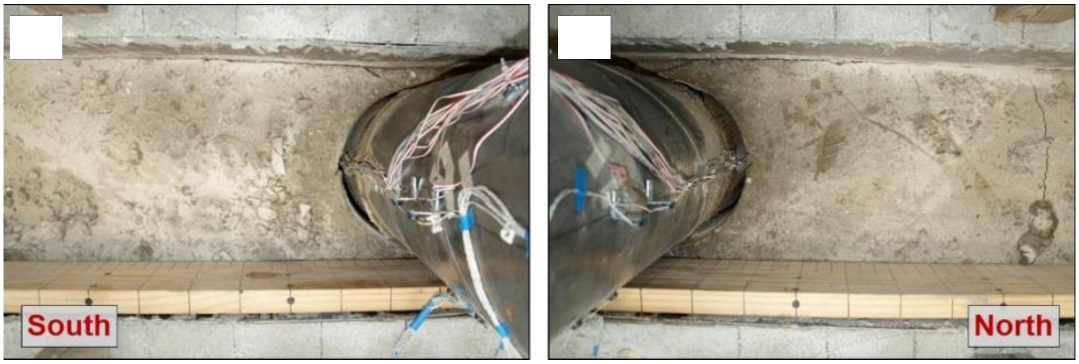

Figure 3.6. Gapping at front and back of pile in first phase of loading history (courtesy of Diego Aguirre)

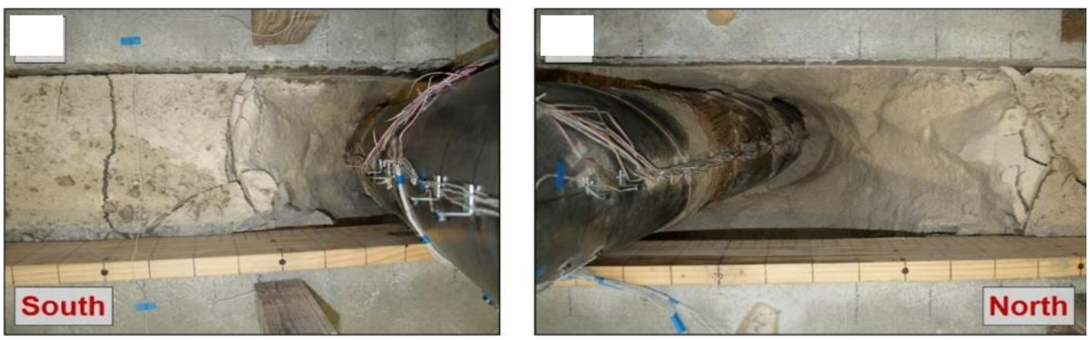

Figure 3.7. Gapping and soil cave-in in second phase of loading history (courtesy of Diego Aguirre)

3.4 3D simulation

3.4.1 Model configuration

3.4.1.1 Boundary condition

Soil in soil pit is described as a 4.5m homogenous sand layer on top of 0.3m of gravel. Pit circular section is described as a regular polygon with 18 edges and internal angles of 20°. Fixities are automatically applied by program at boundary that hinder soil moving vertically at bottom of soil layer and horizontally on sides. Concrete plates on top of soil are described by vertical distributed load. Interface interaction between soil and pit wall, and between soil and plates surface are not considered in model.

3.4.1.2 Hardening soil model parameters and soil-pile interface

Gravel layer is described in Mohr-Coulomb model with modulus of 120,000 kPa and friction angle of 45° (Kulhawy and Mayne, 1990) to avoid significant settlement and failure of this layer. Sand layer is described in Hardening soil model. Parameters required for hardening soil model are presented in Table 3.8. γ, n, ϕ, R_f parameters are taken directly from soil properties resulted from triaxial test (Table 3.6 and Table 3.7). Since cyclic load is simulated as equivalent static load, unloading modulus is not calibrated and is set as default value by program. The values of parameters depend on expected soil relative density. The calibration process comes down to only two parameters E_{50}^{ref} and E_{oed}^{ref} . Since, interface property was concluded to have insignificant effect on soil-pile interaction (Kim and Jeong, 2011), R_{inter} is chosen as 0.7

3.4.1.3 Meshing

It is understood that meshing is influential on outcomes and outcomes would converge when meshing is refined to a certain degree. However, fine meshing required more resources to run the program; therefore, medium size mesh is selected for the model.

Table 3.8. Model parameters (Brinkgreve and Broere, 2006)

Parameter	Description	Unit	Value
γ	Soil unit weight	kN/m^3	Table 3.6
ϕ	Friction angle	deg	Table 3.7
c	Cohesion	kPa	0.01
R_f	Failure ratio	-	Table 3.7
m	Modulus exponent	-	Table 3.7
E_{ur}^{ref}	Unload-reload modulus at reference confining pressure of 100 kPa	kN/m^2	$3E_{50}^{ref}$
E_{50}^{ref}	$E_{50}^{ref} = \frac{(2-R_f)}{2} E_i^{ref}$ (3.7) secant modulus at 50% failure deviatoric stress, corresponding to reference confining pressure	kN/m^2	To be calibrated
E_{oed}^{ref}	Tangent modulus at reference axial stress of 100 kPa in oedometer test	kN/m^2	To be calibrated
R_{inter}	Interface strength reduction factor	-	0.7

3.4.2 Pile properties

Pile element is described to have flexural stiffness similar to $(EI)_{cr}$. Since the software is not allowed to prescribe directly pile stiffness, a composite section is defined for pile. The section comprises of elastic shell elements enclosing an elastic core. This configuration helps to avoid pile section deformation and distortion. Pile section has diameter of actual pile and shell element has thickness of actual steel casing. Interface between two materials is set as rigid (R_{inter} =1). Circular section is described by 12-edge regular polygon.

Pile stiffness if calibrated by simulating a cantilever beam subjected to a lateral load at level of L=2m from fixity. Values of lateral are chosen to cause a maximum moment that is not greater than first yield moment ($M_y^{'} = 131.22$ kNm). Moduli of the shell and filling material initially are set as values of actual steel pipe and concrete, respectively. Then they are modified by same modifier until displacement profile of pile matches closely with that of a beam having same boundary, loading conditions and flexural rigidity of $(EI)_{cr}$. Calibration is performed at three values of load P=65.6 kPa, P=32.8 kPa and P=16.4 kPa, corresponding to M= $M_y^{'}$, $0.5M_y^{'}$ and $0.25M_y^{'}$, respectively. Displacement of cantilever beam is computed as: $\Delta_x = \dfrac{P}{6(EI)_{cr}}(2L^3 - 3L^2 + x^3)$, where x is the distance from point of interest to free end. Obtained moduli for shell and enclosed material are described in Table 3.9. The model and displacement profiles are presented in Figure 3.8, and details on displacement profiles of beam and pile are presented in Appendix C.

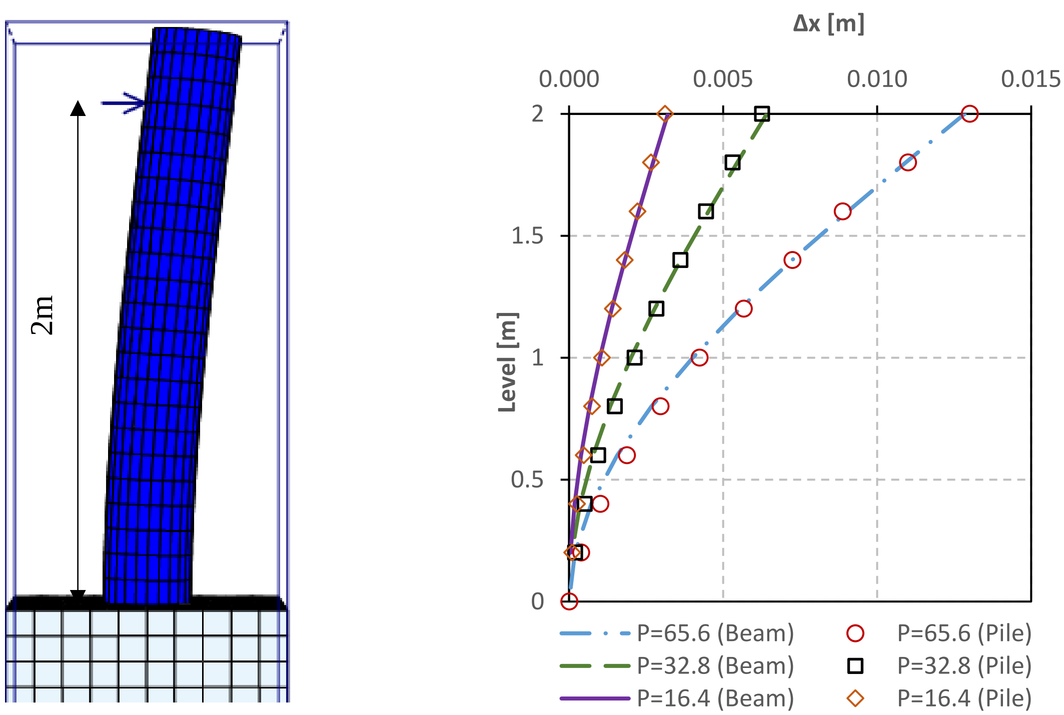

Figure 3.8. Pile calibration model (left) and displacement profiles (right)

Table 3.9. Modulus for simulated pile materials

Shell		Core	
E_{sh} (MPa)	E_{sh}/E_s	E_{core} (MPa)	E_{core}/E_c
146,000	0.73	21,030	0.73

3.5 Plaxis 3D model calibration and p-y curves for testing conditions

3.5.1 Calibration procedure

3.5.1.1 Staged construction analysis

The simulation follows the consequence of construction works by using staged construction analysis feature of Plaxis. Analysis of a stage inherits model conditions from the precedent and passes on the updated post-analyzing conditions to the descendent. Stages of analysis are presented in Table 3.10. Typical model and displacement pattern in system are described in Figure 3.9.

Table 3.10. Analyzing stages

Stage	Description
Initial	K_0- consolidation procedure under soil and pile selfweight
Phase 1	Applying surcharge
Phase 2	Applying lateral load P_1
Phase 3	Applying lateral load $P_2 > P_1$
Phase 4	Applying lateral load $P_3 > P_2$

3.5.1.2 Calibration procedure

Model parameters will be calibrated based on displacement profiles obtained from experiments. Three pushing portions of first three loading cycles will be simulated while pulling halves are not included. In other words, cyclic loading is replaced by equivalent pseudo-static analysis that yields identical displacement profile. Effects of cyclic load will be detected if there is any difference in model parameters for static loading values. Magnitudes of load applying on pile are presented in Table 3.11

Table 3.11. Lateral load magnitudes for analyses

Pile test	Surcharge	P_1 (kN)	P_2 (kN)	P_3 (kN)
S5	5 kPa	15.9	25	33
S6	50.8 kPa	17.5	27.1	41

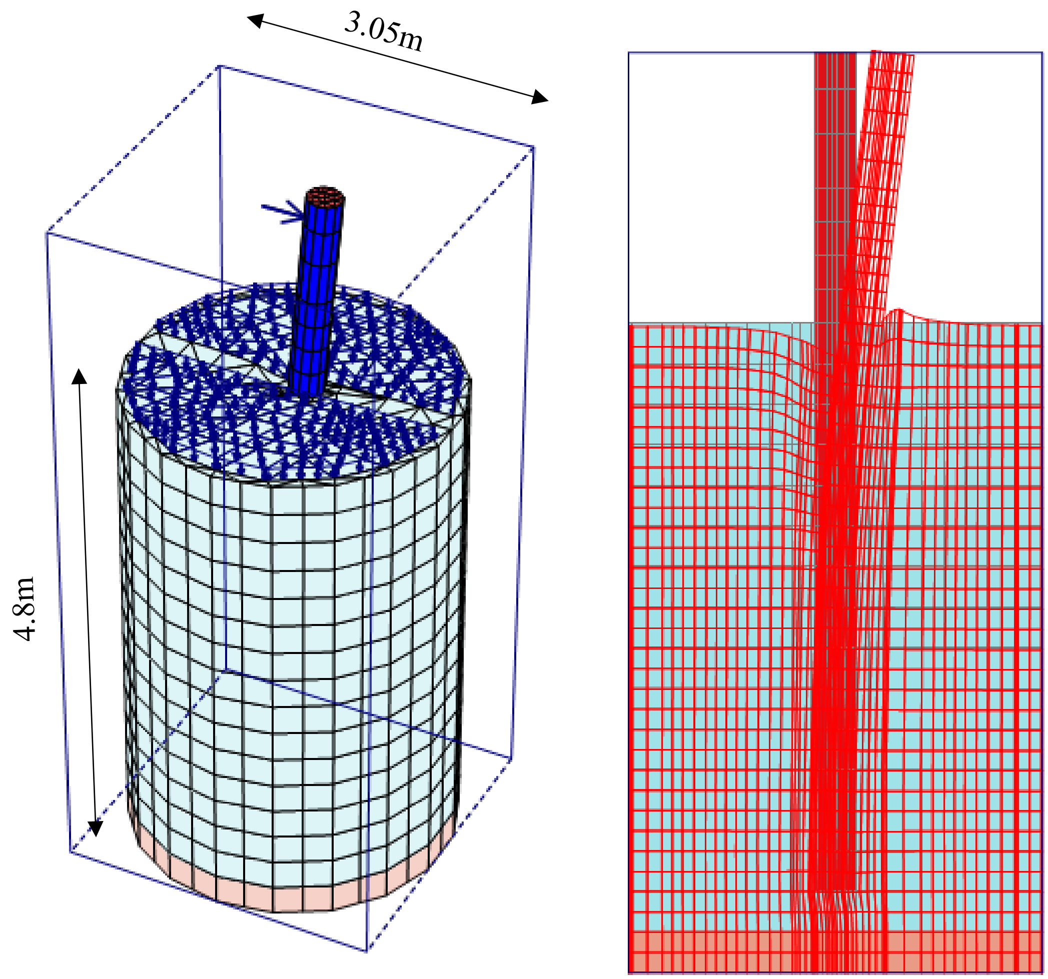

Figure 3.9. Typical 3D model for analysis (left) and horizontal displacement pattern in pile and soil (right)

Validation procedure and parametric study are as follows:

- Calibration for testing condition 1 (surcharge of 5 kPa): find model parameters for P_1, then increases load to P_2 and P_3:
    - If displacement profiles for P_2 and P_3 agree with testing results, cyclic loading has insignificant effect
    - Otherwise, modify parameters in a new model, apply the level of load that need to reanalyze. Match testing results and assess effect of cyclic loading on soil-pile interaction,
    - Determine p-y curves for testing condition 1
- Calibration for testing condition 2 (surcharge of 50 kPa): Since soil for pile S6 was slightly looser than that of pile S5, it properties are calibrated separately following aforementioned procedure. Surcharge of 50 kPa sustained during the test so it is unchanged in the model. The surcharge changes vertical effective stress and thus mean stress in soil, resulting in different parameters for p-y curves. P-y curves for testing condition 2 is determined and will be compare with those from condition 1 to examine the effect of the surcharge.
- Extend boundary to larger distance that assures free-field condition:
    - Run analyses with calibrated parameters for S5 for various loading values, including P_1, P_2, P_3. Compare obtained results with tested ones, and determine p-y curves for static load in free-field condition. Subsequently, analyze boundary effect in pile test results.

- Alternate soil properties for higher relative density and rerun analyses.

Determine effect of denser soil in soil-pile interaction and p-y curves.

3.5.2 Parameters verification for pile S5

3.5.2.1 3D analysis displacement profiles versus experimental data

With values of E_{50}^{ref} and E_{oed}^{ref} presented in Table 3.12, simulation results agree well with testing data at P_1, and P_2 and P_3 (see Figure 3.10). However, discrepancy is increasing at depths larger than 1.8m. Since it is one set of parameters, it can be concluded that cyclic loading has very little effect of soil-pile interaction in first three cycles of loading. Coordinates of displacement profile is enclosed in Appendix D

Table 3.12. Model parameters for S5

E_{50}^{ref} (kN/m^2)	E_{oed}^{ref} (kN/m^2)	n	ϕ (deg)	R_f
11,000	6,480	0.52	34	0.86

3.5.2.2 Depth of maximum moment

Actual depth of maximum moment is where largest recorded strain during loading occurred. In numerical model, it is the depth that provides highest axial stress/force in circumferential shell member of pile section (Table 3.13). Recorded strain profiles show that for first three pushes, maximum strains were at 1.49 m, and strains at depths of 0.9m, 1.2m and 1.49 m are similar. Meanwhile, numerical analysis gives the depth of maximum moment at about 1.2m. That proves numerical analysis has good agreement in predicting depth of maximum moment with experimental results. Point of fixity from numerical analysis is at depth of about 3m.

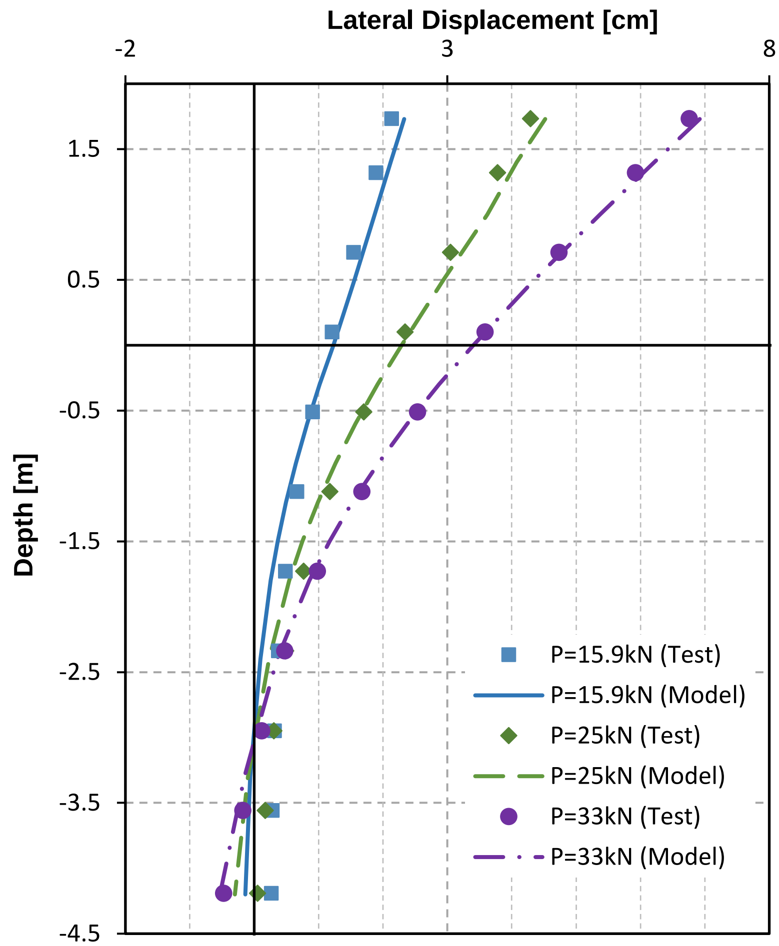

Figure 3.10. Lateral displacement profiles by numerical analysis and pile test for S5

Table 3.13. Maximum axial force (kN/m) in shell element – S5

Load (kN)	**15.9**	**25**	**33**
z=0.9 m	182.3	290	384.4
z=1.2 m	184.7	295.7	392.7
z=1.5 m	180.1	290.7	387

3.5.3 Parameters verification for pile S6

3.5.3.1 Distribution of vertical stress due to surcharge

Distribution of vertical stress due to K_0-consolidation and surcharge for points adjacent to pile is presented in Figure 3.11. Additional stress by post-tension force applying on two semi-circular plates leads to increase in soil modulus and largest increase occurs at depths between 0.6m to 2m.

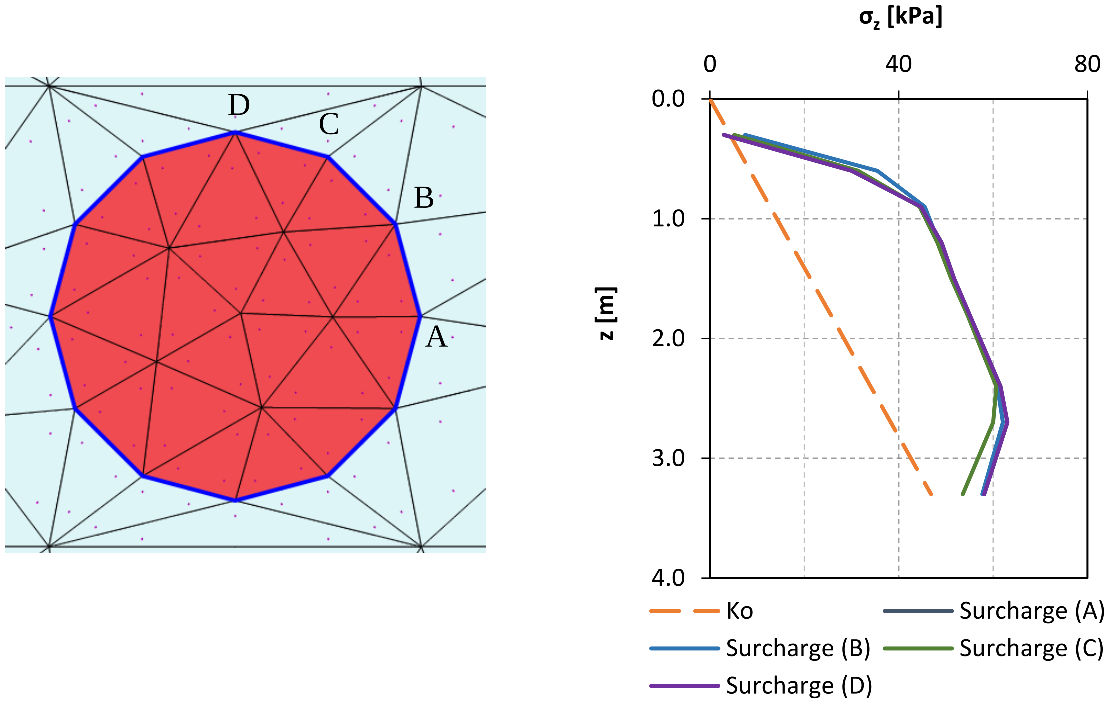

Figure 3.11. Distribution of vertical stress due to self-weight and surcharge

3.5.3.2 3D analysis displacement profiles versus experimental data

With model parameters presented in Table 3.14, numerical analysis provides pile deflection profiles very similar to testing data of S6. Displacement profiles at lateral loads of 17.5 kN, 27.1 kN and 41 kN are plotted in Figure 3.12. Coordinates of displacement profile is enclosed in Appendix D

Table 3.14. Model parameters for S6

E_{50}^{ref} (kN/m^2)	E_{oed}^{ref} (kN/m^2)	n	ϕ (deg)	R_f
8,600	5,075	0.52	32	0.86

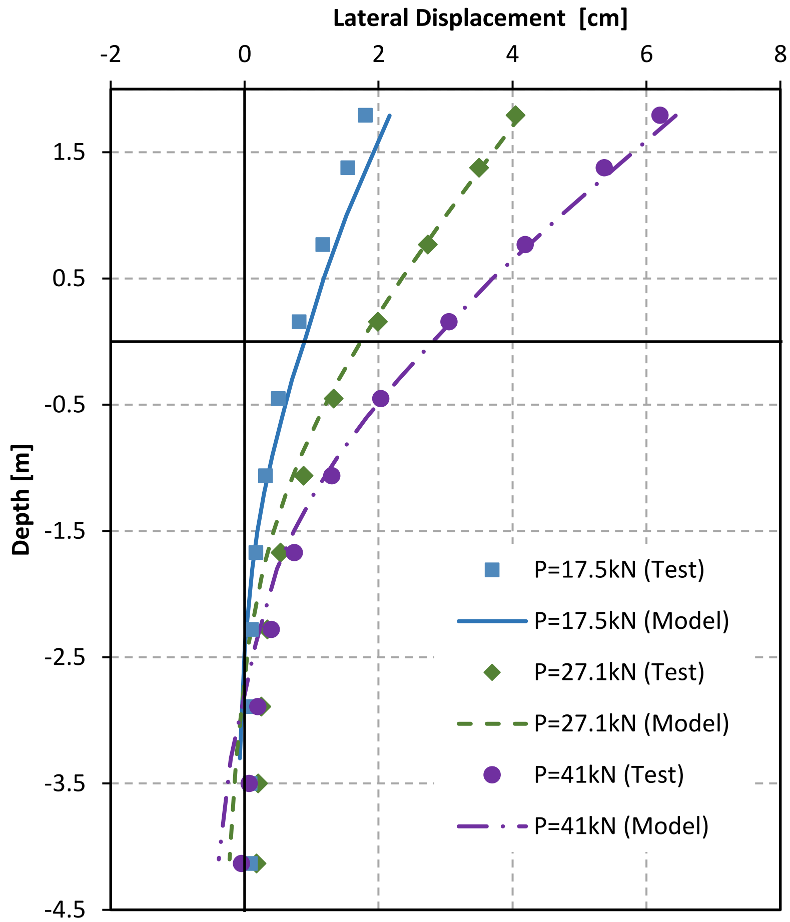

Figure 3.12. Lateral displacement profiles by numerical analysis and pile test S6

3.5.3.3 Depth of maximum moment

Experimental data of pile test S6 shows that maximum moment occurred at depths from 0.82m to 1.12m. Meanwhile numerical analysis reports maximum axial force in shell element at 0.9m (Table 3.15), which is shallower than that in pile test S5 (1.2m)

Table 3.15. Maximum axial force (kN/m) in shell element – S6

Load (kN)	17.5	27.1	41
z=0.6 m	192.1	298.5	456.2
z=0.9 m	196.4	307.7	474.4
z=1.2 m	190.4	301.6	470.1

3.5.4 P-y curves resulted from numerical analyses

3.5.4.1 P-y curves for testing condition 1

Since cyclic loading has insignificant effect on soil-pile interaction in first three cycles, p-y curves for two cases are identical. P-y curves are extracted from numerical results by Fan and Long (2005) recommendation. Soil reaction is the resultant of stresses at 32 closest points to pile section perimeter (see Figure 3.13). Soil reaction component at each point is computed by multiplying traction vector T_x by distributed circumferential length (dash blue circle). As pile section is described by a regular polygon with 12 edges, reactions of a group of two or three points is summed up at their shared vertex. Reactions at vertices show distribution of soil reactions over section height (Figure 3.14) and sum of them is total soil reaction on pile.

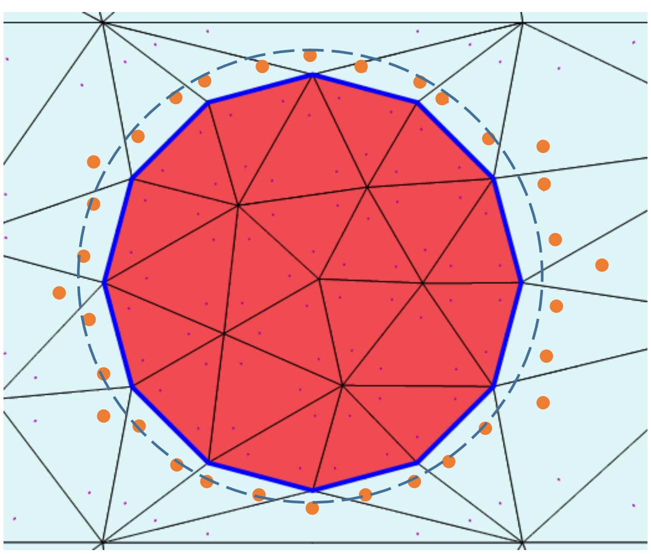

Figure 3.13. Stress points for computing soil reaction

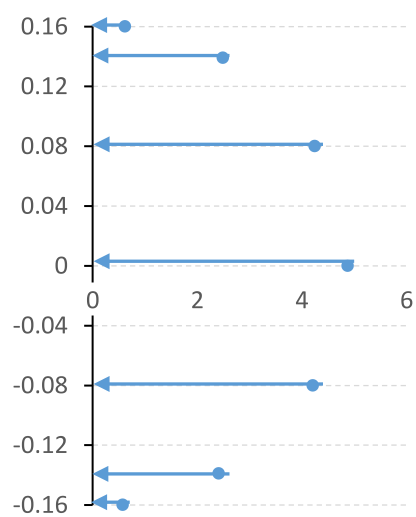

Figure 3.14. Typical distribution of reaction over section height

P-y curves at depths of 0.3m, 0.6m, 0.9m, 1.2m, 1.8 and 2.4m for testing condition 1 including boundary and surcharge of 5kPa are presented in Table 3.16 and

Figure 3.15. These set of p-y curves will be discussed in comparison with the set for testing condition 2 on impact of surcharge and with another one for free-field case on effect of boundary condition in next sections.

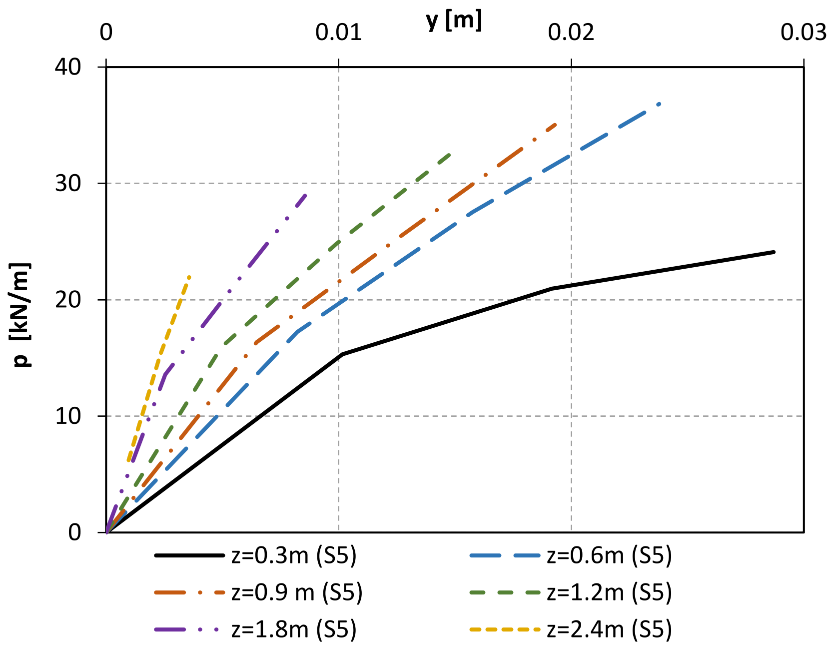

Figure 3.15. P-y curves resulted from numerical analysis for testing condition 1

Table 3.16. P-y responses from numerical analyses – S5

z=0.3m		**z=0.6m**		**z=0.9m**	
y (m)	**p (kN/m)**	**y (m)**	**p (kN/m)**	**y (m)**	**p (kN/m)**
0	0	0	0	0	0
0.010	15.3	0.008	17.2	0.006	16.4
0.019	20.9	0.016	27.5	0.013	25.4
0.029	24.1	0.024	36.8	0.019	35.0
z=1.2m		**z=1.8m**		**z=2.4m**	
y (m)	**p (kN/m)**	**y (m)**	**p (kN/m)**	**y (m)**	**p (kN/m)**
0	0	0	0	0	0
0.005	15.9	0.003	13.6	0.001	6.2
0.010	24.8	0.005	21.1	0.002	15.3
0.015	33.2	0.009	28.9	0.004	21.9

3.5.4.2 P-y curves for testing condition 2

P-y curves at depths of 0.3m, 0.6m, 0.9m and 1.2m, and 1.8m for testing condition 2 including boundary and surcharge of 50.8kPa, are described in Table 3.17 and Figure 3.16. Data shows that p-y curves at depths of 0.6, 0.9 and 1.2m are almost identical and likely yet to reach ultimate soil resistance at first yield of pile. Figure 3.17 compares numerical analysis based p-y curves for S5 and S6 and show significant changes in p-y curves due to large surcharge on ground. The surcharge improved substantially modulus of subgrade reaction and ultimate resistance at every depth. P-y curves at depths of 0.6m, 0.9m and 1.2m for pile test S6 have similar initial slope as p-y curve at depth 1.8m for pile test S5 does but they definitely possess larger ultimate resistance than their counterpart. Increase in effective stress in ground leads to huge improvement in soil-pile system performance.

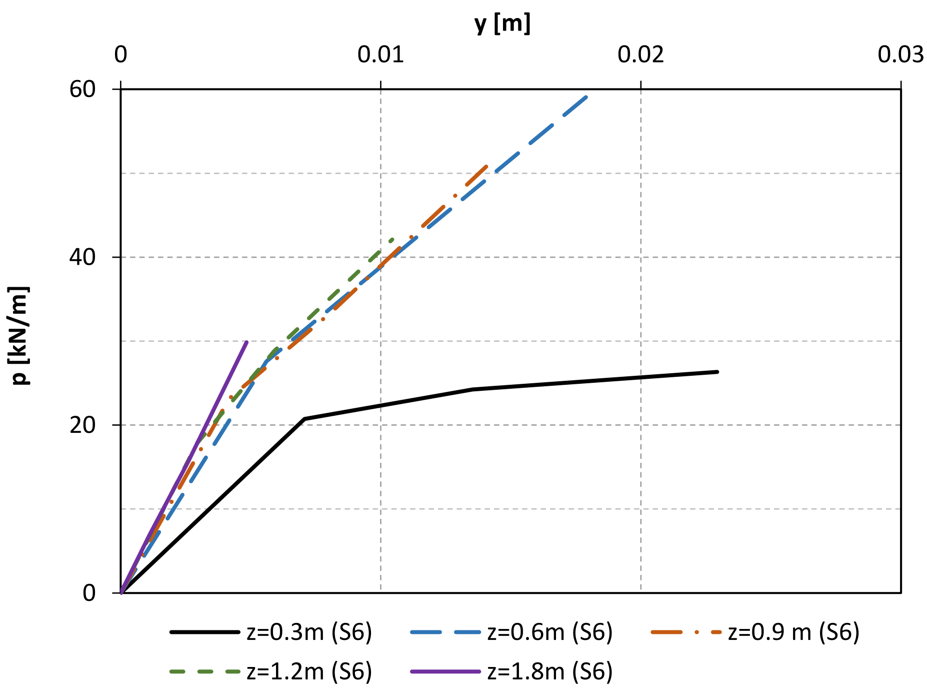

Figure 3.16. P-y curves resulted from numerical analysis for testing condition 2

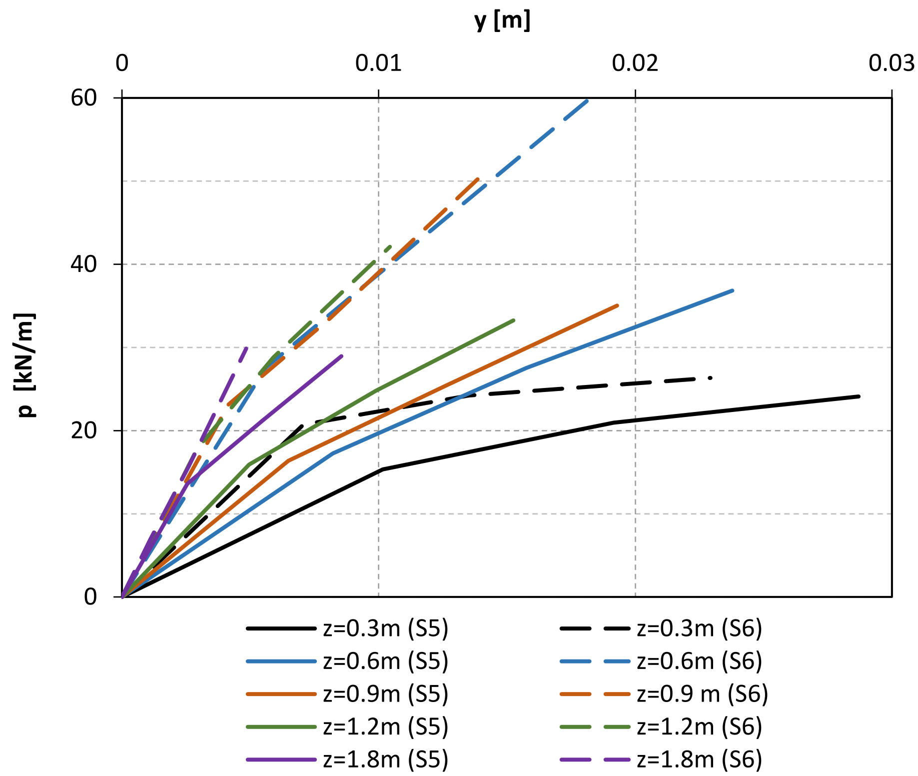

Figure 3.17. Comparison of p-y curves for S5 and S6

Table 3.17. P-y responses from numerical analyses – S6

z=0.3m		**z=0.6m**		**z=0.9m**		**z=1.2m**		**z=1.8m**	
y m	**p kN/m**	**y m**	**p kN/m**	**y m**	**p kN/m**	**y m**	**p kN/m**	**y m**	**p kN/m**
0	0	0	0	0	0	0	0	0	0
0.007	20.7	0.006	27.9	0.004	23.1	0.003	17.9	0.001	6.9
0.014	23.9	0.011	38.9	0.008	33.4	0.006	28.4	0.003	15.6
0.023	26.3	0.018	60.1	0.014	50.8	0.010	42.4	0.005	29.9

3.6 Calibrated model parameters versus triaxial testing parameters

Bases on calibrated parameters for pile test S5 (Table 3.12), initial modulus and relative density for soil is computed from equations 3.7 and 3.6 as follows:

$$E_i^{ref} = \frac{2E_{50}^{ref}}{(2-R_f)} = 19,820\ \mathrm{kN/m^2}$$

$$D_R = \frac{\left(\frac{E_i^{ref}}{100} - 90\right)}{10.36} = 10.44\%$$

Similarly, calibrated model parameters for pile test S6 (Table 3.14) provides initial modulus of 15,495 kN/m^2 corresponding to relative density of 6.3%. These values of relative density are very close to that obtained from lab testing result for depth of 0.15m, which are 10% and 6.7% for pile tests S5 and S6, respectively (Table 3.7). Although soil unit weight and relative density likely increase with depth, this outcome indicates that modulus from axial compression triaxial test represents soil behavior very well and could be use as representative modulus for whole soil medium. These outcomes allow using set of soil properties corresponding to a relative density (Table 3.6) without modification in numerical analysis for parametric study. However, a rigorous report on in-situ relative density by in-situ testing methods is required to establish a relationship between calibrated E_{50}^{ref} and soil modulus resulted from AC test.

Brinkgreve (2005) cited a relation between D_R and E_{50}^{ref}, given as $E_{50}^{ref} = 60D_R \quad [\mathrm{MPa}]$ with values varying from 15 MPa for loose to 50 MPa for dense sand. The relation is not particular for laterally loaded pile problem but for Hardening soil model in general. It yields D_R=18.3% for $E_{50}^{ref} = 11\,\mathrm{MPa}$. A verification on in-situ relative density is required to assesses this equation and suggests modification, if needed.

$E_{oed}^{ref} / E_{50}^{ref}$ ratio of 0.59 is reported from calibrated parameters and can be used as a reference for future analyses. Since tested piles were installed by means of liquefaction of soil, and in analysis K_0 for normally consolidated condition was applied, this ratio would be more appropriate for similar situation, e.g. for drilled shaft. If soil is significant displaced or densified during installation, this ratio should be assessed.

3.7 Parametric study and p-y curves for free-field conditions

3.7.1 Soil-pile interaction in free-field conditions

The calibrated model is extended to free-field condition by enlarging domain size to an extent the that the boundary has negligible effect on soil-pile system performance. In order to achieve more data point for p-y curves, analyses are performed at 9 values of load of 5 kPa, 10 kPa, 15.9 kPa, 20 kPa, 25 kPa, 28 kPa, 33 kPa, 41kPa and 45 kPa. This set includes 15.9 kPa, 25 kPa and 33 kPa, which are experimental load values, aimed at comparison of soil-pile performance in bounded and unbounded conditions. 41kN was the force at predicted first yield displacement in pile test S5; however, it was an underprediction since maximum tensile strain at the load was less than yield strain of steel tube. Therefore, lateral load of 45 kN is taken into analysis. Displacement profiles, points of maximum moment and fixity, and p-y curves are aspects to be examined.

3.7.1.1 Domain size

Size of domain that ensures negligible boundary effect has been reported by several researchers (Table 3.18). Two researches with parametric studies by Stewart, *et al.* (2007) and Zhang and Ahmari (2013) provided R_{domain}/D_{pile} ratios of 11 and 20, respectively. Therefore, two analyses are performed with these ratios to select the suitable size for further investigation. Displacement profiles of pile subjected to lateral load of 32 kN in 8 m wide x 8 m long and 13m x 13m domains are illustrated in Figure 3.18. It can be concluded that 8m x 8m field still exhibits some degree of boundary effect. Therefore, soil domain of 13m x 13 m with the pile at the center is selected to analyze laterally loaded single pile in free-field condition (see Figure 3.19). Soil strata and model parameters are kept the same as in analysis of pile test S5 (Table 3.12).

Table 3.18. Reported domain size for free field condition

Authors	D_{pile} (m)	R_{domain}/D_{pile}	Remarks
Fan and Long (2005)	0.63	32	
Yang and Jeremić (2005)	0.43	13	
Stewart, *et al.* (2007)	0.6	11	Parametric study
Karthigeyan, *et al.* (2007)	1.2	20	
Kim and Jeong (2011)	1.0 and 2.4	11.5	
Zhang and Ahmari (2013)	0.91 to 1.22	20	Parametric study

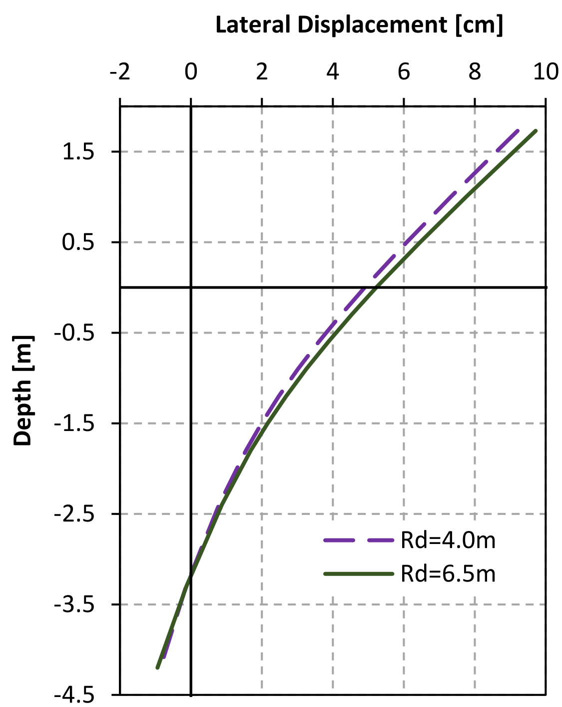

Figure 3.18. Pile deflection in domain size of 8m and 13m

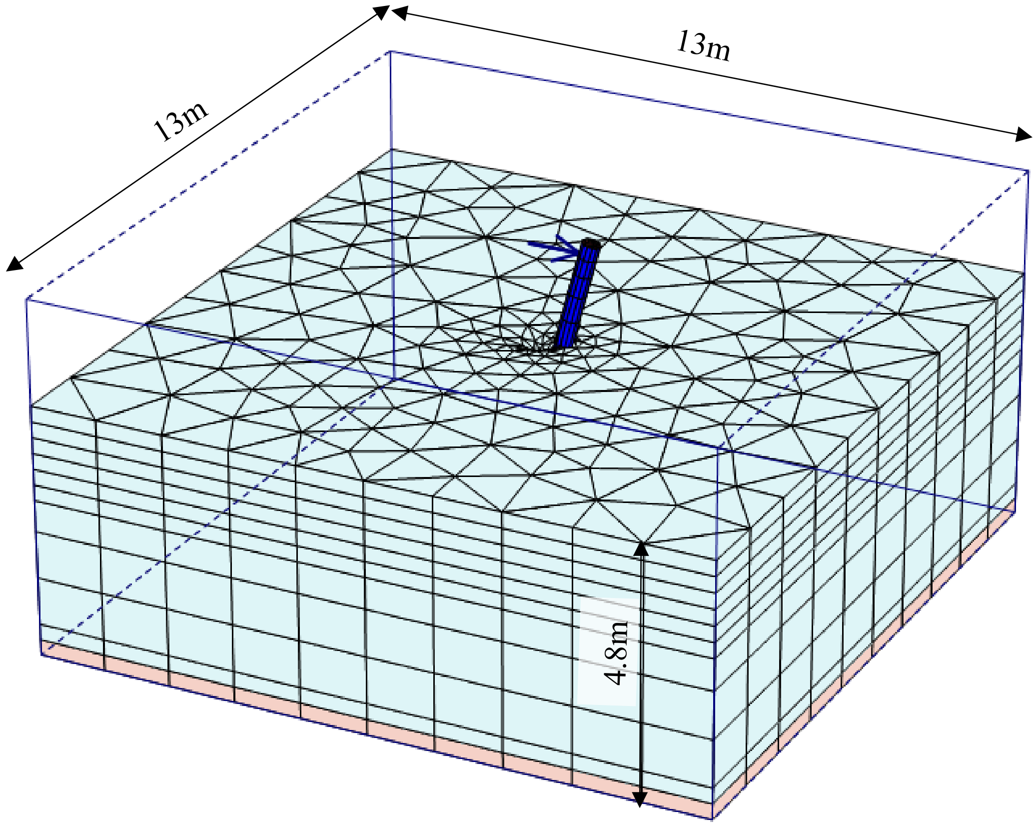

Figure 3.19. Soil domain for analyses in free-field condition

3.7.1.2 Effect of testing boundary on displacement profile

Figure 3.20 illustrates pile deflection profiles at nine aforementioned loading values in free-field condition. 10% in brackets indicates soil relative density in order to differentiate from other packing states of soil. A comparison with numerical results for pile S5 at testing loads are presented in Figure 3.21. Apparently pile has significantly larger displacement in free condition; in other words, boundary condition in laboratory hindered pile displacement and improved pile-soil system performance. Pile displacement data in free-field condition is presented in Appendix E

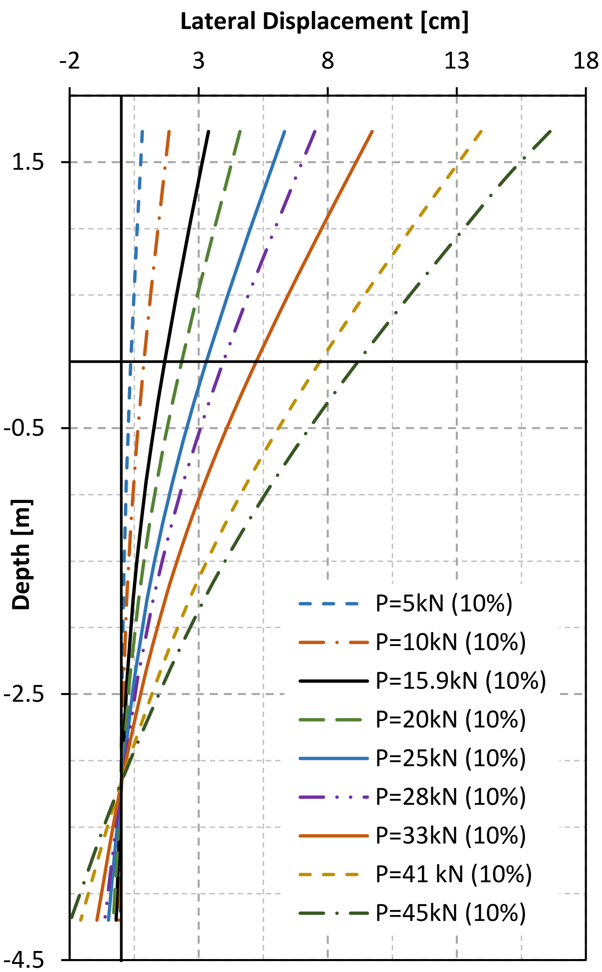

Figure 3.20. Pile displacement profiles in free-field condition

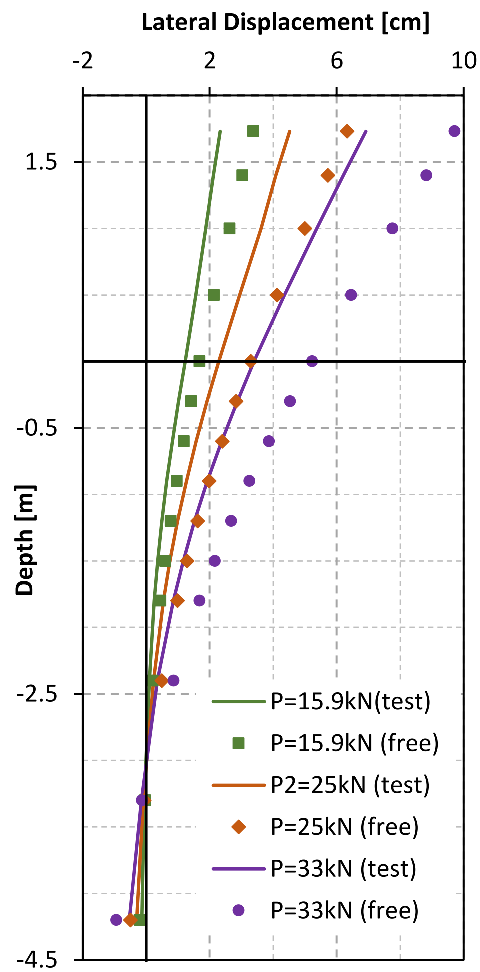

Figure 3.21. Comparison of pile displacement profiles in testing and free-field conditions

3.7.1.3 Effects of testing boundary on depths of maximum moment and fixity

Depth of maximum moment is similar to that in testing condition, which is 1.2m for all the loads. Since figures at P=15.9 kN, 25 kN and 33 kN are consistently larger than those in testing condition (Table 3.19). Therefore, moment demand for pile in free-field condition is higher. Point of fixity relocates down slightly to depth of some 3.2m, which is not significantly different from that in testing conditions (3 m)

Table 3.19. Axial force (kN/m) in shell element for free-field condition

Load (kN)	5	10	15.9	20	25	28	33	41	45
z =0.9	56.7	115.6	186.7	235.4	295.4	331.6	392.9	491.4	541.2
z=1.2	56.8	117.8	192	242.4	304.5	342	405.5	508.1	560.5
z=1.5	54.3	115.3	190.3	241.1	303.3	340.7	403.9	506	558.3

3.7.1.4 Effect of boundary condition on p-y curves

P-y curves for depths of 0.3m, 0.6m, 0.9m, 1.2m, 1.8m and 2.4m resulted from analysis of laterally loaded pile in free-field condition are shown in Figure 3.22. Figure 3.23 compares these relationships with those in testing condition. It is obvious that experimental boundary condition increases ultimate soil resistance at every depth. Lateral modulus of subgrade reaction likely is the same in both cases at depths from 0.3m to 1.2m; however, at 1.8m and 2.4m, the graph indicates an increase in initial slope, which is due to boundary effect.

Another comparison is made between API-based p-y curves for static load and those results from numerical simulation for unbounded condition. Table 3.20 describes input for API p-y curves, in which k_h is selected regarding to friction angle (Figure 3.24). Coefficient A for ultimate reaction is computed by recommendation of Reese, *et al.* (1974), which is expressed by equation 3.8. Values of ultimate resistance is tabulated in Table 3.21

$$\begin{cases} A = 0.9 \quad \text{for cyclic loading} \\ A = \max\{0.9; 3 - 0.8z/D\} \text{ for static loading} \end{cases} \tag{3.8}$$

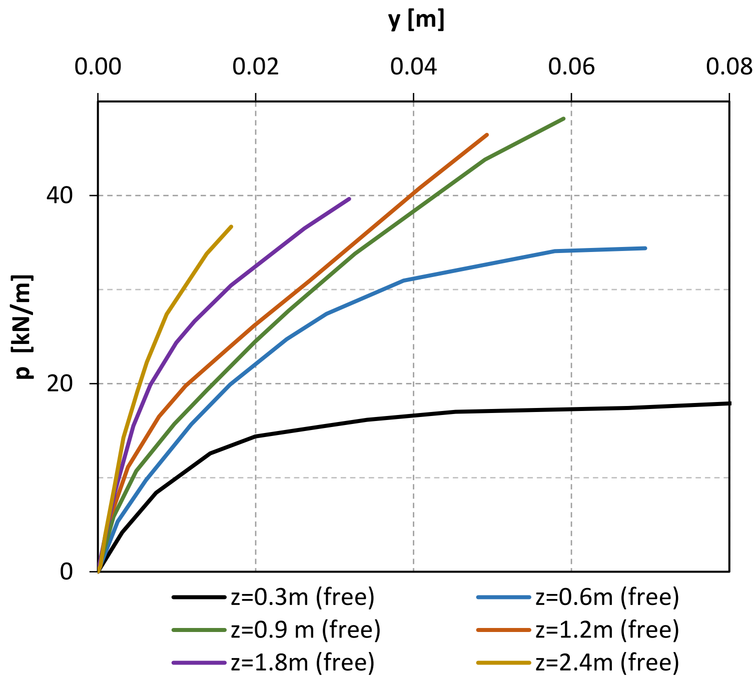

Figure 3.22. p-y curves in free-field condition

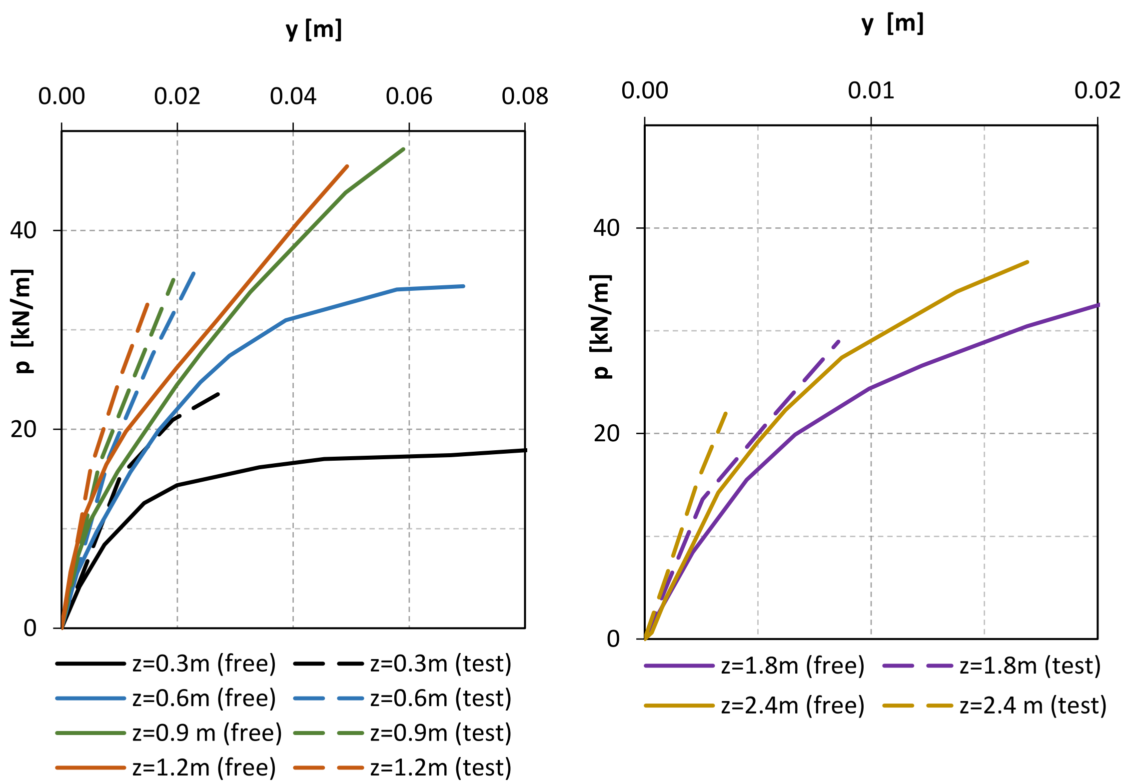

Figure 3.23. Comparison of p-y curves in testing (S5) and free-field conditions

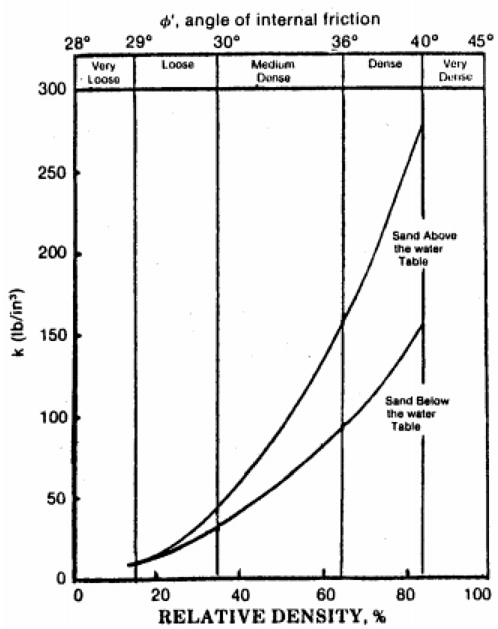

Figure 3.24. Modulus of subgrade reaction (API, 2000)

Table 3.20. Input for API p-y curves

γ_d (kN/m3)	z_1 (m)	z_2 (m)	z_3 (m)	z_4 (m)	z_5 (m)	z_6 (m)	ϕ_1 (deg)	k_h (kN/m3)
14.2	0.3	0.6	0.9	1.2	1.8	2.4	34	31,200

Table 3.21. Ultimate soil resistance of API p-y curves for free-field condition

z (m)	0.3	0.6	0.9	1.2	1.8	2.4
p_u (kN/m)	7.41	7.41	44.6	73.4	151.8	258
A	2.25	1.5	0.9	0.9	0.9	0.9
Ap_u (kN/m)	17.8	34.2	40.1	66	136.6	232.2

Figure 3.25 indicates that ultimate soil reactions at depths of 0.3m and 0.6m resulted from numerical analysis are similar to those of API p-y curves. Meanwhile, at z=0.9m numerical analysis gives larger value than API ultimate resistance. Up to first yield of pile, soil resistance is activated fully or significantly at depths up to 1.2m, while reaction of less than 30% of API ultimate resistance is mobilized at depth of 1.8m and

deeper. It is expected that soil resistance between 0.6 and 1.2m continues to play an important role in soil-pile interaction beyond yield of pile.

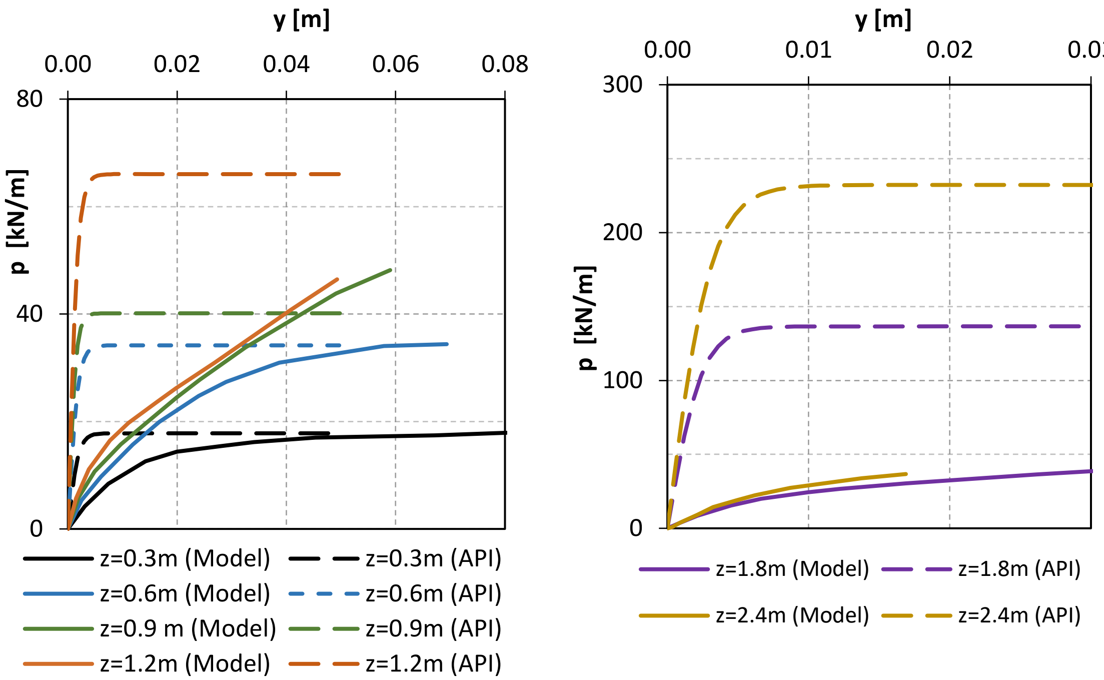

Figure 3.25. Comparison of p-y curves by numerical analysis for free-field condition and API recommendations (k_h=31,200 kN/m^3)

API code overestimates lateral modulus of subgrade reaction, which was also concluded by Yan and Byrne (1992) and Boulanger, *et al.* (2003). High values of k_h leads to pile experiencing little deflection to reach ultimate reaction and underestimation of pile lateral displacement. Therefore, k_h should be corrected, for example by a correction for effect of overburden stress (Boulanger, *et al.*, 2003). Another solution is to choose k_h based on relative density (Figure 3.24). For D_R=10%, k_h=10 lb/in^3 = 2,714 kN/m^3 and this modulus of subgrade reaction produces a set of API p-y curves that better agrees with results from numerical analysis (Figure 3.26). All data on p-y curves for free-field condition is presented in Appendix F

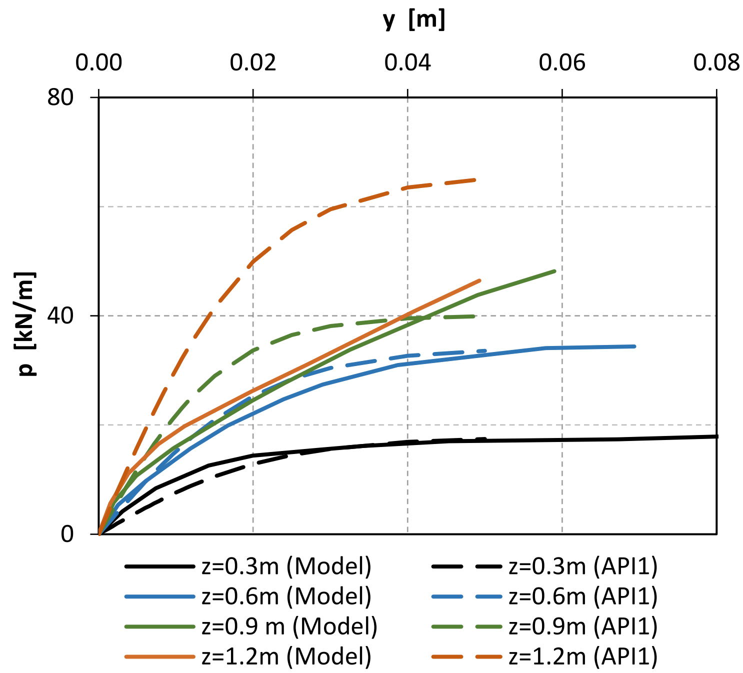

Figure 3.26. Comparison of p-y curves from numerical analysis for free-field condition and API recommendations (k_h=2,714 kN/m^3)

3.7.2 Effect of soil relative density

Analyses are performed for other relative densities of 20% and 40% to investigate influence of denser state of sand to soil-pile interaction. Model parameters are chosen based on Table 3.6 and are shown in Table 3.22. Ratio of $E_{oed}^{ref} / E_{50}^{ref}$ is 0.59 as in analyses of pile S5 and free-field condition with soil relative density of 10%

Table 3.22. Model parameters for D_R of 20% and 40%

D_R (%)	γ_d (kN/m3)	E_{50}^{ref} (kN/m^2)	E_{oed}^{ref} (kN/m^2)	ϕ (deg)	n	R_f
20	14.52	15,870	9,365	34.2	0.52	0.89
40	15.04	29,410	17,350	35.4	0.52	0.86

3.7.2.1 Effect of D_R on p-y displacement profiles

Figure 3.27 illustrate pile deflection due to lateral load for soil at relative densities of 20% and 40%. Figure 3.28 compares pile deflection profiles caused by lateral loads of 15.9 kN, 25 kN and 33 kN in sand with relative densities of 10%, 20% and 40% Obviously, magnitude of pile deflection decreases with increasing relative density

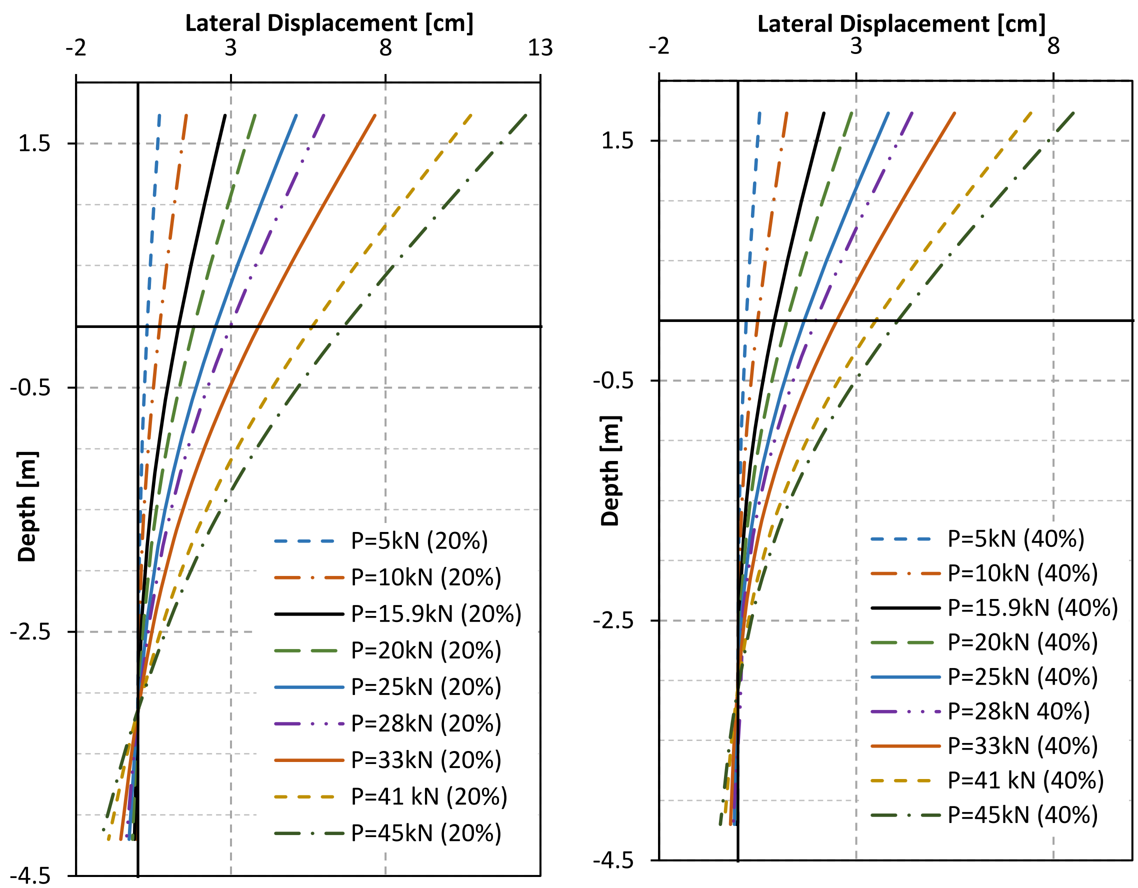

Figure 3.27. Displacement profiles for D_R=20% (left) and D_R=40% (right)

3.7.2.2 Effect of D_R on points of maximum moment and fixity

Maximum axial force in shell element at depths of 0.9m, 1.2m and 1.5m is shown in Table 3.23 and Table 3.24. It can be concluded that point of maximum moment moves slightly upwards as relative density increases. For most loading values, maximum moment is reported at depth of 1.2m; however, at small loads, 5kPa for D_R=20%, and 5kPa, 10kPa and 15.9kPa for D_R=40%, it is at 0.9m deep. Moment demand in pile decreases as soil becomes denser.

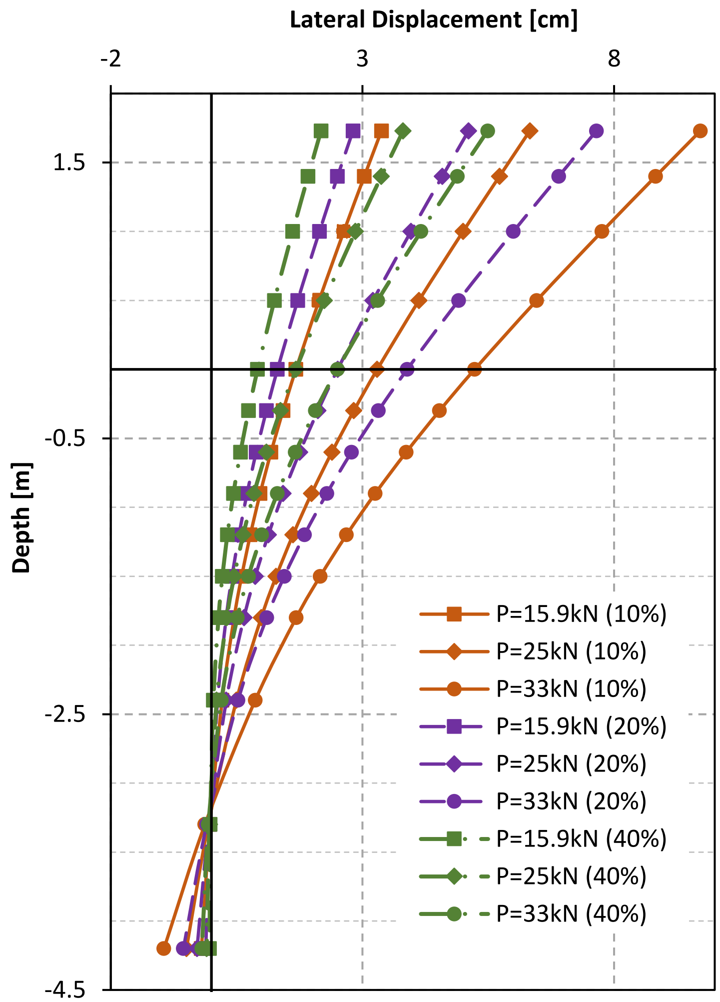

Figure 3.28. Comparison of displacement profiles at different relative densities

Table 3.23. Maximum axial force (kN/m) in shell element for soil at D_R=20%

Load (kN)	5	10	15.9	20	25	28	33	41	45
z =0.9	55.8	114	184.8	233.5	293.6	329.8	391.2	489.8	539.6
z=1.2	55.2	115	188.5	238.9	300.9	338.4	401.9	504.6	556.9
z=1.5	52	111.1	185.2	235.8	297.9	335.2	398.3	500.5	552.7

Table 3.24. Maximum axial force (kN/m) in shell element for soil at D_R=40%

Load (kN)	5	10	15.9	20	25	28	33	41	45
z =0.9	53.8	110.7	180.2	228.3	288.3	324.4	385.5	483.9	533.7
z=1.2	51.8	109.2	180.2	229.4	290.7	327.7	390.7	492.6	544.6
z=1.5	47.1	102.6	172.9	221.6	282.3	318.8	381	481.7	533.3

Depths from 0.9m to 1.2m, which are about 2.8 to 3.8 pile diameters, have largest moment demand, and plastic hinge likely occurs in this region. This portion of pile, and for some distance outside this zone, should be carefully examined and detailed to ensure section flexural strength and ductility for desired limits states. The finding is slightly larger than result of an experimental result by Chai and Hutchinson (2002). The authors reported maximum moment at 2.3D for a reinforce concrete pile with D=0.406m in loose sand with lateral load imposing at level of 6D above ground and embedded length of 13.5D, which is similar to pile in this study. Allotey and El Naggar (2008) performed numerical analysis of Chai and Hutchinson (2002) experiment with Beam on nonlinear Winkler foundation approach and reported the depth of maximum moment at 2.5-3D with API p-y curves and 1.5-2D with Yan and Byrne p-y curves (Yan and Byrne, 1992) for dense sand.

Point of fixity is almost identical for three relative densities, at 3.2m, which is 10D. Therefore, recommended embedded length is greater than this figure. Duncan, *et al.* (1994) suggested minimum pile length for characteristic load method is 8D, 11D and 14D for dense, medium and loose sand, respectively. The finding of this study, thus is reasonable.

3.7.2.3 Effect of D_R on p-y curves

P-y curves for depths of 0.3m, 0.6m, 0.9m, 1.2m, 1.8m and 2.4m and relative densities of 10%, 20% and 40% are presented in Figure 3.29 and Figure 3.30. Since plastic hinge location is expected to be at 1.2m, up to pile first yield soil resistance above this depth is mobilized considerably to fully in all cases, while a significantly smaller portion is activated at lower depths. Figure 3.31 illustrates relation between normalized soil resistance, $p/(\sigma'_{vo}D)$, and normalized displacement, y/D, where σ_z and D are effective overburden stress and pile diameter, respectively. Increase in soil relative density leads to increase in ultimate soil resistance and initial slope of p-y curves. Soil at depth of 0.3m and 0.6m reaches ultimate resistance in all cases and denser soil arrived at ultimate reaction at lower pile normalized deflection.

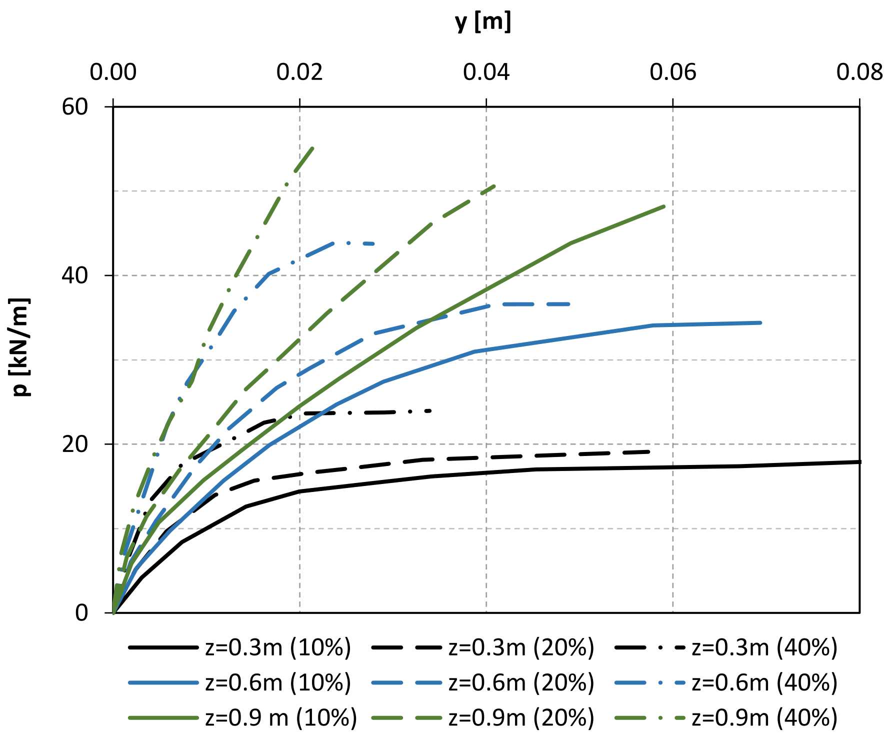

Figure 3.29. P-y curves at depths of 0.3m, 0.6m and 0.9m for various relative densities

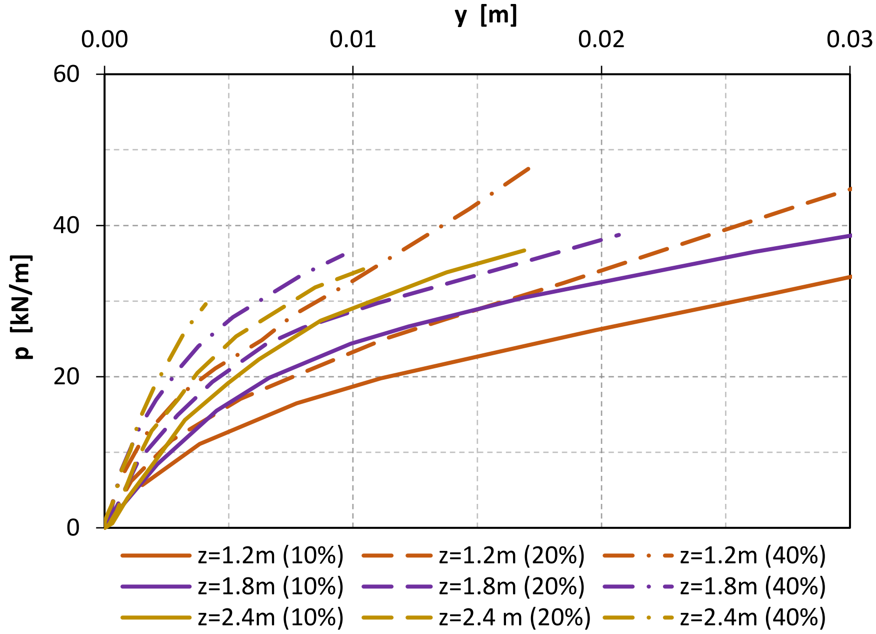

Figure 3.30. P-y curves at depths of 1.2m, 1.8m and 2.4m for various relative densities

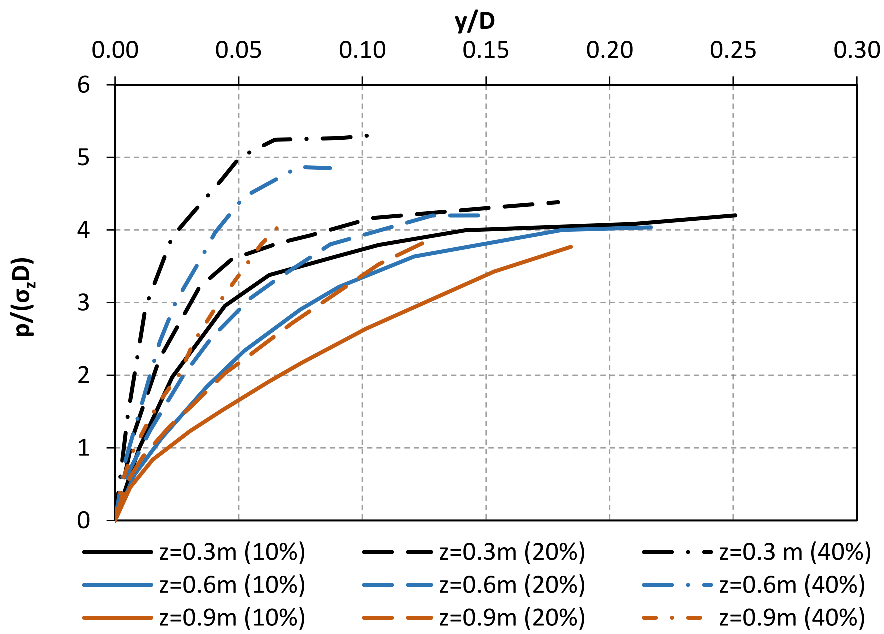

Figure 3.31. Normalized p-y curves for depths of 0.3m, 0.6m and 0.9m for various relative densities

Normalized p-y curves at depths of 0.3m and 0.6m suggests that soil at deeper location likely approaches to ultimate value at lower normalized displacement. At a certain relative density, normalized ultimate soil resistance at 0.3m and 0.6m tends to converge. However, normalized curves for 0.9m are very likely not to follow these trends. The finding suggests that ultimate resistance 0.9m possibly resulted from different failure mechanism from that of above locations.

3.7.2.4 API ultimate resistance versus numerical ultimate resistance

Since p-y curve obtained from numerical analysis at depth of 0.9m possesses higher ultimate resistance than API recommended curve does, comparison is made between p-y curves resulted from two methods for depths 0.6m and 0.9m and all three relative densities. The data for these p-y curves is presented in Appendix F. It can be seen in Figure 3.32 and Table 3.25 that numerical analysis consistently delivers higher ultimate resistance for the depths. The difference at depth of 0.9m is significant.

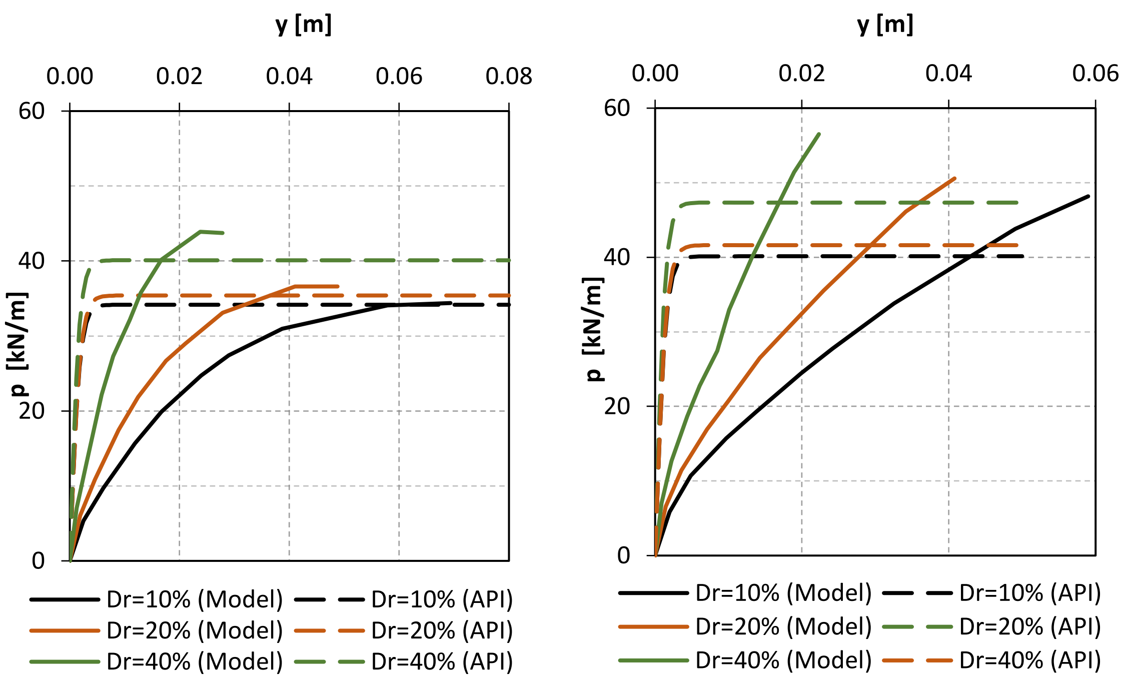

(a) z=0.6m (b) z=0.9m

Figure 3.32. Comparison of API-based and numerical-based p-y curves: (a) at z=0.6m, (b) at z=0.9m

Table 3.25. Comparison of API p_u and numerical analysis-based reaction at P=45kN

z (m)	0.6			0.9		
D_R (%)	10	20	40	10	20	40
p_u (kN/m)	22.8	23.6	26.7	44.6	46.2	52.6
A	1.5	1.5	1.5	0.9	0.9	0.9
Ap_u (kN/m)	34.2	35.4	40.1	40.1	41.6	47.3
p (kN/m) @ P=45kN (FEA)	34.4	36.6	43.7	48.2	50.6	56.5

The finding agrees with an earlier research by Yan and Byrne (1992), who performed small-scale test on piles with diameters varied from 6.35 mm to 12.7 mm in soil tank that had dimension of 445mm in direction of loading. Similar conclusions on modulus of subgrade reaction and ultimate soil resistance were reported when they associated p-y curves computed from testing data with API ones (Figure 3.33). The authors did not discuss on reasons for difference in ultimate resistance values obtained from their tests and API code, instead they proposed new expressions for p-y curves.

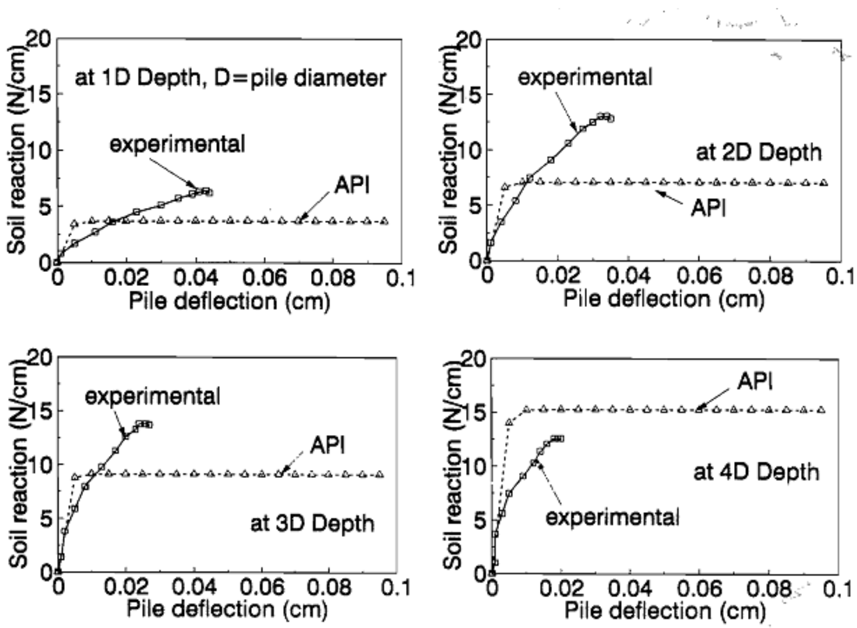

Figure 3.33. Comparison of p-y curves from small-scale test and those recommended by API (Yan and Byrne, 1992)

It is believed that pile flexural displacement causes both lateral and vertical pressures on soil in front of pile. Additional vertical stress leads to larger shear resistance and deeper failure surfaces for depths of 0.6m and 0.9m, instead of passive wedge-type failure assumed by Reese, *et al.* (1974). Therefore, soil lateral ultimate resistance is improved, and vertical reaction provides additional resisting moment that enhance soil-pile system performance. Table 3.26, Table 3.27 and Figure 3.34 illustrate development in vertical stress at point right in front of pile and one pile diameter away at depths of 0.3m, 0.6m, 0.9 and 1.2m as lateral load increases. Since the largest increase is at 0.9m, the gap in maximum resistance by API code and numerical analysis is reasonably larger than at other positions. Increase in vertical stress provides an explanation on little gap between p-y curves at 0.9m and 1.2m in Figure 3.22, and between p-y curves at 0.6m, 0.9m and 1.2 of pile test S6 (Figure 3.16). Distribution of vertical stresses in the center plane in direction of loading (Appendix G) at selected values of load and D_R=10% confirms increase of vertical stress

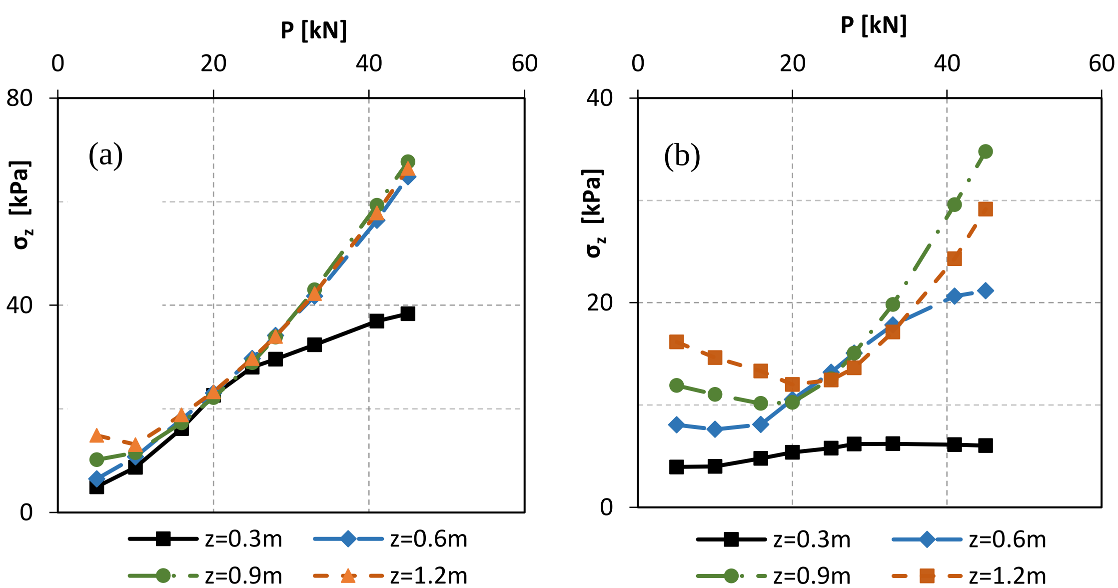

Figure 3.34. Development of vertical stress at depths of 0.3m, 0.6m, 0.9m and 1.2m: (a) right at pile front surface, (b) 1D away from front surface

Table 3.26. Vertical stress σ_z (kPa) at pile front surface, D_R=10%

Load (kN)	5	10	15.9	20	25	28	33	41	45
z=0.3m	8.7	16.2	22.6	28.1	29.6	32.4	36.9	38.4	8.7
z=0.6m	6.5	10.7	18.0	23.1	29.7	34.2	41.7	56.4	64.8
z =0.9m	10.2	11.6	17.3	22.2	28.9	33.8	43.0	59.3	67.7
z=1.2m	14.9	13.1	18.9	23.3	29.7	34.0	42.3	57.8	66.4

Table 3.27. Vertical stress σ_z (kPa) 1D away from pile front surface, D_R=10%

Load (kN)	5	10	15.9	20	25	28	33	41	45
z=0.3m	4.0	4.0	4.8	5.4	5.8	6.2	6.2	6.1	6.0
z=0.6m	8.1	7.6	8.1	10.5	13.2	15.1	17.8	20.6	21.2
z =0.9m	11.9	11.0	10.1	10.3	12.6	15.1	19.8	29.6	34.8
z=1.2m	16.2	14.6	13.3	12.0	12.5	13.6	17.1	24.3	29.1

3.8 Conclusions and Recommendations

Model parameters were successfully validated by experimental results of two piles with bounded condition and very different values of surcharge (5 kPa and 50.8 kPa), and were extended to free-field condition. P-y curves were generated for testing and free-field conditions to investigate effects of boundary, cyclic loading, surcharge and soil relative density. Following conclusions are drawn from the investigation:

- Cyclic loading had insignificant effect and could be neglected in first three cycles of loading calibrated in numerical analysis. Therefore, p-y curves for cyclic and static loads were identical,
- Boundary improved soil-pile system performance, particularly decreased pile displacement and moment demand. Ultimate soil resistance of p-y curves

increased in all selected depths, and indication of increase in modulus of subgrade reaction was found at depth of 1.8m and greater. Surcharge of 50.8 kPa changed effective stress pattern in soil substantially, resulting in significant increase in soil resistance and modulus of subgrade reaction. Surcharge also led to shallower point of maximum moment. Modulus of subgrade reaction appeared to be stress-dependent.

- Parametric study on soil relative density showed that higher relative density gives higher ultimate soil resistance and initial slope of p-y curves. Denser soil reached ultimate resistance at lower pile deflection. Relative density had insignificant impact on locations of maximum moment and fixity although these points tended to move upward with increasing density. Moment demand of pile decreased as relative density increased. Point of maximum moment appeared at 1.2m (3.8D) and fixity was at 3.2m (10D) for three selected relative densities although location of maximum moment moved slightly upward as relative density increased.

- API recommended lateral modulus of subgrade reaction, which was selected according to friction angle, was excessively large for soil in this study due to soil low relative density and pile installation by sand liquefaction. Selection of k_h based on D_R was better for this case.

- Soil resistance was mobilized significantly above point of maximum moment, of which it was fully mobilize at depths of 0.3m and 0.6m. Ultimate resistance at these positions were similar to that computed by API equations, although the curve at 0.6m exhibited larger value than API one. However, ultimate resistance at 0.9m was significantly larger than API figure and it was not reached yet at yielding of pile. Vertical stress caused by pile rotation in soil medium was believed to improve shear resistance and alter failure surface for this depth, resulting in larger ultimate reaction. Therefore, API -based p-y curves was suggested to underpredict pile displacement at low range of lateral load, and overpredict pile displacement at large loading values.

- Calibrated model parameters agreed with soil testing properties from axial compression triaxial test, proving that modulus and shear strength parameters resulted from this stress path could be used as representative properties for whole domain. However, recommended relation between model reference modulus and soil relative density was not established due to lack of rigorous relative density investigation over the depth of soil pit. Ratio of $E_{oed}^{ref} / E_{50}^{ref} = 0.59$ was recommended for 3D numerical analysis using Hardening soil model for comparable problems (NC soil, non-displacement pile)
- Numerical simulation for pile tests can be improved by considering interface interaction between soil and pit wall and between soil and concrete plates, and rigidity of plates. This factors were not included in simulation due to limitation of the software and could be addressed by newer version. Pressure cells data was not employed to calibrate model parameters and could be done in more comprehensive simulation

4. SUMMARY OF CONCLUSIONS

4.1 Summary

Soil experiments and three-dimensional analyses on laterally loaded piles were performed to determine p-y curves for sands. Soil classification tests and sixteen triaxial tests with axial compression stress path provided necessary geotechnical parameters for strength and deformation analyses. Shear strength parameters resulted from axial compression tests were used to generate API recommended p-y relationships, and a simple procedure to construct API-like p-y curves directly from triaxial stress-strain responses was proposed.

Area correction was concluded to have most significant impact on testing data reduction among assessed factors and was recommended to be considered in processing recorded testing information.

A relation between soil relative density and modulus number was established, and it appeared as a straight line expressed as $K=10.36D_R+90$. This relationship helped selecting model parameters in numerical analyses and associating calibrated model parameters and experimental ones.

Two basic scaling factors for converting axial compression stress-strain relationships to p-y curves were determined. These factors are easy to be computed from characteristic parameters of stress-strain response (peak deviatoric stress and axial strain at peak) and p-y curves (ultimate soil response), soil friction angle and pile diameter.

Two large-scale pile tests in soil pit were successfully simulated in 3D finite element models to confirm model parameters and extend model to free-field conditions, where true soil-pile interaction was examined. Effects of cyclic loading, boundary condition, surcharge and relative density were assessed and discussed. Testing boundary condition was proved to increase lateral modulus of subgrade reaction and ultimate soil resistance, resulting in lower pile deflection and moment demand. Surcharge induced additional vertical stress, which in turn improves p-y curves characteristic parameters. Increasing relative density in unbounded condition led to higher soil reaction at given pile deflection and ultimate soil resistance, and lower displacement and moment demand in pile.

Comparison of p-y curves resulted from numerical analysis for free condition and those recommended by API showed some significant differences. API modulus of subgrade reaction was excessively large, and API ultimate soil resistance was lower for depths from 0.6m to 1.2m (point of maximum moment). Analyses using API -based p-y curves, therefore, were concluded to underpredict of pile deflection at low lateral load, and overpredict it at large loading values. Additional vertical stress on soil due to pile rotation was believe to change failure surface and increase soil ultimate resistance.

Soil modulus and shear strength parameters resulted from axial compression triaxial test could be used as representative soil parameters for surrounding soil medium. Reference model modulus E_{50}^{ref} showed association with soil relative density; however, it was not explicitly defined. Ratio of $E_{oed}^{ref} / E_{50}^{ref} = 0.59$ was recommended for 3D numerical analysis using Hardening soil model for comparable problems.

4.2 Recommendations for future researches

It is recommended to perform more 3D numerical analyses on published pile experiments in sandy soils with reliable data on soil relative density in order to draw relationship between model reference modulus E_{50}^{ref} and D_R, and to assessed $E_{oed}^{ref} / E_{50}^{ref}$ ratio in different range of D_R and pile installation methods. Determining relationship between E_{50}^{ref} and data of in-situ tests is also recommended. It also should be done for clayey soils and layered ground. For clays, undrained shear strength is effective stress dependent and could be determined by SHANSHEP method (Ladd and Foott, 1974) as: $s_u / \sigma'_{vo} = S(OCR)^m$, and undrained modulus E_u=Ks_u (Duncan and Buchignani, 1976), where K is a factor as a function of OCR and plastic index (PI).

3D numerical simulation shows its potential to perform analyses of laterally loaded single pile in free-head condition. Newer version of Plaxis 3D Foundation, which is able analyzing of restrained-head single pile and possesses better set of properties for pile element, allows investigating on effect of soil-pile interaction on sequence of formation of above and in ground plastic hinges. It also could be extended to analysis of pile group, particularly in distribution of load to individual pile and occurrence order of plastic hinges under influence of soil-pile interaction. Analysis of soil pile interaction with nonlinear also can be performed.

Research on failure mechanism and ultimate soil resistance with consideration of vertical stress due to rotation of pile should be performed as it significantly impacts soil-pile system performance and characteristic parameters of p-y curves. Parametric study on effects of soil-pile interface properties and pile stiffness on development of vertical stress is also recommended.

5. REFERENCES

Airey, D. W., and Wood, D. M. (1988). "The Cambridge true triaxial apparatus." *Advanced Triaxial Testing of Soil and Rock, ASTM STP 9*, R. T. Donaghe, R. C. Chaney, and M. L. Silver, eds., American Society for Testing and Materials, Louisville, Kentucky, 796-805.

Allotey, N., and El Naggar, M. H. (2008). "Generalized dynamic Winkler model for nonlinear soil–structure interaction analysis." *Canadian Geotechnical Journal*, 45(4), 560-573.

Allotey, N., and El Naggar, M. H. (2008). "A numerical study into lateral cyclic nonlinear soil–pile response." *Canadian Geotechnical Journal*, 45(9), 1268-1281.

API (2000). "Recommeded Practice for Planning, Designing, and Constructing Fixed Offshore Platforms - Working Stress Design, 21st Edition." API Recommended Practice 2A-WSD. American Petrolium Institute.

ASTM-D7181 (2011). "Method for Consolidated Drained Triaxial Compression Test for Soils." ASTM International.

Baldi, G., and Nova, R. (1984). "Membrane Penetration Effects in Triaxial Testing." *Journal of Geotechnical Engineering*, 110(3), 403-420.

Berre, T. (1982). "Triaxial Testing at the Norwegian Geotechnical Institute." *Geotechnical Testing Journal*, 5(1), 3-17.

Bishop, A. W., and Green, G. E. (1965). "The Influence of End Restraint on the Compression Strength of a Cohesionless Soil." *Géotechnique*, 15(3), 243-266.

Black, D. K., and Lee, K. L. (1973). "Saturating laboratory samples by back pressure." *Journal of the Soil Mechanics and Foundations Division. Proceedings of ASCE* 99(SM1), 75-93.

Bohac, J., and Feda, J. (1992). "Membrane Penetration in Triaxial Tests." *Geotechnical Testing Journal*, 15(3), 288-294.

Bouafia, A. (2007). "Single piles under horizontal loads in sand: determination of P–Y curves from the prebored pressuremeter test." *Geotechnical and Geological Engineering*, 25(3), 283-301.

Boulanger, R. W., Curras, C. J., Kutter, B. L., Wilson, D. W., and Abghari, A. (1999). "Seismic Soil-Pile-Structure Interaction Experiments and Analyses." *Journal of Geotechnical and Geoenvironmental Engineering*, 125(9), 750-759.

Boulanger, R. W., Kutter, B. L., Brandenberg, S. J., Singh, P., and Chang, D. (2003). "Pile foundations in liquiefied and laterally spreading ground during earthquakes: Centrifuge experiments and analyses." Report No. UCD/CGM-03/01. University of California at Davis.

Bouzid, D. A., Bhattacharya, S., Dash, S. R., and (2013). "Winkler Springs (p-y curves) for pile design from stress-strain of soils: FE assessment of scaling coefficients using the Mobilized Strength Design concept." *Geomechanics and Engineering*, 5(5), 379-399.

Briaud, J., Smith, T., and Meyer, B. (1984). "Laterally Loaded Piles and the Pressuremeter: Comparison of Existing Methods." *Laterally Loaded Deep Foundations: Analysis and Performance*, J. Langer, E. Mosley, and C. Thompson, eds., ASTM International, West Conshohocken, PA, 97-111.

Brinkgreve, R. B., and Broere, W. (2006). "PLAXIS 3D Foundation Material Models Manual, version 1.5." PLAXIS Inc.

Brinkgreve, R. B., and Vermeer, P. A. (1997). "Plaxis finite element code for soil and rock analysis-Version 7." Balkema, Rotterdam.

Brinkgreve, R. B. J. (2005). "Selection of Soil Models and Parameters for Geotechnical Engineering Application." *Soil Constitutive Models*, 69-98.

Brown, D. A., and Shie, C.-F. (1990). "Three dimensional finite element model of laterally loaded piles." *Computers and Geotechnics*, 10(1), 59-79.

Budek, A. M., Priestley, M. J. N., and Benzoni, G. (2000). "Inelastic Seismic Response of Bridge Drilled-Shaft RC Pile/Columns." *Journal of Structural Engineering*, 126(4), 510-517.

Byrne, P. M., Cheung, H., and Yan, L. (1987). "Soil parameters for deformation analysis of sand masses." *Canadian Geotechnical Journal*, 24(3), 366-376.

Byrne, P. M., and Eldridge, T. L. "A three parameter dilatant elastic stress-strain model for sand." *Proc., International Symposium on Numerical Models in Geomechanics*, 73-79.

Chai, Y. H., and Hutchinson, T. C. (2002). "Flexural strength and ductility of extended pile-shafts. II: Experimental study." *Journal of Structural Engineering*, 128(5), 595-602.

Chail, Y. H., Priestley, M. J. N., and Frieder, S. (1991). "Seismic Retrofit of Circular Bridge Columns for Enhanced Flexural Performance." *Structural Journal*, 88(5).

Chaney, R., and Mulilis, J. P. (1978). "Suggested method for soil specimen remolding by wet-raining." *Geotechnical Testing Journal* 1(2), 107-108.

Chaney, R., Stevens, E., and Sheth, N. (1979). "Suggested Test Method for Determination of Degree of Saturation of Soil Samples by <i>B</i> Value Measurement." *Geotechnical Testing Journal*, 2(3), 158-162.

Changho Choi, Pedro Arduino, and Harney, M. D. (2008). "Development of a true triaxial apparatus for sands and gravels." *Geotechnical Testing Journal*, 31(1).

Desai, C. S., Sharma, K. G., Wathugala, G. W., and Rigby, D. B. (1991). "Implementation of hierarchical single surface δ0 and δ1 models in finite element procedure." *International Journal for Numerical and Analytical Methods in Geomechanics*, 15(9), 649-680.

Drucker, D. C., and Prager, W. (1952). "Soil mechanics and plastic analysis or limit design." *Quarterly of Applied Mathematics*, 10(2), 157-165.

Duncan, J. M., and Buchignani, A. L. (1976). "An Engineering Manual for Settlement Studies." Department of Civil Enigneering, University of California, Berkeley. Report No. UCB/GT-76-01.

Duncan, J. M., Byrne, P. M., Wong, K. S., and Mabry, P. (1980). "Strength, stress-strain and bulk modulus parameters for finite element analyses of stresses and movements in soil masses." University of California, Berkeley. Report no. UCB/GT/80-01.

Duncan, J. M., and Chang, C.-Y. (1970). "Nonlinear analysis of stress and strain in soils." *ASCE Journal of the Soil Mechanics and Foundation Division*, 96(5), 1629-1653.

Duncan, J. M., and Dunlop, P. (1968). "The Significance of Cap and Base Restraint " *Journal of the Soil Mechanics and Foundations Division*, 94(1), 271-290.

Duncan, J. M., Leonard T. Evans, J., and Ooi, P. S. K. (1994). "Lateral Load Analysis of Single Piles and Drilled Shafts." *Journal of Geotechnical Engineering*, 120(6), 1018-1033.

Duncan, J. M., and Seed, H. B. (1967). "Corrections for Strength Test Data." *Journal of the Soil Mechanics and Foundations Division*, 93(SM5), 121-137.

El Naggar, M. H., and Novak, M. (1995). "Nonlinear lateral interaction in pile dynamics." *Soil Dynamics and Earthquake Engineering*, 14(2), 141-157.

Elremaily, A., and Azizinamini, A. (2002). "Behavior and strength of circular concrete-filled tube columns." *Journal of Constructional Steel Research*, 58(12), 1567-1591.

Evans, M. D., and Seed, H. B. (1987). "Undrained cyclic triaxial testing of gravels - the effect of membrane compliance." *UCB/EERC-87/08*, Earthquake Engineering Research Center, University of California, Berkeley.

Fan, C.-C., and Long, J. H. (2005). "Assessment of existing methods for predicting soil response of laterally loaded piles in sand." *Computers and Geotechnics*, 32(4), 274–289.

Frost, J., and Park, J. (2003). "A Critical Assessment of the Moist Tamping Technique." *Geotechnical Testing Journal*, 26(1), 1-14.

Frydman, S., Zeitlen, J., and Alpan, I. (1973). "The Membrane Effect in Triaxial Testing of Granular Soils." *Journal of Testing and Evaluation*, 1(1), 37-41.

Fukushima, S., and Tatsuoka, F. (1984). "Strength and deformation of characteristics of saturated sand at extremely low pressures." *Soils and Foundations*, 24(4), 30-48.

Furlong, R. W. (1967). " Strength of Steel-Encased Concrete Beam Columns." *Journal of the Structural Division* 93(5), 113-124.

Gabr, M. A., and Borden, R. H. (1988). "Analysis of load deflection response of laterally loaded piers using DMT." *International Symposium on Penetration Testing, ISOPT-1*Orlando, Florida, 245-253.

Gabr, M. A., Lunne, T., and Powell, J. J. (1994). "P-y Analysis of Laterally Loaded Piles in Clay Using DMT." *Journal of Geotechnical Engineering*, 120(5), 816-837.

Garga, V. K., and Zhang, H. (1997). "Volume changes in undrained triaxial tests on sands." *Canadian Geotechnical Journal*, 34(5), 762-772.

Georgiadis, M. "Development ofp- y curves for layered soils." *Proc., Geotechnical Practice in Offshore Engineering*, ASCE, 536–545.

Germaine, J., and Ladd, C. (1988). "State-of-the-Art Paper: Triaxial Testing of Saturated Cohesive Soils." *Advanced Triaxial Testing of Soil and Rock, STP29091S*, R. Donaghe, R. Chaney, and M. Silver, eds., ASTM International, West Conshohocken, PA.

Gerolymos, N., and Gazetas, G. (2005). "Phenomenological model applied to inelastic response of soil-pile interaction systems." *Journal of the Japanese Geotechnical Society : soils and foundation*, 45(4), 119-132.

Henkel, D. J., and Gilbert, G. D. (1952). "The Effect Measured of the Rubber Membrane on the Triaxial Compression Strength of Clay Samples." *Géotechnique*, 3(1), 20-29.

Hutchinson, T. C., Chai, Y. H., Boulanger, R. W., and Idriss, I. M. (2004). "Inelastic Seismic Response of Extended Pile-Shaft-Supported Bridge Structures." *Earthquake Spectra*, 20(4), 1057-1080.

Ibsen, L. B., and Praastrup, U. (2002). "The Danish rigid boundary true triaxial apparatus for soil testing." *Geotechnical Testing Journal*, 25(3).

Ismail, M. A., Sharma, S. S., and Fahey, a. M. (2005). "A small true triaxial apparatus with wave velocity measurement." *Geotechnical Testing Journal*, 28(2).

Jang, D.-J., and Frost, J. D. "Sand structure differences resulting from specimen preparation procedures " *Proc., Geotechnical Earthquake Engineering and Soil Dynamics III*, American Society of Civil Engineers.

Karthigeyan, S., Ramakrishna, V. V. G. S. T., and Rajagopal, K. (2007). "Numerical Investigation of the Effect of Vertical Load on the Lateral Response of Piles." *Journal of Geotechnical and Geoenvironmental Engineering*, 133(5), 512-521.

Kerop D. Janoyan, Wallace, J. W., and Jonathan, P. S. (2006). "Full-Scale Cyclic Lateral Load Test of Reinforced Concrete Pier-Column." *Structural Journal*, 103(2).

Kiekbusch, M., and Schuppener, B. (1977). "Membrane Penetration and Its Effect on Pore Pressures." *Journal of the Geotechnical Engineering Division*, 103(GT11), 1267-1279.

Kim, J., Jeong, S., and Kim, Y. (2014). "Improved design method for bent pile structures (cast-in-drilled-hole shafts) based on nonlinear characteristics." *Materials and Structures*, 47(7), 1239-1258.

Kim, Y., and Jeong, S. (2011). "Analysis of soil resistance on laterally loaded piles based on 3D soil–pile interaction." *Computers and Geotechnics*, 38(2), 248-257.

King, D. J., Priestle, M., and Park, R. (1986). "Computer Programs for Concrete Column Design." Research Report 86/12. Department of Civil Engineering, University of Canterbury, New Zealand.

Ko, H.-Y., and Scott, R. F. (1967). "A New Soil Testing Apparatus." *Géotechnique*, 17(1), 40-57.

Kramer, S. L., Sivaneswaran, N., and Davis, R. O. (1990). "Analysis of Membrane Penetration in Triaxial Test." *Journal of Engineering Mechanics*, 116(4), 773-789.

Kulhawy, F. H., and Mayne, P. W. (1990). "Manual on Estimating Soil Properties for Foundation Design." Electric Power Research Institute. EL-6800. Research Project 1493-06.

La Rochelle, P., Leroueil, S., Trak, B., Blais-Leroux, L., and Tavenas, F. (1988). "Observational Approach to Membrane and Area Corrections in Triaxial Tests." *Advanced Triaxial Testing of Soil and Rock, STP29110S*, R. Donaghe, R. Chaney, and M. Silver, eds., ASTM International, West Conshohocken, PA, 715-731.

Ladd, C. C., and Foott, R. (1974). "New design procedure for stability of soft clays." *Journal of the Geotechnical Engineering Division*, 100(7), 763-786.

Ladd, R. S. (1978). "Preparing Test Specimens Using Undercompaction." *Geotechnical Testing Journal*, 1(1), 16-23.

Lade, P. (2016). *Triaxial Testing of Soils*, Wiley-Blackwell, Hoboken.

Limkatanyu, S., Kuntiyawichai, K., and Spacone, E. (2009). "Response of reinforced concrete piles including soil–pile interaction effects." *Engineering Structures*, 31(9), 1976-1986.

Lowe, J., and Johnson, T. C. "Use of Back Pressure to Increase Degree of Saturation of Triaxial Test Specimens " *Proc., Research Conference on Shear Strength of Cohesive Soils*, ASCE, 819-836.

Lu, J., Elgamal, A., Sikorsky, C., and Shantz, T. (2010). "Computational modeling of a large pile group under lateral load." *International Conferences on Recent Advances in Geotechnical Earthquake Engineering and Soil Dynamics*, Missouri University of Science and Technolog, Missouri University of Science and Technolog, Paper 9.

Lu, J., Elgamal, A., and Yang, Z. (2011). "OpenSeesPL: 3D Lateral Pile-Ground Interaction . User Manual (Beta 1.0) ", University of California, San Diego

Department of Structural Engineering

Lu, Y. Q., and Kennedy, D. J. L. (1994). "The flexural behaviour of concrete-filled hollow structural sections." *Canadian Journal of Civil Engineering*, 21(1), 111-130.

Mander, J. B., Priestley, M. J. N., and Park, R. (1988). "Theretical stress-strain model for confined concrete." *Journal of Structural Engineering*, 114(8), 1804-1825.

Marchetti, S., Totani, G., Calabrese, M., and Monaco, P. "P-y curves from DMT data for piles driven in clay." *Proc., 4th International Conference Deep Foundation Institute on Piling and Deep Foundations*, 263-272.

Martin, G. R., Seed, H. B., and Finn, W. D. L. (1978). "Effects of System Compliance on Liquefaction Tests." *Journal of the Geotechnical Engineering Division*, 104(4), 463-479.

Matlock, H. (1970). "Correlation for design of laterally loaded piles in soft clay." *Offshore Technology Conference*Houston, Texas, 577-595.

Mayne, P. W., Christopher, B. R., and DeJong, J. (2001). "Manual on Subsurface Investigations." National Highway Institute, National Highway Institute.

Molenkamp, F., and Luger, H. J. (1981). "Modelling and minimization of membrane penetration effects in tests on granular soils." *Géotechnique*, 31(4), 471-486.

Montejo, L. A., González-Román, L. A., and Kowalsky, M. J. (2012). "Seismic Performance Evaluation of Reinforced Concrete-Filled Steel Tube Pile/Column Bridge Bents." *Journal of Earthquake Engineering*, 16(3), 401–424.

Mulilis, J., Townsend, F., and Horz, R. (1978). "Triaxial Testing Techniques and Sand Liquefaction " *Dynamic Geotechnical Testing* M. Silver, and D. Tiedemann, eds., ASTM International, Denver, Colorado, 265-279.

Naggar, M. H. E., and Bentley, K. J. (2000). "Dynamic analysis for laterally loaded piles and dynamic p-y curves." *Canadian Geotechnical Journal*, 37(6), 1166-1183.

Newland, P. L., and Allely, B. H. (1959). "Volume Changes During Undrained Triaxial Tests on Saturated Dilatant Granular Materials." *Géotechnique*, 9(4), 174-182.

Newland, P. L., and Allely, B. H. (1957). "Volume Changes in Drained Taixial Tests on Granular Materials." *Géotechnique*, 7(1), 17-34.

Nicholson, P. G., Seed, R. B., and Anwar, H. A. (1993). "Elimination of membrane compliance in undrained triaxial testing. I. Measurement and evaluation." *Canadian Geotechnical Journal*, 30(5), 727-738.

O'Neill, M. W., and Murchison, J. M. (1983). "An evaluation of p-y relationships in sands." *Report (American Petroleum Institute), PRAC 82-41-1*, University of Houston. Department of Civil Engineering, Research report No. GT-DF02-83.

Osman, A. S., and Bolton, M. D. (2005). "Simple plasticity-based prediction of the undrained settlement of shallow circular foundations on clay." *Géotechnique*, 55(6), 435-447.

Pranjoto, S., and Pender, M. J. "Gapping effects on the lateral stiffness of piles in cohesive soil." *Proc., Pacific Conference on Earthquake Engineering*, Paper No. 096.

Priestley, M. J. N., Calvi, G. M., and Kowalsky, M. J. (2007). *Displacment-Based Seimic Design Of Structures*, IUSS Press, Pavia, Italy.

Priestley, M. J. N., and Park, R. (1969). "Strength and Ductility of Concrete Bridge Columns Under Seismic Loading." *Structural Journal*, 84(1).

Priestley, M. J. N., Seible, F., Xiao, Y., and Verma, R. (1994). "Steel Jacket Retrofitting of Reinforced Concrete Bridge Columns for Enhanced Shear Strength--Part 2: Test Results and Comparison With Theory." *Structural Journal*, 91(5).

Rad, N. S., and Clough, G. W. (1984). "New Procedure for Saturating Sand Specimens." *Journal of Geotechnical Engineering*, 110(9), 1205-1218.

Rajaparthy, S. R., Zhang, Z., Hutchinson, T. C., and Lang, F. (2008). "Plastic Hinge Formation in Pile Foundations Due to Liquefaction-Induced Loads." *Geotechnical Earthquake Engineering and Soil Dynamics IV*, 1-10.

Ramana, K. V., and Raju, V. S. (1982). "Membrane Penetration in Triaxial Tests." *Journal of Geotechnical Engineering*, 108(GT2), 305-310.

Reese, L. C., Cox, W. R., and Koop, F. D. "Analysis of laterally loaded piles in sand." *Proc., 6th Offshore Technology Conference*, 473-483.

Reese, L. C., Cox, W. R., and Koop, F. D. "Field testing and analysis of laterally loaded piles in stiff clay." *Proc., The VII Annual Offshore Technology Conference*, 672-690.

Robertson, P., Davies, M., and Campanella, R. (1989). "Design of Laterally Loaded Driven Piles Using the Flat Dilatometer." *Geotechnical Testing Journal*, 12(1), 30-38.

Robertson, P. K., Campanella, R. G., Brown, P. T., Grof, I., and Hughes, J. M. O. (1985). "Design of axially and laterally loaded piles using in situ tests: A case history." *Canadian Geotechnical Journal*, 22(4), 518-527.

Roscoe, K., Schofield, A., and Thurairajah, A. (1964). "An Evaluation of Test Data for Selecting a Yield Criterion for Soils." *Laboratory Shear Testing of Soils, ASTM Special Technical Publication 361*, ASTM International, West Conshohocken, PA.

Seed, H. B., and Idriss, I. M. (1970). "Soil moduli and damping factors for dynamic response analysis." University of California, Berkeley. Report no. EERC 70-10, Earthquake Engineering Research Centre.

Seed, H. B., Wong, R. T., Idriss, I. M., and Tokimatsu, K. (1986). "Moduli and Damping Factors for Dynamic Analyses of Cohesionless Soils." *Journal of Geotechnical Engineering*, 112(11), 1016-1032.

Song, S. T., and Chai, Y. H. (2008). "Performance assessment of multi-column bents with extended pile-shafts under lateral earthquake loads." *The IES Journal Part A: Civil & Structural Engineering*, 1(1), 39-54.

Song, S. T., Chai, Y. H., and Hale, T. H. (2005). "Analytical Model for Ductility Assessment of Fixed-Head Concrete Piles." *Journal of Structural Engineering*, 131(7), 1051-1059.

Stewart, J. P., Taciroglu, E., Wallace, J. W., Ahlberg, E. R., Lemnitzer, A., Rha, C., and Khalili-Tehrani, P. (2007). "Full Scale Cyclic Large Deflection Testing of Foundation Support Systems for Highway Bridges. Part I: Drilled Shaft Foundations." University of California, Los Angeles. Report 2007/01.

Taciroglu, E., Rha, C., and Wallace, J. W. (2006). "A Robust Macroelement Model for Soil–Pile Interaction under Cyclic Loads." *Journal of Geotechnical and Geoenvironmental Engineering*, 132(10), 1304-1314.

Thomson, P. R., and Wong, R. C. K. (2008). "Specimen nonuniformities in water-pluviated and moist-tamped sands under undrained triaxial compression and extension." *Canadian Geotechnical Journal*, 45(7), 939-956.

Vaid, Y., and Negussey, D. (1984). "A Critical Assessment of Membrane Penetration in the Triaxial Test." *Geotechnical Testing Journal*, 7(2), 70-76.

Wood, F. M., Yamamuro, J. A., and Lade, P. V. (2008). "Effect of depositional method on the undrained response of silty sand." *Canadian Geotechnical Journal*, 45(11), 1525-1537.

Yamamuro, J., and Lade, P. (1993). "Effects of Strain Rate on Instability of Granular Soils." *Geotechnical Testing Journal*, 16(3), 304-313.

Yamamuro, J. A., Abrantes, A. E., and Lade, P. V. (2011). "Effect of Strain Rate on the Stress-Strain Behavior of Sand." *Journal of Geotechnical and Geoenvironmental Engineering*, 137(12), 1169-1178.

Yan, L., and Byrne, P. M. (1992). "Lateral pile response to monotonic pile head loading." *Canadian Geotechnical Journal*, 29(6), 955-970.

Yang, Z., and Jeremić, B. (2002). "Numerical analysis of pile behaviour under lateral loads in layered elastic–plastic soils." *International Journal for Numerical and Analytical Methods in Geomechanics*, 26(14), 1385-1406.

Yang, Z., and Jeremić, B. (2005). "Study of Soil Layering Effects on Lateral Loading Behavior of Piles." *Journal of Geotechnical and Geoenvironmental Engineering*, 131(6), 762-770.

Zhang, L., and Ahmari, S. (2013). "Nonlinear analysis of laterally loaded rigid piles in cohesive soil." *International Journal for Numerical and Analytical Methods in Geomechanics*, 37(2), 201-220.

Zhu, J., and Anderson, S. (1998). "Corrections for Triaxial Tests on Undisturbed Soils." *Geotechnical Testing Journal*, 26(3), 277-284.

6. APPENDICES

6.1 Appendix A. P-y curves generated from soil testing results

Table 6.1. Data for API p-y curves at D_R=20% and 40%

y (m)	D_R=20%			D_R=40%		
	γz=25 kPa	γz=50 kPa	γz=75 kPa	γz=25 kPa	γz=50 kPa	γz=75 kPa
	p (kN/m)	p (kN/m)	p (kN/m)	p (kN/m)	p (kN/m)	p (kN/m)
0	0.0	0.0	0.0	0.0	0.0	0.0
0.0006	32.5	66.0	99.3	39.4	80.2	120.9
0.0012	61.5	129.7	196.9	73.3	156.8	239.0
0.0018	84.6	188.9	291.0	98.9	226.7	352.1
0.0024	101.6	242.3	380.4	116.3	287.9	458.0
0.003	113.3	289.0	463.8	127.4	339.6	555.3
0.0036	121.0	328.8	540.5	134.2	382.0	643.1
0.0042	126.0	362.0	610.1	138.2	415.9	721.0
0.0048	129.1	389.1	672.4	140.5	442.4	789.2
0.0054	131.0	411.0	727.5	141.9	462.9	848.0
0.006	132.2	428.4	775.9	142.6	478.5	898.3
0.0066	133.0	442.2	818.0	143.1	490.3	940.9
0.0072	133.4	452.9	854.2	143.3	499.1	976.6
0.0078	133.7	461.3	885.3	143.5	505.7	1006.4
0.0084	133.9	467.8	911.8	143.5	510.6	1031.1
0.009	134.0	472.8	934.2	143.6	514.2	1051.6
0.0096	134.0	476.6	953.2	143.6	516.9	1068.3
0.0102	134.1	479.6	969.1	143.6	518.9	1082.1
0.0108	134.1	481.8	982.5	143.6	520.3	1093.4
0.0114	134.1	483.5	993.7	143.6	521.4	1102.6
0.012	134.1	484.9	1003.1	143.6	522.2	1110.0
0.015	134.1	488.0	1031.0	143.7	523.9	1131.0
0.02	134.1	489.0	1045.3	143.7	524.4	1140.3

Table 6.2. Data for API p-y curves at D_R=53% and 70%

y (m)	D_R=53%			D_R=70%		
	γz=25 kPa	γz=50 kPa	γz=75 kPa	γz=25 kPa	γz=50 kPa	γz=75 kPa
	p (kN/m)	p (kN/m)	p (kN/m)	p (kN/m)	p (kN/m)	p (kN/m)
0	0.00	0.0	0.0	0	0.0	0
0.0006	47.69	97.5	146.9	67.6	139.3	210.3
0.0012	87.56	189.6	290.0	120.7	268.4	413.2
0.0018	116.20	272.4	425.7	155.0	380.1	602.2
0.0024	134.61	343.1	551.4	174.5	471.0	772.8
0.003	145.61	401.3	665.1	184.8	541.4	922.2
0.0036	151.90	447.5	765.9	189.9	593.8	1049.8
0.0042	155.40	483.2	853.7	192.5	631.7	1156.4
0.0048	157.32	510.3	928.8	193.8	658.6	1243.8
0.0054	158.37	530.5	992.4	194.4	677.3	1314.5
0.006	158.94	545.4	1045.4	194.7	690.3	1370.8
0.0066	159.25	556.3	1089.3	194.8	699.2	1415.4
0.0072	159.42	564.2	1125.3	194.9	705.2	1450.4
0.0078	159.51	569.9	1154.6	194.9	709.3	1477.6
0.0084	159.55	574.0	1178.4	194.9	712.1	1498.7
0.009	159.58	576.9	1197.7	194.9	714.0	1515.1
0.0096	159.59	579.0	1213.1	195.0	715.3	1527.7
0.0102	159.60	580.6	1225.5	195.0	716.2	1537.4
0.0108	159.61	581.6	1235.4	195.0	716.8	1544.8
0.0114	159.61	582.4	1243.4	195.0	717.2	1550.5
0.012	159.61	583.0	1249.7	195.0	717.4	1554.9
0.015	159.61	584.1	1266.5	195.0	717.9	1565.4
0.02	159.61	584.3	1273.1	195.0	718.0	1568.7

Table 6.3. Proposed API-like p-y curves at D_R=20%

γz=25 kPa		γz=50 kPa		γz=75 kPa	
y (m)	p (kN/m)	y (m)	p (kN/m)	y (m)	p (kN/m)
0.0000	0.0	0.0000	0.0	0.0000	0.0
0.0008	53.8	0.0007	156.0	0.0005	281.0
0.0016	80.2	0.0013	243.9	0.0011	450.7
0.0024	95.9	0.0020	301.2	0.0016	566.8
0.0032	106.0	0.0027	341.1	0.0022	650.8
0.0040	113.1	0.0033	370.3	0.0027	714.1
0.0048	118.3	0.0040	392.4	0.0033	763.2
0.0056	122.3	0.0047	409.7	0.0038	802.3
0.0064	125.4	0.0053	423.6	0.0044	834.1
0.0072	127.9	0.0060	435.0	0.0049	860.3
0.0080	130.0	0.0067	444.4	0.0055	882.4
0.0088	131.7	0.0073	452.4	0.0060	901.2
0.0096	133.1	0.0080	459.2	0.0065	917.3
0.0104	134.1	0.0087	465.1	0.0071	931.3
0.0112	134.1	0.0093	470.2	0.0076	943.6
0.0120	134.1	0.0100	474.7	0.0082	954.5
		0.0107	478.8	0.0087	964.1
		0.0113	482.3	0.0093	972.8
		0.0120	484.9	0.0098	980.6
				0.0104	987.6
				0.0109	994.0
				0.0115	999.9
				0.0120	1003.1

Table 6.4. Proposed API-like p-y curves at D_R=40%

γz=25 kPa		γz=50 kPa		γz=75 kPa	
y (m)	**p (kN/m)**	**y (m)**	**p (kN/m)**	**y (m)**	**p (kN/m)**
0.0000	0.0	0.0000	0.0	0.0000	0.0
0.0008	64.2	0.0007	187.5	0.0006	347.1
0.0016	92.9	0.0014	287.2	0.0013	548.1
0.0024	109.2	0.0021	348.9	0.0019	679.1
0.0032	119.6	0.0028	390.8	0.0025	771.1
0.0040	126.9	0.0035	421.0	0.0032	839.2
0.0048	132.2	0.0042	443.9	0.0038	891.6
0.0056	136.3	0.0049	461.8	0.0044	933.2
0.0064	139.5	0.0056	476.1	0.0051	966.9
0.0072	142.2	0.0064	487.9	0.0057	994.8
0.0080	143.6	0.0071	497.7	0.0063	1018.3
0.0088	143.6	0.0078	506.1	0.0069	1038.4
0.0096	143.6	0.0085	513.3	0.0076	1055.7
0.0104	143.6	0.0092	519.5	0.0082	1070.8
0.0112	143.6	0.0099	522.2	0.0088	1084.1
0.0120	143.6	0.0106	522.2	0.0095	1095.9
		0.0113	522.2	0.0101	1106.4
		0.0120	522.2	0.0107	1110.0
				0.0114	1110.0
				0.0120	1110.0

Table 6.5. Proposed API-like p-y curves at D_R=53%

γz=25 kPa		γz=50 kPa		γz=75 kPa	
y (m)	**p (kN/m)**	**y (m)**	**p (kN/m)**	**y (m)**	**p (kN/m)**
0.0000	0.0	0.0000	0.0	0.0000	0.0
0.0009	77.4	0.0008	228.2	0.0007	427.3
0.0017	112.0	0.0016	348.5	0.0014	672.0
0.0026	131.3	0.0024	422.8	0.0021	831.2
0.0034	143.5	0.0032	472.6	0.0028	942.2
0.0043	151.8	0.0040	508.1	0.0035	1023.5
0.0051	157.8	0.0048	534.6	0.0042	1085.5
0.0060	159.6	0.0056	555.0	0.0049	1134.0
0.0069	159.6	0.0064	571.3	0.0056	1173.1
0.0077	159.6	0.0072	583.0	0.0064	1205.2
0.0086	159.6	0.0080	583.0	0.0071	1231.9
0.0094	159.6	0.0088	583.0	0.0078	1249.7
0.0103	159.6	0.0096	582.9	0.0085	1249.7
0.0111	159.6	0.0104	582.9	0.0092	1249.6
0.0120	159.6	0.0112	582.9	0.0099	1249.6
		0.0120	582.9	0.0106	1249.6
				0.0113	1249.6
				0.0120	1249.6

Table 6.6. Proposed API-like p-y curves at D_R=70%

γz=25 kPa		γz=50 kPa		γz=75 kPa	
y (m)	p (kN/m)	y (m)	p (kN/m)	y (m)	p (kN/m)
0.0000	0.0	0.0000	0.0	0.0000	0.0
0.0006	74.7	0.0005	215.0	0.0004	344.9
0.0011	116.3	0.0011	351.4	0.0009	591.0
0.0017	142.5	0.0016	445.6	0.0013	776.3
0.0023	160.5	0.0022	514.2	0.0018	920.4
0.0029	173.6	0.0027	566.3	0.0022	1035.6
0.0034	183.5	0.0033	607.0	0.0027	1129.6
0.0040	191.2	0.0038	639.7	0.0031	1207.6
0.0046	195.0	0.0044	666.5	0.0036	1273.3
0.0051	195.0	0.0049	688.9	0.0040	1329.3
0.0057	194.9	0.0055	707.8	0.0044	1377.7
0.0063	194.9	0.0060	717.4	0.0049	1419.8
0.0069	194.9	0.0065	717.4	0.0053	1456.8
0.0074	194.9	0.0071	717.4	0.0058	1489.6
0.0080	194.9	0.0076	717.4	0.0062	1518.8
		0.0082	717.4	0.0067	1544.9
		0.0087	717.3	0.0071	1554.9
		0.0093	717.3	0.0076	1554.9
		0.0098	717.4	0.0080	1554.8
		0.0104	717.4	0.0084	1554.8
		0.0109	717.4	0.0089	1554.7
		0.0115	717.4	0.0093	1554.7
		0.0120	717.4	0.0098	1554.7
				0.0102	1554.7
				0.0107	1554.7
				0.0111	1554.8
				0.0116	1554.8
				0.0120	1554.8

6.2 Appendix B. Displacement and loading histories on S5 and S6, and their displacement profiles

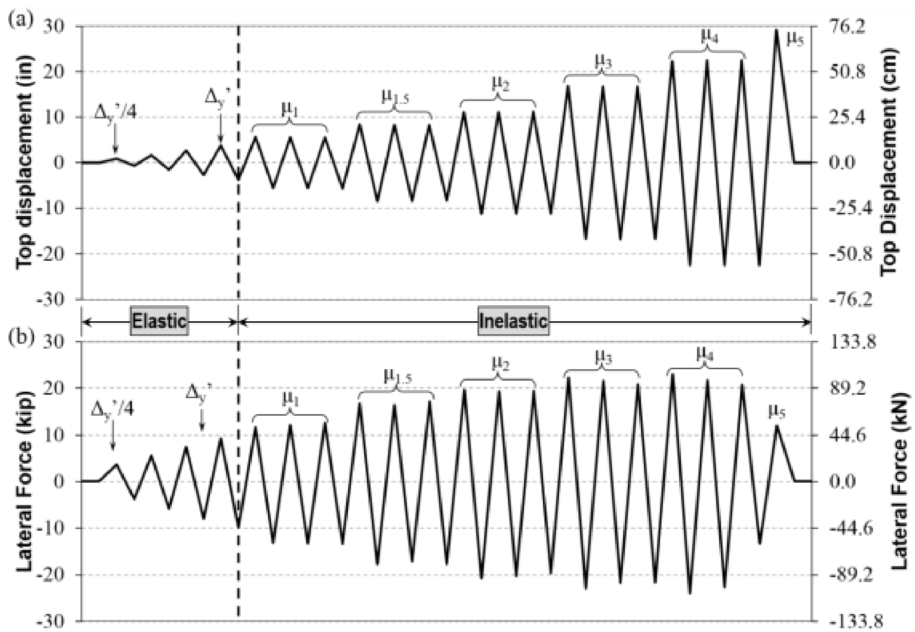

Figure 6.1. Experimental displacement and load histories on S5 (courtesy of Diego Aguirre)

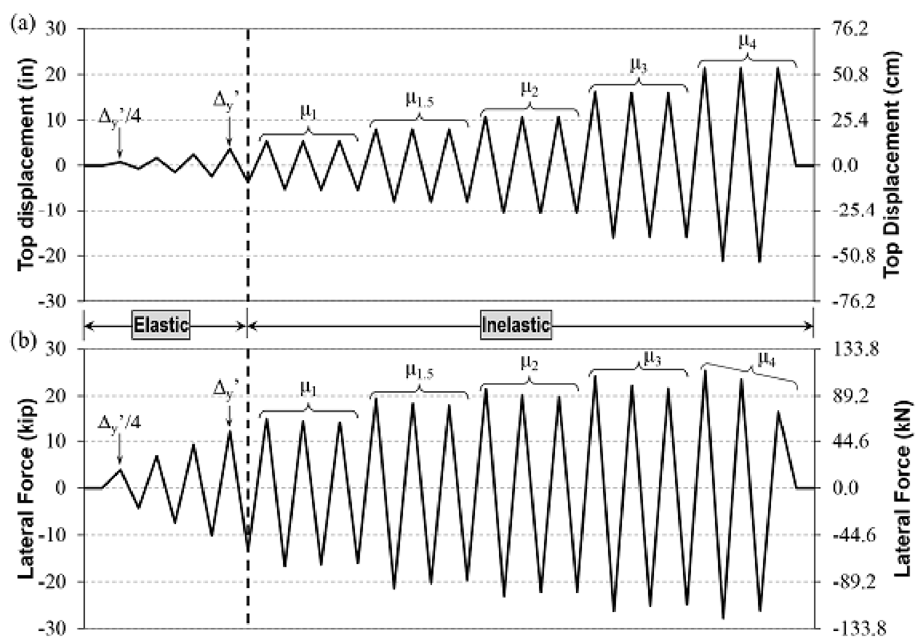

Figure 6.2. Experimental displacement and load histories on S6 (courtesy of Diego Aguirre)

Table 6.7. S5 experimental displacement profile (courtesy of Diego Aguirre)

z (m)	+1/4Δy'	−1/4Δy'	+1/2Δy'	−1/2Δy'	+3/4Δy'	-3/4Δy'	+Δy'	− Δy'
	y (cm)	y (cm)	y (cm)	y (cm)	y (cm)	y (cm)	y (cm)	y (cm)
1.73	2.13	-1.80	4.29	-4.09	6.76	-6.73	9.55	-9.55
1.32	1.89	-1.55	3.78	-3.54	5.92	-5.86	8.39	-8.33
0.71	1.54	-1.18	3.05	-2.74	4.73	-4.61	6.73	-6.58
0.10	1.21	-0.84	2.34	-2.00	3.58	-3.42	5.12	-4.92
-0.51	0.91	-0.55	1.70	-1.33	2.54	-2.35	3.65	-3.40
-1.12	0.66	-0.32	1.18	-0.81	1.67	-1.48	2.41	-2.14
-1.73	0.48	-0.18	0.77	-0.42	0.98	-0.80	1.39	-1.14
-2.34	0.37	-0.10	0.49	-0.18	0.48	-0.34	0.62	-0.42
-2.95	0.32	-0.07	0.31	-0.05	0.12	-0.02	0.02	0.12
-3.56	0.28	-0.07	0.17	0.04	-0.18	0.23	-0.50	0.57
-4.19	0.26	-0.08	-0.05	0.09	-0.48	0.43	-1.03	0.96

Table 6.8. S6 experimental displacement profile (courtesy of Diego Aguirre)

z (m)	+1/4Δy'	−1/4Δy'	+1/2Δy'	−1/2Δy'	+3/4Δy'	-3/4Δy'	+Δy'	− Δy'
	y (cm)	y (cm)	y (cm)	y (cm)	y (cm)	y (cm)	y (cm)	y (cm)
1.79	1.80	-1.82	4.04	-3.83	6.20	-6.05	9.28	-9.25
1.38	1.54	-1.60	3.50	-3.28	5.37	-5.19	8.06	-7.93
0.77	1.17	-1.30	2.73	-2.48	4.19	-3.93	6.32	-6.01
0.16	0.81	-1.05	1.99	-1.75	3.05	-2.79	4.65	-4.26
-0.45	0.50	-0.83	1.33	-1.12	2.03	-1.78	3.13	-2.71
-1.06	0.31	-0.67	0.88	-0.65	1.30	-1.02	2.00	-1.53
-1.67	0.17	-0.57	0.53	-0.35	0.74	-0.50	1.12	-0.70
-2.28	0.10	-0.52	0.34	-0.20	0.39	-0.20	0.53	-0.18
-2.89	0.08	-0.51	0.25	-0.16	0.20	-0.06	0.13	0.14
-3.50	0.08	-0.51	0.20	-0.17	0.06	0.00	-0.19	0.35
-4.13	0.08	-0.52	0.17	-0.19	-0.05	0.06	-0.43	0.59

6.3 Appendix C. Displacement profiles for pile stiffness calibration

Table 6.9. Displacement profiles of cantilever beam and pile at various lateral loads

Level (m)	P = 16.4 kN		P=32.8 kN		P=65.6 kN	
	Beam (m)	Pile (m)	Beam (cm)	Pile (cm)	Beam (cm)	Pile (cm)
2	0.0032	0.0031	0.0064	0.0063	0.0128	0.0130
1.8	0.0027	0.0027	0.0055	0.0053	0.0109	0.0110
1.6	0.0023	0.0022	0.0045	0.0044	0.0090	0.0089
1.4	0.0018	0.0018	0.0036	0.0036	0.0072	0.0072
1.2	0.0014	0.0014	0.0028	0.0028	0.0055	0.0057
1	0.0010	0.0011	0.0020	0.0021	0.0040	0.0042
0.8	0.0007	0.0007	0.0013	0.0015	0.0027	0.0030
0.6	0.0004	0.0005	0.0008	0.0009	0.0016	0.0019
0.4	0.0002	0.0003	0.0004	0.0005	0.0007	0.0010
0.2	0.00005	0.0001	0.0001	0.0002	0.0002	0.0004
0	0.0032	0.0031	0.0064	0.0063	0.0000	0.0000

6.4 Appendix D. Displacement profiles for S5 and S6 resulted from model calibration

Table 6.10. Lateral displacement profiles for S5 from model calibration

z (m)	P_1 =15.93 (kN)	P_2 =25.01 (kN)	P_3 =33.02 (kN)
	y (cm)	y (cm)	y (cm)
1.73	2.33	4.52	6.92
1.40	2.12	4.08	6.21
1.00	1.87	3.62	5.37
0.50	1.56	2.94	4.35
0.00	1.23	2.29	3.40
-0.30	1.02	1.92	2.87
-0.60	0.82	1.58	2.38
-0.90	0.65	1.27	1.93
-1.20	0.50	0.99	1.53
-1.50	0.37	0.75	1.17
-1.80	0.26	0.54	0.86
-2.4	0.10	0.23	0.36
-3.30	-0.06	-0.10	-0.15
-4.20	-0.14	-0.30	-0.53

Table 6.11. Lateral displacement profiles for S6 from model calibration

z (m)	P_1 =17.5 (kN)	P_2 =27.1 (kN)	P_3 =41 (kN)
	y (cm)	y (cm)	y (cm)
1.73	2.17	4.01	6.44
1.40	1.84	3.50	5.58
1.00	1.52	2.92	4.73
0.50	1.18	2.27	3.70
0.00	0.89	1.68	2.81
-0.30	0.71	1.35	2.29
-0.60	0.56	1.06	1.82
-0.90	0.42	0.81	1.41
-1.20	0.29	0.59	1.04
-1.50	0.19	0.41	0.74
-1.80	0.11	0.26	0.48
-2.4	0.01	0.05	0.16
-3.30	-0.07	-0.12	-0.20
-4.10	-0.10	-0.21	-0.39

6.5 Appendix E. Displacement profiles for free-field condition

Table 6.12. Displacement profile for 8x8m and 13x13m domains

z (m)	8x8m	13x13m
	y (cm)	y (cm)
1.73	9.21	9.72
1.40	8.35	8.83
1.00	7.33	7.76
0.50	6.08	6.46
0.00	4.90	5.23
-0.30	4.24	4.53
-0.60	3.61	3.87
-0.90	3.02	3.26
-1.20	2.48	2.69
-1.50	1.99	2.16
-1.80	1.55	1.69
-2.4	0.79	0.87
-3.30	-0.135	-0.13
-4.10	-0.861	-0.94

Table 6.13. Displacement profiles for free-field condition, D_R=10%

z m	5 kN	10 kN	15.9 kN	20 kN	25 kN	28 kN	33 kN	41 kN	45 kN
	y (cm)	y (cm)	y (cm)	y (cm)	y (cm)	y (cm)	y (cm)	y (cm)	y (cm)
1.73	0.82	1.85	3.38	4.60	6.33	7.50	9.72	13.94	16.61
1.40	0.73	1.66	3.04	4.15	5.72	6.79	8.83	12.71	14.98
1.00	0.62	1.42	2.63	3.61	5.00	5.95	7.76	11.23	13.27
0.50	0.49	1.14	2.14	2.95	4.12	4.93	6.46	9.42	11.18
0.00	0.37	0.88	1.68	2.34	3.30	3.96	5.23	7.70	9.17
-0.30	0.31	0.74	1.42	1.99	2.83	3.41	4.53	6.72	8.03
-0.60	0.25	0.61	1.19	1.67	2.39	2.90	3.87	5.79	6.93
-0.90	0.20	0.49	0.97	1.38	1.99	2.42	3.26	4.91	5.90
-1.20	0.15	0.38	0.77	1.11	1.62	1.98	2.69	4.08	4.93
-1.50	0.11	0.29	0.60	0.87	1.29	1.58	2.16	3.32	4.02
-1.80	0.08	0.21	0.45	0.66	0.99	1.22	1.69	2.62	3.18
-2.4	0.03	0.09	0.21	0.32	0.50	0.62	0.87	1.38	1.69
-3.30	-0.01	-0.02	-0.03	-0.04	-0.06	-0.08	-0.13	-0.23	-0.29
-4.10	-0.04	-0.09	-0.20	-0.31	-0.50	-0.64	-0.94	-1.57	-1.96

Table 6.14. Displacement profiles for free-field condition, D_R=20%

z m	5 kN	10 kN	15.9 kN	20 kN	25 kN	28 kN	33 kN	41 kN	45 kN
	y (cm)	y (cm)	y (cm)	y (cm)	y (cm)	y (cm)	y (cm)	y (cm)	y (cm)
1.73	0.69	1.56	2.81	3.78	5.11	6.00	7.65	10.74	12.52
1.40	0.61	1.39	2.51	3.38	4.59	5.39	6.90	9.73	11.35
1.00	0.52	1.18	2.15	2.91	3.97	4.67	6.00	8.51	9.95
0.50	0.40	0.93	1.72	2.34	3.21	3.80	4.91	7.03	8.26
0.00	0.30	0.70	1.31	1.81	2.51	2.98	3.89	5.63	6.64
-0.30	0.24	0.57	1.09	1.51	2.12	2.53	3.32	4.84	5.73
-0.60	0.19	0.46	0.89	1.24	1.76	2.11	2.78	4.10	4.88
-0.90	0.15	0.36	0.71	1.00	1.43	1.72	2.29	3.41	4.08
-1.20	0.11	0.27	0.55	0.78	1.13	1.37	1.85	2.79	3.34
-1.50	0.08	0.20	0.41	0.60	0.87	1.07	1.45	2.22	2.67
-1.80	0.05	0.14	0.29	0.43	0.65	0.80	1.10	1.71	2.07
-2.4	0.02	0.05	0.12	0.19	0.30	0.37	0.53	0.85	1.04
-3.30	-0.01	-0.02	-0.03	-0.04	-0.05	-0.06	-0.09	-0.16	-0.20
-4.10	-0.02	-0.05	-0.11	-0.18	-0.29	-0.37	-0.56	-0.95	-1.20

Table 6.15. Displacement profiles for free-field condition, D_R=40%

z m	5 kN	10 kN	15.9 kN	20 kN	25 kN	28 kN	33 kN	41 kN	45 kN
	y (cm)	y (cm)	y (cm)	y (cm)	y (cm)	y (cm)	y (cm)	y (cm)	y (cm)
1.73	0.548	1.235	2.178	2.878	3.810	4.408	5.489	7.421	8.497
1.40	0.478	1.083	1.920	2.543	3.376	3.913	4.885	6.630	7.604
1.00	0.396	0.904	1.615	2.147	2.862	3.324	4.166	5.685	6.536
0.50	0.298	0.692	1.251	1.674	2.246	2.619	3.303	4.548	5.250
0.00	0.210	0.499	0.918	1.240	1.680	1.969	2.504	3.491	4.053
-0.30	0.163	0.395	0.739	1.004	1.371	1.615	2.067	2.908	3.391
-0.60	0.123	0.304	0.578	0.792	1.092	1.293	1.668	2.374	2.782
-0.90	0.088	0.225	0.437	0.606	0.845	1.007	1.312	1.892	2.231
-1.20	0.060	0.158	0.317	0.446	0.632	0.759	1.001	1.468	1.743
-1.50	0.038	0.105	0.219	0.314	0.453	0.550	0.736	1.102	1.319
-1.80	0.021	0.064	0.141	0.207	0.307	0.378	0.516	0.792	0.958
-2.4	0.002	0.012	0.039	0.064	0.105	0.136	0.198	0.327	0.407
-3.30	-0.008	-0.015	-0.024	-0.029	-0.038	0.044	-0.060	-0.095	-0.118
-4.10	-0.007	-0.018	-0.038	-0.057	-0.093	-0.123	-0.190	-0.346	-0.447

6.6 Appendix F. P - y curves for free-field condition

Table 6.16. p (kN/m) - y (m) curves for free-field condition, D_R=10%

z (m)		5 kN	10kN	15.9kN	20kN	25kN	28kN	33kN	41kN	45kN
-0.3	y	0.0031	0.0074	0.0142	0.0199	0.0283	0.0341	0.0453	0.0672	0.0803
	p	4.19	8.40	12.59	14.39	15.46	16.17	17.02	17.40	17.90
-0.6	y	0.0025	0.0061	0.0119	0.0167	0.0239	0.0290	0.0387	0.0579	0.0693
	p	5.35	9.71	15.69	19.90	24.73	27.40	30.96	34.07	34.39
-0.9	y	0.0020	0.0049	0.0097	0.0138	0.0199	0.0242	0.0326	0.0491	0.0590
	p	5.86	10.70	15.73	19.28	24.46	27.76	33.81	43.82	48.17
-1.2	y	0.0015	0.0038	0.0077	0.0111	0.0162	0.0198	0.0269	0.0408	0.0493
	p	5.65	11.10	16.48	19.77	23.53	26.16	30.97	40.81	46.45
-1.8	y	0.0008	0.0021	0.0045	0.0066	0.0099	0.0122	0.0169	0.0262	0.0318
	p	3.25	8.43	15.51	19.88	24.36	26.62	30.43	36.50	39.64
-2.4	y	0.0003	0.0009	0.0021	0.0032	0.0050	0.0062	0.0087	0.0138	0.0169
	p	0.61	3.88	9.22	14.25	19.12	22.27	27.38	33.81	36.69

Table 6.17. p (kN/m) - y (m) curves for free-field condition, D_R=20%

z (m)		5 kN	10kN	15.9kN	20kN	25kN	28kN	33kN	41kN	45kN
-0.3	y	0.0024	0.0057	0.0109	0.0151	0.0212	0.0253	0.0332	0.0484	0.0573
	p	5.15	9.70	13.99	15.68	16.64	17.11	18.13	18.75	19.10
-0.6	y	0.0019	0.0046	0.0089	0.0124	0.0176	0.0211	0.0278	0.0410	0.0488
	p	6.05	10.85	17.48	21.88	26.68	29.01	33.12	36.59	36.61
-0.9	y	0.0015	0.0036	0.0071	0.0100	0.0143	0.0172	0.0229	0.0341	0.0408
	p	6.59	11.45	16.91	20.75	26.53	29.55	35.54	46.15	50.58
-1.2	y	0.0011	0.0027	0.0055	0.0078	0.0113	0.0137	0.0185	0.0279	0.0334
	p	6.19	11.58	17.05	20.33	25.02	27.61	32.38	42.54	48.36
-1.8	y	0.0005	0.0014	0.0029	0.0043	0.0065	0.0080	0.0110	0.0171	0.0207
	p	2.86	8.93	14.91	19.31	24.21	26.47	29.72	35.31	38.75
-2.4	y	0.0002	0.0005	0.0012	0.0019	0.0030	0.0037	0.0053	0.0085	0.0104
	p	0.32	2.18	8.42	12.82	17.04	20.48	25.34	31.81	34.20

Table 6.18. p (kN/m) - y (m) curves for free-field condition, D_R=40%

z (m)		5 kN	10kN	15.9kN	20kN	25kN	28kN	33kN	41kN	45kN
-0.3	**y**	0.0016	0.0040	0.0074	0.0100	0.0137	0.0162	0.0207	0.0291	0.0339
	p	6.50	13.26	17.61	19.09	21.13	22.55	23.65	23.75	23.95
-0.6	**y**	0.0012	0.0030	0.0058	0.0079	0.0109	0.0129	0.0167	0.0237	0.0278
	p	7.0	13.1	22.2	27.3	32.2	35.8	40.2	43.9	43.7
-0.9	**y**	0.0009	0.0023	0.0044	0.0061	0.0085	0.0101	0.0131	0.0189	0.0223
	p	7.1	12.7	18.7	22.8	27.5	33.0	39.9	51.4	56.5
-1.2	**y**	0.0006	0.0016	0.0032	0.0045	0.0063	0.0076	0.0100	0.0147	0.0174
	p	6.2	12.1	17.9	21.1	24.8	28.1	32.7	42.2	48.3
-1.8	**y**	0.0002	0.0006	0.0014	0.0021	0.0031	0.0038	0.0052	0.0079	0.0096
	p	1.6	7.4	13.3	17.0	21.3	24.0	27.9	33.4	36.1
-2.4	**y**	0.0000	0.0001	0.0004	0.0006	0.0011	0.0014	0.0020	0.0033	0.0041
	p	0.9	1.9	3.8	7.2	10.3	14.1	18.5	26.2	29.6

Table 6.19. Normalized p-y curves for D_R=10%

z=0.3m		z-0.6m		z=0.9m	
y/D	$p/(\sigma_z D)$	y/D	$p/(\sigma_z D)$	y/D	$p/(\sigma_z D)$
0.010	0.98	0.008	0.63	0.006	0.46
0.023	1.97	0.019	1.14	0.015	0.84
0.044	2.96	0.037	1.84	0.030	1.23
0.062	3.38	0.052	2.34	0.043	1.51
0.088	3.63	0.075	2.90	0.062	1.91
0.107	3.80	0.091	3.22	0.076	2.17
0.142	3.99	0.121	3.63	0.102	2.65
0.210	4.08	0.181	4.00	0.153	3.43
0.251	4.20	0.217	4.04	0.184	3.77

Table 6.20. Normalized p-y curves for D_R=20%

z=0.3m		z-0.6m		z=0.9m	
y/D	$p / (\sigma_z D)$	y/D	$p / (\sigma_z D)$	y/D	$p / (\sigma_z D)$
0.008	1.18	0.006	0.69	0.005	0.50
0.018	2.23	0.014	1.25	0.011	0.88
0.034	3.21	0.028	2.01	0.022	1.29
0.047	3.60	0.039	2.51	0.031	1.59
0.066	3.82	0.055	3.06	0.045	2.03
0.079	3.93	0.066	3.33	0.054	2.26
0.104	4.16	0.087	3.80	0.072	2.72
0.151	4.30	0.128	4.20	0.107	3.53
0.179	4.38	0.152	4.20	0.127	3.87

Table 6.21. Normalized p-y curves for D_R=40%

z=0.3m		z-0.6m		z=0.9m	
y/D	$p / (\sigma_z D)$	y/D	$p / (\sigma_z D)$	y/D	$p / (\sigma_z D)$
0.005	1.44	0.004	0.78	0.003	0.52
0.012	2.94	0.010	1.45	0.007	0.94
0.023	3.91	0.018	2.46	0.014	1.38
0.031	4.23	0.025	3.03	0.019	1.68
0.043	4.69	0.034	3.57	0.026	2.03
0.050	5.00	0.040	3.96	0.031	2.44
0.065	5.25	0.052	4.46	0.041	2.95
0.091	5.27	0.074	4.87	0.059	3.80
0.106	5.31	0.087	4.85	0.070	4.18

Table 6.22. API p-y curves, D_R=10%, kh=31,200 kN/m^3

y (m)	z=0.3m	z-0.6m	z=0.9m	z=1.2m	z=1.8m	z=2.4m
	p (kN/m)	p (kN/m)	p (kN/m)	p (kN/m)	p (kN/m)	p (kN/m)
0	0.00	0.0	0.0	0.0	0.0	0.0
0.0006	5.44	10.8	15.9	21.6	33.0	44.4
0.0012	9.95	19.7	27.5	39.1	62.4	85.7
0.0018	13.15	25.8	34.2	50.9	86.0	121.5
0.0024	15.16	29.6	37.4	57.9	103.3	150.8
0.003	16.35	31.7	39.0	61.8	115.3	173.6
0.0036	17.02	32.9	39.6	63.8	123.2	190.8
0.0042	17.38	33.5	39.9	64.9	128.2	203.2
0.0048	17.58	33.8	40.0	65.5	131.4	212.1
0.0054	17.68	34.0	40.1	65.7	133.4	218.4
0.006	17.74	34.1	40.1	65.9	134.7	222.7
0.0066	17.77	34.1	40.1	66.0	135.4	225.7
0.0072	17.79	34.1	40.1	66.0	135.9	227.8
0.0078	17.79	34.2	40.1	66.0	136.2	229.2
0.0084	17.80	34.2	40.1	66.0	136.3	230.2
0.009	17.80	34.2	40.1	66.0	136.4	230.8
0.0096	17.80	34.2	40.1	66.0	136.5	231.3
0.0102	17.80	34.2	40.1	66.0	136.5	231.6
0.0108	17.80	34.2	40.1	66.0	136.6	231.8
0.0114	17.80	34.2	40.1	66.0	136.6	231.9
0.012	17.80	34.2	40.1	66.0	136.6	232.0
0.015	17.80	34.2	40.1	66.0	136.6	232.2
0.02	17.80	34.2	40.1	66.0	136.6	232.2
0.025	17.80	34.2	40.1	66.0	136.6	232.2
0.03	17.80	34.2	40.1	66.0	136.6	232.2
0.04	17.80	34.2	40.1	66.0	136.6	232.2
0.05	17.80	34.2	40.1	66.0	136.6	232.2

Table 6.23. API p-y curves, D_R=10%, kh=2,714 kN/m^3

y (m)	z=0.3m	z-0.6m	z=0.9m	z=1.2m	z=1.8m	z=2.4m
	p (kN/m)	p (kN/m)	p (kN/m)	p (kN/m)	p (kN/m)	p (kN/m)
0	0.00	0.0	0.0	0.0	0.0	0.0
0.0006	0.49	1.0	1.5	2.0	2.0	11.7
0.0012	0.98	2.0	2.9	3.9	3.9	23.4
0.0018	1.46	2.9	4.4	5.8	5.8	34.9
0.0024	1.95	3.9	5.8	7.8	7.8	46.3
0.003	2.43	4.9	7.2	9.7	9.7	57.4
0.0036	2.91	5.8	8.7	11.6	11.6	68.3
0.0042	3.38	6.8	10.0	13.5	13.5	78.8
0.0048	3.85	7.7	11.4	15.3	15.3	89.0
0.0054	4.31	8.6	12.7	17.2	17.2	98.8
0.006	4.77	9.5	14.0	19.0	19.0	108.2
0.0066	5.22	10.4	15.3	20.8	20.8	117.2
0.0072	5.66	11.3	16.5	22.5	22.5	125.7
0.0078	6.10	12.1	17.7	24.2	24.2	133.8
0.0084	6.52	13.0	18.9	25.9	25.9	141.4
0.009	6.94	13.8	20.0	27.5	27.5	148.5
0.0096	7.35	14.6	21.1	29.1	29.1	155.2
0.0102	7.75	15.4	22.1	30.7	30.7	161.5
0.0108	8.14	16.2	23.1	32.2	32.2	167.3
0.0114	8.52	16.9	24.1	33.7	33.7	172.8
0.012	8.90	17.7	25.0	35.1	35.1	177.8
0.015	10.60	21.0	29.0	41.5	41.5	197.8
0.02	12.88	25.3	33.7	49.9	49.9	216.7
0.025	14.52	28.4	36.5	55.7	55.7	225.4
0.03	15.65	30.5	38.1	59.5	59.5	229.2
0.04	16.91	32.7	39.5	63.5	63.5	231.6
0.05	17.44	33.6	40.0	65.1	65.1	232.1

Table 6.24. API p-y curves at z=0.6m and 0.9m for D_R=20% and 40%

D_R (%)	20		40	
z (m)	0.6	0.9	0.6	0.9
y (m)	p (kN/m)	p (kN/m)	p (kN/m)	p (kN/m)
0	0.0	0.0	0.0	0.0
0.0006	10.9	16.0	13.6	19.9
0.0012	19.9	27.9	24.4	33.9
0.0018	26.2	34.9	31.5	41.3
0.0024	30.2	38.5	35.6	44.8
0.003	32.6	40.2	37.8	46.3
0.0036	33.9	41.0	39.0	46.9
0.0042	34.6	41.3	39.5	47.2
0.0048	35.0	41.5	39.8	47.3
0.0054	35.2	41.6	40.0	47.3
0.006	35.3	41.6	40.0	47.3
0.0066	35.3	41.6	40.1	47.3
0.0072	35.4	41.6	40.1	47.3
0.0078	35.4	41.6	40.1	47.3
0.0084	35.4	41.6	40.1	47.3
0.009	35.4	41.6	40.1	47.3
0.0096	35.4	41.6	40.1	47.3
0.0102	35.4	41.6	40.1	47.3
0.0108	35.4	41.6	40.1	47.3
0.0114	35.4	41.6	40.1	47.3
0.012	35.4	41.6	40.1	47.3
0.015	35.4	41.6	40.1	47.3
0.02	35.4	41.6	40.1	47.3
0.025	35.4	41.6	40.1	47.3
0.03	35.4	41.6	40.1	47.3
0.04	35.4	41.6	40.1	47.3
0.05	35.4	41.6	40.1	47.3

6.7 Appendix G. Development of vertical and horizontal stresses extracted from numerical model

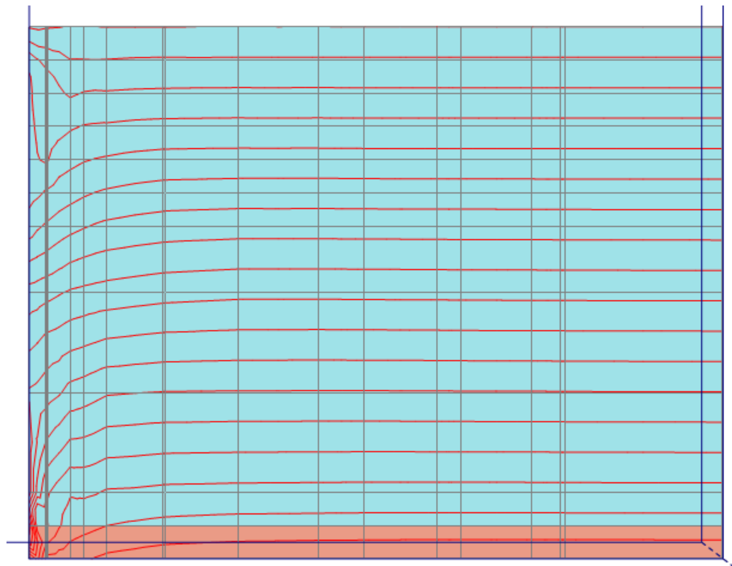

Figure 6.3. Distribution of vertical stress in front of pile at P=15.9 kN

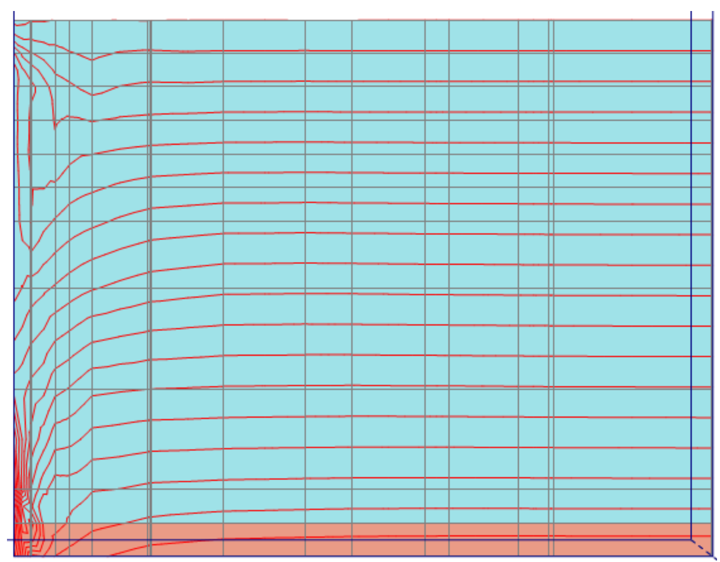

Figure 6.4. Distribution of vertical stress in front of pile at P=25 kN

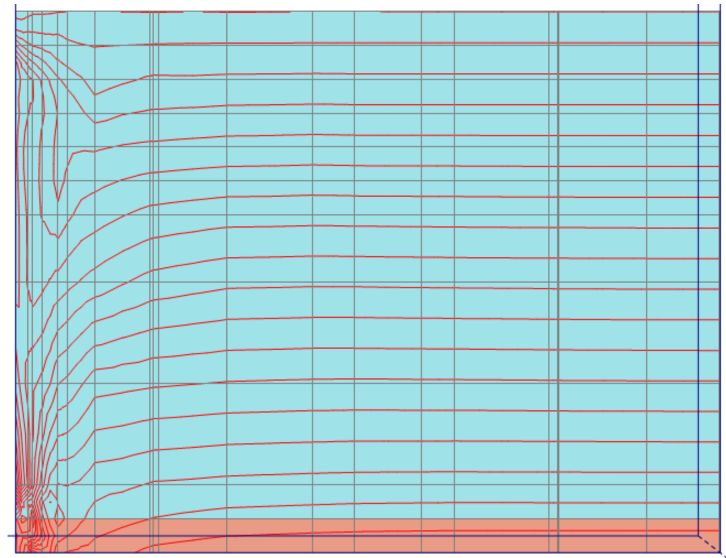

Figure 6.5. Distribution of vertical stress in front of pile at P=33 kN

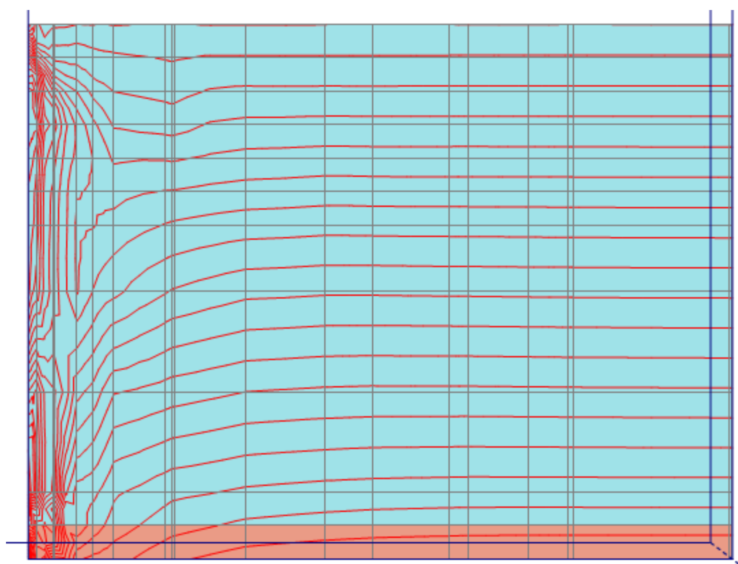

Figure 6.6. Distribution of vertical stress in front of pile at P=45 kN

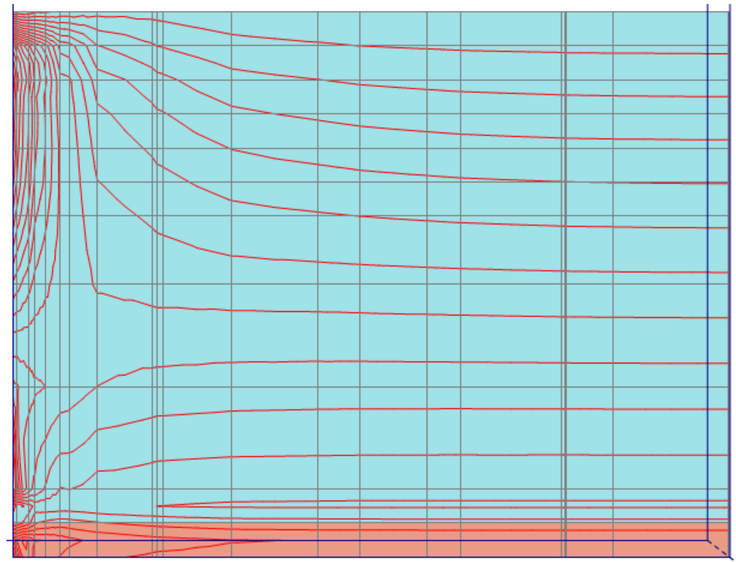

Figure 6.7 Distribution of horizontal stress in front of pile at P=15.9 kN

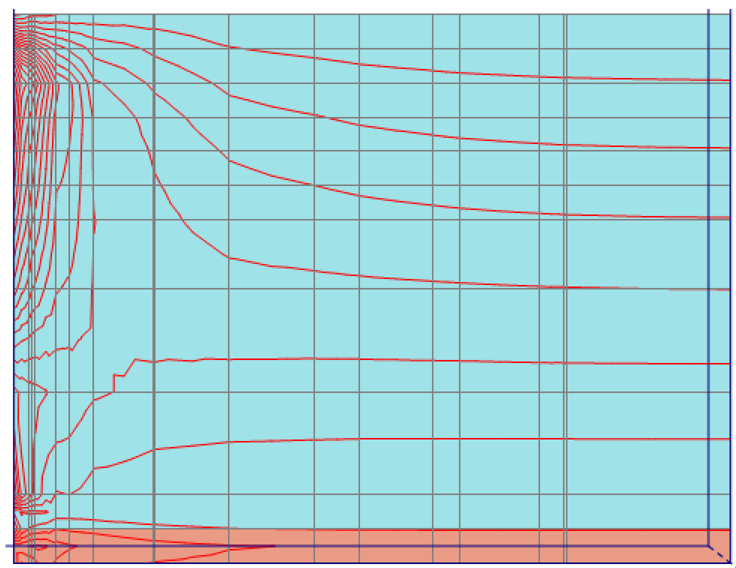

Figure 6.8. Distribution of horizontal stress in front of pile at P=25 kN

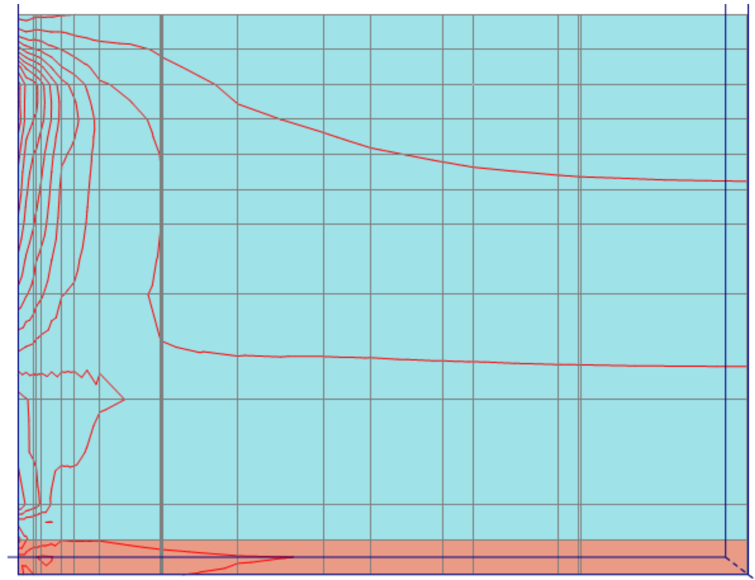

Figure 6.9. Distribution of horizontal stress in front of pile at P=33 kN

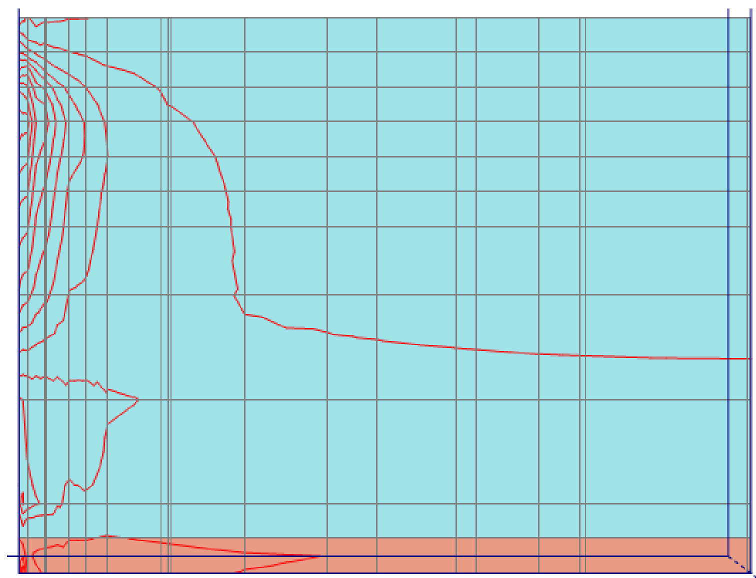

Figure 6.10. Distribution of horizontal stress in front of pile at P=45 kN